Superfluid Neutron Star Dynamics

Vadym Khomenko

Advisor: dr. hab. Brynmor Haskell

A thesis presented for the degree of
Doctor of Philosophy

Nicolaus Copernicus Astronomical Center
Polish Academy of Sciences
Bartycka 18, Warsaw
Poland

Abstract

Neutron stars are fantastic laboratories for fundamental physics. With densities in the interior exceeding nuclear saturation density, they allow to probe aspects of the strong interaction that cannot be studied in terrestrial laboratories. Furthermore at such high densities the Fermi energies of the constituents is much higher than the thermal energy, and this leads to neutrons being superfluid and protons superconducting.

It is well known from terrestrial studies that a superfluid rotates by forming an array of quantised vortices, and the movement of these vortices can create 'avalanches' in the interior of the neutron star, and lead to observable phenomena, such as pulsar glitches.

In this thesis the motion of vortices, and their avalanches will be considered in a hydrodynamical context. First a hydrodynamical model for vortex pileup and avalanche propagation will be presented, then it will be applied to large glitches in the Crab and Vela pulsars.

The hydrodynamical stability of the system will also be considered, by studying oscillations of the superfluid neutron star. It will be shown that there are modes that can grow unstable in the laminar regime, but are stabilised if turbulence develops.

After this, an analysis of non-linear mutual friction, also applicable to the turbulent case, will be presented, and the onset of turbulence in laboratory analogues of neutron stars will be discussed.

Streszczenie

Gwiazdy neutronowe są znakomitymi laboratoriami podstawowych problemów fizyki. Ponieważ gęstość we wnętrzu gwiazd neutronowych przekracza kilkukrotnie gęstość materii jądrowej, możemy dzięki obserwacjom takich gwiazd badać aspekty oddziaływania silnego nieosiągalne w laboratoriach naziemnych. Ponadto przy tak dużych gęstościach energie Fermiego składników są znacznie wyższe niż energia termiczna, w związku z tym neutrony są nadciekłe, a protony nadprzewodzące. Z badań naziemnych wiadomo, że nadciekły materiał rotuje tworząc układ skwantowanych wirów. Ruch takich wirów może powodować powstawanie „lawin" we wnętrzu gwiazdy neutronowej i prowadzić do obserwowalnych zjawisk, takich jak glicze pulsarów. W przedstawionej pracy ruch wirów i ich lawiny są rozpatrywane w kontekście hydrodynamicznym. Na wstępie przedstawiony jest model hydrodynamiczny opisujący spiętrzenia wirów i propagację lawin, a następnie jest on zastosowany do dużych gliczy w pulsarach Crab i Vela. Rozważana również jest hydrodynamiczna stabilność układu poprzez badanie oscylacji nadciekłej gwiazdy neutronowej. Pokazano istnienie takich modów oscylacji, które mogą być niestabilne w reżimie laminarnym, ale są stabilizowane, gdy pojawia się turbulencja. Przedstawiono również analizę nieliniowego tarcia wzajemnego, która może być zastosowana w przypadku turbulencji oraz omówiono powstawanie turbulencji w laboratoryjnych analogach gwiazd neutronowych.

List of papers part of this thesis

1. Khomenko, V. and Haskell, B., 2018, "Modelling Pulsar Glitches: The Hydrodynamics of Superfluid Vortex Avalanches in Neutron Stars", PASA **35**, 20

2. Haskell, B. and Khomenko, V. and Antonelli, M. and Antonopoulou, D., 2018, "Crust or core? Insights from the slow rise of large glitches in the Crab pulsar", MNRAS **481**, L146

3. Khomenko, V. and Antonelli, M. and Haskell, B., 2019, "Hydrodynamical instabilities in the superfluid interior of neutron stars with background flows between the components", Phys.Rev.D, **100**, 123002

4. Celora, T. and Khomenko, V. and Antonelli, M. and Haskell, B., 2020, "The effect of non-linear mutual friction on pulsar glitch sizes and rise times", MNRAS **496**, 5564

Chapter 1

Introduction

1.1 Historical overview of neutron stars

The idea of the existence of incredibly dense objects with small radii, namely neutron stars (NSs), was first proposed in 1934 by Baade and Zwicky [1]. NSs were suggested to be products of supernovae explosions and to be made exclusively by tightly packed neutrons, discovered a few years earlier, in 1932, by Chadwick [2]. The first NS model was proposed by Oppenheimer and Volkoff [3]. It made use of a simple Equation of State (EoS) to predict masses and radii of neutron stars. The model treated matter inside the star as a perfect gas of free neutrons at high density. The first derived mass of NS was $M_{max} = 0.7\,M_{\odot}$, radius $R = 9.6$ km, central density $\rho_c = 5 \cdot 10^{15}$ g/cm^3. Though it was simplistic from today's point of view, it allowed to extract the basic order of magnitude for the physical parameters of a NS.

The aim of follow-up papers was to explore more in detail the state of matter in NS interiors, given that conditions inside are extreme and these objects can be observed on long timescales, making NSs natural laboratories of high density and low temperature physics. The composition and physical processes that occur in different regions of such high density objects were of high interest and still are. Each new model carried an additional ingredient used to construct more sophisticated and complex equations of state, which attempted to quantify the role of interactions between the nucleons, taking into account also data from terrestrial nuclear experiments. Examples of early NS equations of state are: the BBP EoS [4] that treats nucleons as a compressible fluid, the Bethe & Johnson EoS [5] that uses the limiting variational method, the Pandharipande & Smith EoS [6, 7] that takes into account tensor interactions and the model of Walecka [8, 9] which explores a relativistic mean field approximation.

Before the discovery of pulsars by Jocelyn Bell in 1968 [10] the theory of NS was not widely developed. The reason was mainly observational, and due to the fact that the small surface area of NSs cannot emit large fluxes

of visible light, while new instruments allowed for observations first in the radio and then X-ray bands, accessing the NS's high energy emission in this range. High energy emission is possible due to the large amount of energy stored in the star, and particularly because of the high rotational energy and magnetic energy. For the first time pulsar rotation periods were measured and NSs were localized in the sky. NSs were also found to be present in binary systems [11], where accretion can power high energy X-ray emission. Observations of NSs in binaries also allow to measure their masses with an increasingly high precision [12], thus allowing to constrain our models for the interior composition.

The modern point of view is that NSs are complex objects with high magnetic fields that can reach $10^{16} - 10^{17}$ G, superfluid phases in the interior and complex emission patterns in electromagnetic and gravitational waves. So the equation of state defines the static properties of the star, but alone it cannot provide a ground for understanding their behavior and evolution. Theoretical work is thus also focused on all the above mentioned aspects that determine the dynamics of the star. Moreover, understanding the influence of high magnetic fields and superfluid states in the interior allows to constrain not only the equation of state, but also to model and predict the phenomena that give rise to electromagnetic and gravitational wave emission [13]. So studies of NSs are crucial, since they may provide information on the properties of matter in conditions of high density and low temperature that cannot be reached in laboratory experiments on Earth.

1.2 General properties of neutron stars

Neutron stars are compact remnants that are endpoints of stellar evolution. They are massive objects (with masses roughly a few times that of the sun) with extremely low radii (of order 10 km) and high densities (above nuclear saturation density). NSs may be classified depending on their evolutionary track and formation history. The first distinction is whether the NSs are 'isolated' or in binaries (although an isolated NS may have been in a binary in the past). Neutron stars, located in binary systems, are generally subdivided into LMXB (Low-mass X-ray binaries), IMXB (intermediate mass pulsars) and HMXB (high mass X-ray binaries) or MSP (recycled or millisecond radio pulsars). The evolution and the progenitors may be different, but in general a NS's structure is stable with respect to the gravitational collapse mainly due to neutrons being in a so called degenerate state[1].

Neutron degeneracy is in principle analogous to the electron degeneracy, or degeneracy of the any other Fermi gas. It's an ability of particles to occupy higher energy states, because lower energy states are not available due

[1] In reality neutron degeneracy pressure alone cannot explain the observed masses of neutron stars, and nuclear interactions play a crucial role in the equation of state

to the Pauli exclusion principle. They create pressure, that can (partially) compensate the gravitational force compressing the star, even at zero temperature. Neutron and electron degeneracy have astrophysical significance, forming the basis for the explanation of the stability of white dwarfs and neutron stars, respectively.

But how is degeneracy reached? To answer this question we need to look at the evolutionary track of NS. Isolated NSs are formed after the collapse of the high-mass main sequence star (with initial masses between 10-29 M_o). A normal star (or more correctly a star on the Main Sequence) goes through the sequence of burning stages, like hydrogen burning phase (pp-chain or CNO cycle reactions), helium burning phase and further evolutionary stages [14].

Depending on the initial mass of the star, later stages may be unreachable, because the pressure inside is too small to initiate higher mass element burning. If the star is not too massive, it may collapse to a white dwarf, where degenerate electrons support the pressure enough to compensate the gravitational force. But if the star is massive enough to reach the Fe burning phase, further collapse is inevitable, due to the Fe-peak. Energetic reactions of nuclear fission are no longer exothermic and require energy in order to proceed. At this stage, the star begins to collapse and inverse beta decay allows for neutron formation. Neutron degeneracy is reached and the neutron pressure (quantum pressure) acts opposed to the gravitational force, and eventually a new stable inner configuration is reached, in which nucleons are packed close enough (at densities comparable to that of an atomic nucleus) that the short range nucleon repulsion begins to play a crucial role. This configuration is a proto-neutron star.

A proto-neutron star is an unstable configuration, because processes inside are far from equilibrium. The radius of the proto-NS is $20 - 30$ km, temperature $6 \cdot 10^{11}$ K, mass $1.2 - 2\,M_{\odot}$. It's neutrino opaque. Neutrino transparency is reached in 50 seconds after the collapse [15], arriving at the much more stable configuration, the NS itself.

The parameters of the resulting neutron star are dictated by the history of the progenitor. Examples of such a "formation history dependence" are the high magnetic fields outside and inside a neutron star. These are thought to be 'fossil' fields, as their origin lies in the conversion of the magnetic flux, given by the equation:

$$R_i^2 B_i = R_{NS}^2 B_{NS} \tag{1.1}$$

where R and B are the radius and magnetic field of the progenitor, R_{NS} and B_{NS} are the quantities for the formed NS. Since the magnetic field is conserved and the radius of the new configuration is much smaller, the resulting magnetic field is higher and is $\approx 10^{15}$ G [16]. Moreover magnetic flux tubes are believed to be present in the inner layers of a NS, as the protons in the core may form a type 2 superconductor, after the star has

cooled below $10^9 - 10^{10}$ K (see [17] for a review). The number of flux tubes is given by [18]:

$$n_\Phi = B/\Phi_0 \; 10^{19} B_{12} \text{ cm}^{-2} \tag{1.2}$$

with B_{12} magnetic field strength in units of 10^{12} G.

NSs have relatively high initial temperatures. In a first few minutes after a collapse the temperature of a NS is $\approx 10^9 - 10^{10}$K. Due to the neutrino emission and modified URCA processes, the temperature drops in time. The rate of the overall cooling also depends on the thermal emission [19]. At temperatures around $T \approx 10^8$ K photon emission becomes dominant, as the neutrino flux decreases.

The high densities (reaching values up to 10^{16} g/cm^3) and moderate temperatures of mature NSs make it possible for a superfluid condensate to be formed [17]. The presence of superfluidity has consequences on the NS's inner dynamics and alters the expected observational behavior. Superfluidity affects cooling by suppressing reaction rates [20], modifies the viscosity [21], introduces new dissipation mechanisms [22, 23] and alters the gravitational wave emission [24]. Superfluidity and superconductivity both have a large impact on the dynamics of neutron stars. Vortex - flux tube interaction in the core is an example of the combined effect of both superfluidity and superconductivity [17].

As superfluidity has many consequences on the star's dynamics, this allows for constraints to be obtained from observations. Superfluidity may be constrained from cooling [25, 26] or cooling combined with magnetic field evolution [27]. Finally, as we shall see in detail in this thesis, pulsar glitches allow for more elaborate insights into the inner fluid's dynamics [28].

1.3 Structure of neutron stars

Let's move to the structure of a neutron star. For the present discussion its interior may be virtually divided into five distinct regions: the surface with an atmosphere composed of light and heavy elements, outer and inner crust, outer and inner core. The properties of the lower density surface and atmosphere regions mainly impact on the electromagnetic emission, for example the emission from the regions near magnetic poles can be due to synchrotron radiation [29] and thermal emission from the surface depends on the atmosphere composition [30]. Electron-positron pair production in a high magnetic field may further contribute to the radiation emitted [30].

The composition and physical properties of NS regions are the following [31]:

Surface region: Layers, with densities not exceeding the density $\rho \approx 10^6$ g/cm^3, are surface layers. Depending on the composition of the surface and

atmosphere, the emission will differ, as already mentioned. The state of matter at these densities is well known from terrestrial experiments, though the uncertainties in composition may create issues in interpreting observational data.

Crust regions: are regions of a neutron star, lying between the surface and up to the layers where transition to a pure fluid occurs. The crust may be subdivided into the inner crust and outer crust. The inner crust is composed of neutron-rich atoms and cloud of electrons, and at densities of $\rho \approx 4 \cdot 10^{11}$ g/cm^3, neutrons begin to drip out of nuclei and there is a transition to the inner crust.

Free neutrons occupy continuous states as all bound states are filled up, leading to the formation of the neutron Fermi sea. Neutrons in a Fermi sea interact through the long-range attractive interaction and form Cooper pairs like electrons do in conventional s-wave superconductors [2]. Since the typical temperature of a neutron star is smaller than the estimated critical temperature for the $1S_0$ neutron pairing, usually calculated by many body interaction model, s-wave pairing may be formed in all NSs except newly-born ones [32].

Ions in the crust arrange themselves into a crystal lattice. The type of the lattice as well as lattice parameters are however unknown. Simple models suggest that the lattice is of BCC type, but due to the large stresses and high pressures the configuration is likely to be more complex [33]. There is also a probability of poly-crystalline configuration to be formed. The structure of the lattice defines the lattice strength, which is important for modeling magnetar flares, pulsar glitches and gravitational wave emission [34].

An intermediate layer between the crust and the core of the NS, containing nuclear pasta phases, in which nuclei are no longer spherical but form more complex structures, may be present. An example of structure and transition regions is shown on a fig.1.1;

Core regions: are the regions with average densities higher than the nuclear density. The exact composition of a core is unknown. Exotic phases, like pion or kaon condensation or quark matter may be present, depending on the mass of the star. Generally, the outer core is expected to be an electron, proton, neutron and muon fluid, not forming a regular lattice.

The core may contain magnetic flux tubes and superfluid neutrons in $3P_2$ state [35]. P-pairing is a complex phenomena to explain even in terrestrial conditions. An example of this state is found in superfluid Helium 3, that forms a very complex vortex pattern, with a rich order parameter and nontrivial internal topology [36]. The number of protons in the core is small, thus short range repulsion is less dominant. Therefore protons form a $1S_0$ superfluid, similar to that of conventional superconductors [37]. The number

[2] In the case of neutrons the nucleon-nucleon interaction provides the necessary attraction for Cooper pairing. For electrons phonon exchange is necessary

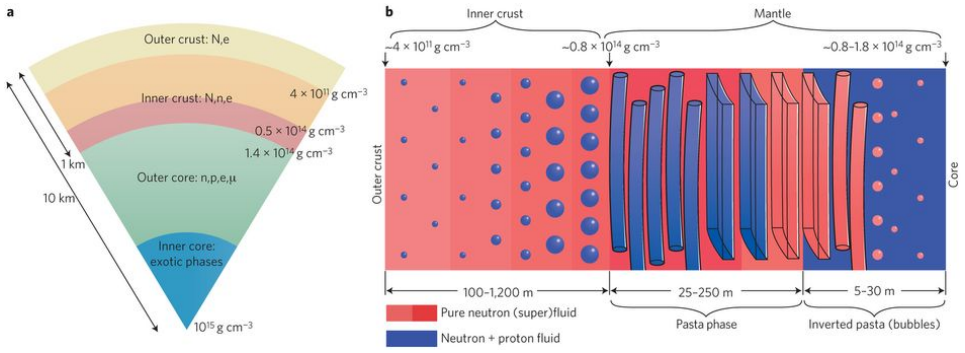

Figure 1.1: Structure of a neutron star. a) Schematic slices. n,p,e, μ stands for neutrons, protons, electrons and muons. b) Paste phases near crust-core transition regions [39].

of magnetic flux tubes greatly exceeds the number of superfluid vortices and conditions inside the core may force vortices to pin on the fluxtubes, thus storing angular momentum [38].

1.4 Emission properties of neutron stars

Following the discussion of the previous section, one may wonder how to "see" a neutron star, what kind of information can be extracted and how to interpret the observational data. In fact NS are not only 'seen' with electromagnetic radiation, but can also be 'heard' with gravitational waves, and signals from the collision of NS-NS binaries have been recently detected for the first time by the LIGO and Virgo interferometers[40, 41]. Mature neutron stars can also radiate continuous gravitational waves if they have a non zero quadrupole moment (non axisymmetric distribution of matter) [42]. In this case gravitational wave emission may depend also on the dissipation in the superfluid interior. For example the r-mode instability, a gravitational-wave driven instability, may be suppressed due to either superfluid mutual friction [43, 44], or a viscous boundary layer at the neutron star core-crust interface [45].

Let us focus on the electromagnetic emission first, as this is crucial to get some insights into the glitch theories studied in this thesis. A few mechanisms for NS EM emission have already been mentioned in the previous section. In general, isolated NSs may emit periodic and non periodic signals. Emission is seen in visible, radio and X-ray spectra, and also in near infrared and ultraviolet. If a NS emits periodic signals in any range it is called a 'pulsar'. The condition for a pulsar to be seen as a periodic signals emitter is that it emits a beam of radiation that is dragged round by rotation (like a lighthouse) and that the beam points towards the Earth, otherwise it

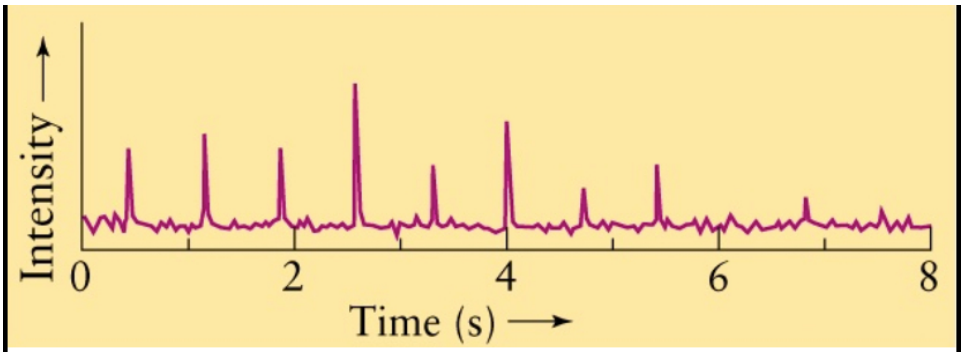

Figure 1.2: Char record of individual pulses from PSR 0329+54, recorded at frequency $410MHz$ with an instrument time constant of 20ms. The regularity of pulses is 0.714s.

will appear as a non pulsating NS[3]. The beam is powered by the rotational energy of the neutron star and the strong electromagnetic field supports the energy for acceleration of protons and electrons, located near the magnetic poles.

We will now focus on rotation powered radio pulsars, which represent the bulk of the glitching pulsar population we are interested in (although, as we shall see, glitches are present also in accretion magnetars, where the magnetic field powers the emission, and have been observed also in accretion powered pulsars).

Radio pulsars emit wideband radio signals. Pulse intensities vary over a wide range and the pulsations are periodic with a very stable frequency. A typical pulsars emission pattern is shown in 1.3. Many pulsars exhibit a high degree of linear polarization, up to 100% in some cases [46].

The simplest theoretical model of pulsar emission and spindown (in a rotational powered pulsar) is a magnetic dipole model. In this model kinetic energy from the pulsar's rotation is transformed into radiation, and the beam of radiation is swept around by rotation due to the magnetic pole to rotational axes misalignment. Irrespectively of the configuration of the inner electromagnetic field, the energy of radiation emitted is:

$$E = \frac{1}{2} I \Omega^2, \tag{1.3}$$

$$\dot{E} = I \Omega \dot{\Omega}. \tag{1.4}$$

where E is the rotational kinetic energy, I - moment of inertia, Ω is the angular frequency. We assume that the pulsar is slowing down due to the

[3]Note that this is not the only reason why a NS may not be a pulsar. Some NSs do not emit pulsed radiation at all, but emit, for example, only thermally

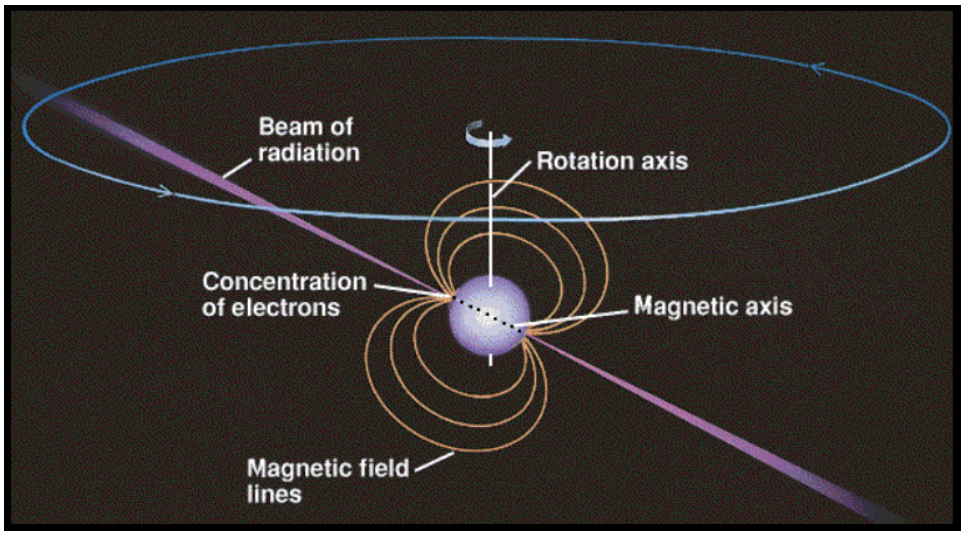

Figure 1.3: Lighthouse model of emission.

emission of electromagnetic waves, so that for dipole radiation one has now:

$$\dot{E} = \frac{B_p^2 R^6 \Omega^4 \sin^2 \alpha}{6c^3}\,, \tag{1.5}$$

where B_p is the polar surface field strength, R the radius, α the inclination angle between the magnetic and spin axis, and c the speed of light in vacuum. Typical long term spin-down rates are in the range $\dot{\nu} \approx 10^{-15} - 10^{-12}$ Hz/s, where $\nu = \frac{\Omega}{2\pi}$. A simple magnetic dipole model gives approximate information on evolution of the rotational frequency of a pulsar and allows to estimate its magnetic field strength from observations.

For any power law deceleration model, such a magnetic dipole model, one can write:

$$\dot{\Omega} = -(constant) \cdot \Omega^n \tag{1.6}$$

where n is called a breaking index. In general the relation for a breaking index is:

$$n = \frac{\Omega\ddot{\Omega}}{\dot{\Omega}^2}; \tag{1.7}$$

thus it may be measured from the pulsar frequency and its derivatives. The breaking index encodes the process, responsible for the emission [47]. For example breaking index $n = 1$ corresponds to the loss of rotational energy due to mainly relativistic particles winds. A breaking index $n = 3$ to magnetic dipole radiation. A breaking index $n = 5$ corresponds to energy loss due to GW radiation from mountains, and $n = 7$ to GW energy loss

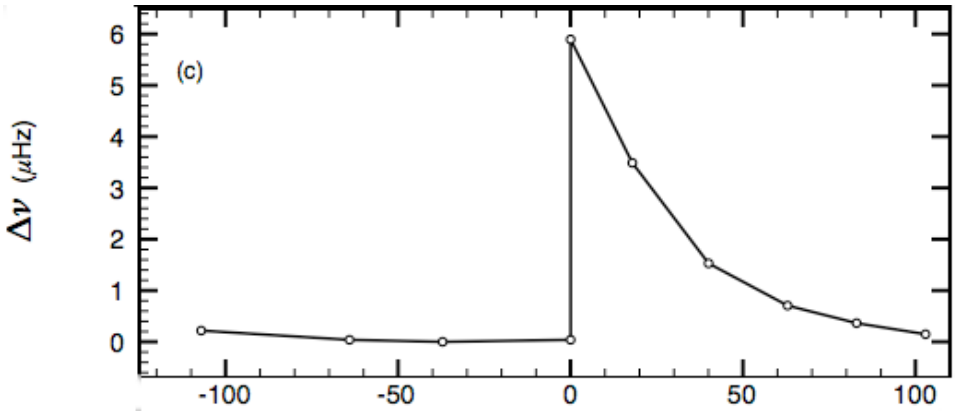

Figure 1.4: Frequency residuals showing a glitch in the PSR B0531+21 (Crab pulsar), occurred around MJD 53067, with a fractional frequency jump of $\Delta\nu/\nu = 5.33 \pm 0.05 \cdot 10^{-9}$ [49].

due to a constant amplitude r-mode. Breaking indices differ from pulsar to pulsar but in general lay in ranges $1 < n < 3$ with a few exceptions, although observationally $\ddot{\Omega}$ is hard to measure [48].

1.5 Why can emission patterns sometimes be puzzling?

A pulsar is almost a perfect rotator. Due to the emission of electromagnetic radiation it loses energy and spins down. If no inner or outer processes alter this behavior, the spindown rate will evolve gradually according to a spindown law such as that in (1.6). But that's where the "almost" part comes in. Sometimes the spin frequency suddenly increases. This increase is called a "pulsar glitch". In addition to that, another phenomenon can occur, an antiglitch, when on the contrary, the spin frequency decreases. These are seen rarely, and generally not in radio pulsars, but rather in magnetars or accreting pulsars. Not less remarkable is timing noise which is the more gradual change of ν and $\dot{\nu}$. In order to study these processes and characterize the rotational behavior of a pulsar the timing technique is used.

1.5.1 Pulsar timing

The pulsar timing method allows to characterize the pulsar rotation. To "time" a pulsar means to measure the times of arrival (TOA) of successive pulses, in order to extract the period of rotation (and its derivatives) of the star. Since we are receiving signals as part of a moving system (on Earth), this movement should be excluded by transferring TOAs into an "inertial" reference frame, that removes the effects of the orbital motion of Earth.

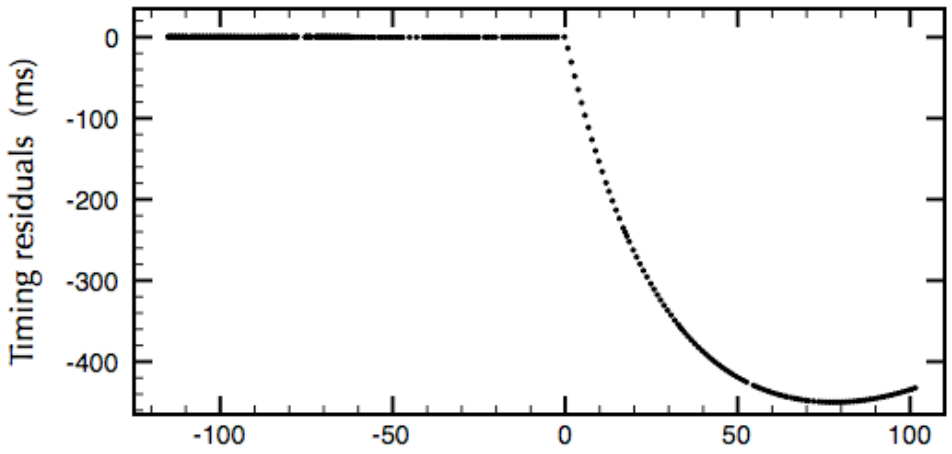

Figure 1.5: The timing residuals relative to a slowdown model, for a glitch in PSR B0531+21 [49].

Other effects should be taken into account as well, such as the effect of dispersion in different frequency bands. Having obtained a set of TOAs, a model for the intrinsic properties of the pulsar, including its astrometric, rotational, interstellar and (if applicable) binary parameters, is applied in order to predict the barycentric pulse arrival time. The difference between the observed and predicted arrival times is known as the timing "residual". Study of the time and radio-frequency variations of these residuals is the basis of the pulsar timing technique [50].

For the about 2600 pulsars known [51], timed pulse periods were measured. They lie in a range between 1 ms and 15 s, with most lying between 0.3 s and 3 s, the so-called "normal pulsars". On the other hand, the "millisecond pulsars" (MSPs), form a distinct group, roughly with periods in the range 1 ms to 10 ms, which are thought to have been recycled to rapid rotation rates by accretion in a binary [52].

Since the timing residuals contain a model of the pulsar spin-down, their systematic variations indicate either errors in the model used or the presence of unmodelled phenomena affecting the observed TOAs. Pulsar glitches are this kind of phenomena (an example is shown in 1.4). Timing residuals, that correspond to a chosen model of spin-down, fluctuate around zero before the glitch occurs. Just after the glitch, timing residuals become negative, so pulses are arriving "early" and the model is no longer valid as the consequence of the star's rotational frequency change (shown in 1.5).

1.5.2 Pulsar glitches / antiglitches

About 425 glitches have been observed in more than 140 pulsars [53]. The relative magnitudes are in a ranges $\Delta\nu_g/\nu \approx (10^{-10} - 3\cdot10^{-5})$. The distribu-

tion of 180 glitching pulsars is shown in 1.6. Glitches in young pulsars and magnetars are typically large with $\Delta\nu_g/\nu \approx 10^{-6}$. However the youngest pulsars, the Crab pulsar, PSR J0537-6910, PSR J0540-6919 tend to have more frequent and smaller glitches with $\Delta\nu_g/\nu \approx 10^{-7} - 10^{-8}$. The most frequent glitcher is located in the Large Magellanic Cloud, PSR J0537-6910. It glitches about three times per year [54]. Regarding the millisecond pulsars only two of them have been observed to glitch and the glitches are small $\Delta\nu_g/\nu \approx 10^{-11}$.

"Large" glitches are common in magnetars. They are "large" in terms of $\Delta\nu_g/\nu$, because typically the ν in magnetars is small. The magnitudes $\Delta\nu_g$ of glitches are similar to those in other young pulsars, but with some additional features presented. Sometimes they're accompanied by radiative changes, either X-ray bursts or associated changes in the pulse profile [55]. Though such phenomena are common for all magnetars and happen frequently, only a small portion of them is associated with glitches. Generally in the "normal" pulsars glitches are not associated with radiative changes.

Antiglitches were observed in accreting pulsars. An example are ones in ultraluminous accreting pulsar NGC 300 ULX 1 [56]. This is remarkable, because no spectral changes at the epoch of the glitches were detected, supporting the evidence that antiglitches may be of the same nature as glitches.

Glitches can differ significantly from one another, not only in size and frequency, but also in the rise and post-glitch relaxation of the star. Some appear as simple steps in frequency, while others also display an increase in spin-down rate after the glitch, or several exponentially relaxing components in the post-glitch recovery [58]. The timescale on which a glitch occurs is short and so far can be constrained only. The most stringent limit obtained is of roughly 10 seconds for the Vela pulsar [59, 60]. Another feature or unusual behavior can be found in some glitches of the Crab pulsar (with lower limit for a rise time constrained as high as 6 hours [61]), where a delayed spin-up occurs after the glitch itself.

Glitch statistics are also of particular interest. It has been suggested that the glitch size distribution is bimodal, so that there should be more that one glitch population, possibly with a multiple glitch mechanisms [62], although in this thesis we will discuss how non-linear coupling between the components in the star can explain the distribution with a single mechanism (possibly occurring in different regions of the star) [63, 64, 65]. The glitch distribution is shown in fig.1.7.

Pulsar glitches can also be used to constrain pulsar masses [66], NS crust-core coupling during the glitch [67] and the physics of neutron star crusts [68]. There could also be a connection between glitches and NS precession [69]. On the other hand the glitch trigger mechanism allows to get insight into a complex statistical processes inside the star, involving the interactions between vortices and large scale motion of fluids [28], as we will also show in

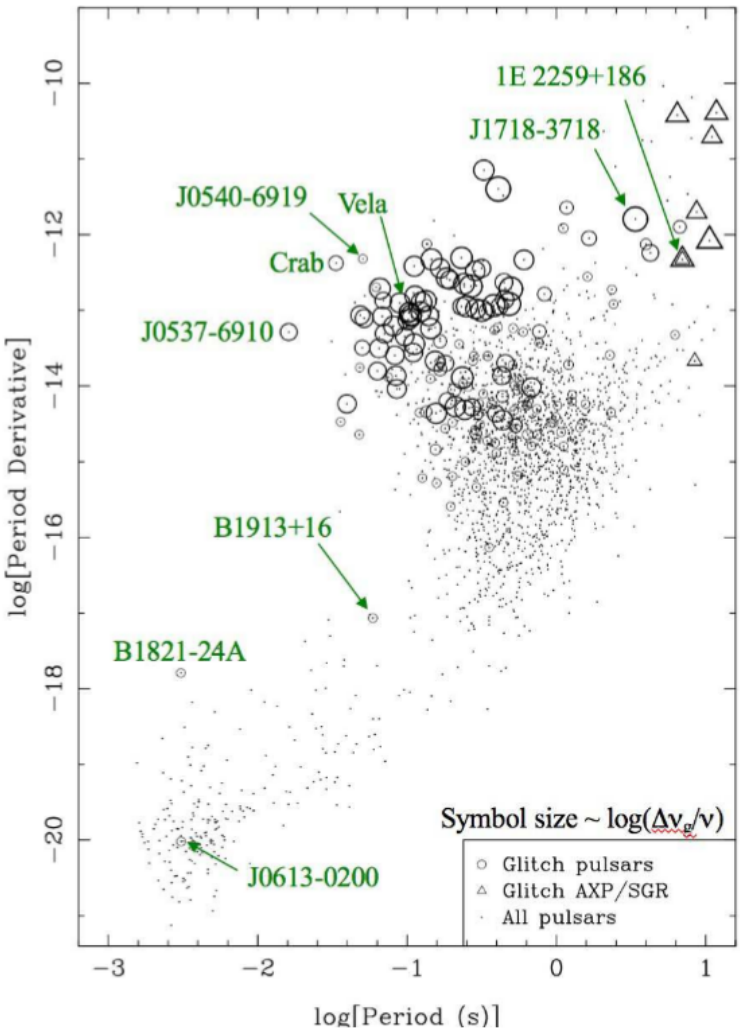

Figure 1.6: Glitching pulsars in the $P - \dot{P}$ diagram [57]

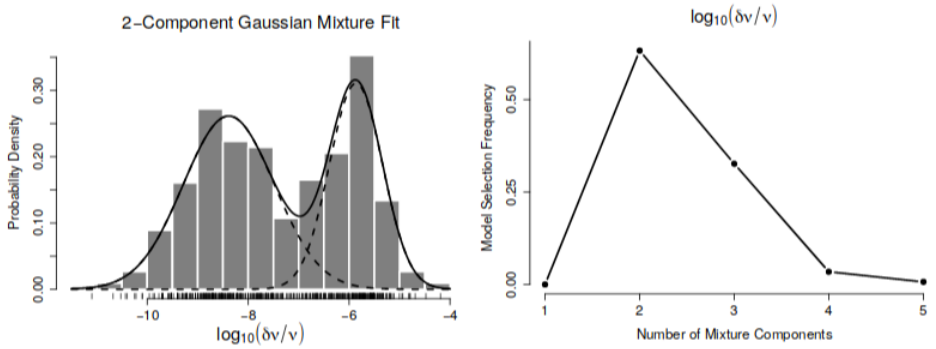

Figure 1.7: Distribution of glitch sizes, which is well fit by 2 gaussians and appears bimodal. [73]

this thesis [70]. Glitch models can be used to investigate superconductivity in a NS's interior [71] and superfluid coupling [72]

1.5.3 Timing noise

Another (apart from glitches) interesting and 'mysterious' deviation from the steady spin-down behavior is timing noise. Timing noise is a type of rotational irregularity which causes the pulse arrival times to wander stochastically about a steady spin-down state [74]. Timing noise manifests itself as a red-noise process in the ToAs, implying an autocorrelated process on a time-scale of months to years. Essentially, however, any "unexplained" deviations from the spin-down model that are not sudden, like glitches, are attributed to "timing noise".

The physical processes, responsible for the timing noise generation remain undefined, but there are some hypotheses. The timing noise may be connected with starquakes, the random pinning and unpinning of vortex lines (hard superfluidity), accretion from the interstellar medium, vortex annihilation at the outer boundary of the superfluid, pulse-shape changes [75] and also due to superfluid turbulence [76].

1.6 Overview on superfluids

As it was outlined before, superfluidity is likely to play a very important role in a NSs evolution and its life cycle. A more general overview is given in this section, because superfluidity requires more attention from the theoretical point of view to develop the models discussed in this thesis. From a hydrodynamical point of view, superfluidity is a state of a fluid, in which there is no classical viscosity associated with its flow. From the quantum-mechanical

(statistical) point of view, a superfluid is Bose or Fermi condensate, containing quasiparticles that do not interact with one another [77].

Superfluidity was discovered experimentally by Kapitsa and Allen [78]. The first theoretical model was suggested by Landau [79]. The first discussion for neutron stars was made by Migdal [80]. The experiments of Kapitsa were carried out in helium 4. At a temperature of 2.19 K (so called λ-point), helium 4 experiences a phase transition of the second order into a superfluid state. Later on, superfluidity in helium 3 was found to occur at much smaller temperatures. Novel experiments usually deal with ultracold atomic gases, that represents a dilute Bose condensates, which can be interpreted with the Bogoliubov theory [81].

Basically two theoretical formulations of superfluidity exist, either starting from a microscopic or from a macroscopic point of view.

1.6.1 Microscopic approach for superfluidity

The microscopic formulation starts from the second quantization, to calculate the superfluid properties needed for a macroscopic theory. For example Landau's theory is build up on the macroscopic two fluid model, where the fluids are a superfluid and a fluid of excitations (or thermally excited states). The latter is composed of quantized sound waves (phonons) and rotons. If the temperature increases the mass density of normal fluid increases, while the mass density of a superfluid decreases. These fluids are not "real". They rather express the two kinds of motion, the superfluid and the normal one [82]. The procedure of calculation of the superfluid properties is based on averaging the second quantized operators.

At finite temperatures superfluid should have a Bose energy spectrum [83], with statistical distribution of elementary excitations given by the Bose distribution:

$$n(p) = [e^{\epsilon(p)/T} - 1]^{-1}. \tag{1.8}$$

The thermodynamic quantities are calculated from the distribution.

Globally a superfluid cannot rotate like an ordinary fluid does. If we put a normal fluid in a rotating bucket, it follows the bucket's rotation and starts to rotate as well, because of the friction between the fluid and bucket's surface. The superfluid, however, doesn't rotate as whole. It forms vortex lines to carry the circulation. Mathematically this means the following. The superfluid velocity field is given by:

$$v_s(r,t) = \frac{h}{m}\nabla S(r,t) \tag{1.9}$$

where v_s is the superfluid velocity, S phase of the condensate. Taking the curl:

$$curl(v_s) = \frac{h}{m}\nabla \times \nabla S(r,t) = 0 \tag{1.10}$$

so the fluid is irrotational. This is a consequence of the quantization of circulation. However rotational energy tends to be minimized.

$$E_{rot} = E - M\Omega \tag{1.11}$$

E and M are energy and momentum in the laboratory frame, and E_{rot} in a rotating coordinate system. If Ω is non zero, the state with $M\Omega > 0$ is energetically favorable. The only way to reach it is to create a local motion. This motion should preserve global $rot(v_s) = 0$. From a kinematic point of view this means creating a vortex with a finite hydrodynamical circulation, defined by:

$$k = \oint_c v_s \cdot dr \tag{1.12}$$

with k - quantum of circulation. The velocity distribution around the vortex line is given by:

$$v_s = \frac{k}{2\pi r} \tag{1.13}$$

where r is the radius vector from the vortex to a point where the velocity is observed. A quantum vortex line cannot be discontinuous. It is either a closed loop or should start and end on a surface. An important property of a vortex line is that it may be energetically favorable to 'pin' on the crystal lattice atoms in the crust (or to fluxtubes in the core). As we shall see, this effect is used to explain the origin of a glitch in most models [28].

1.6.2 Macroscopic formulation of superfluidity

The standard macroscopic formulation is based on the hydrodynamical equations for a two-fluid system, where one fluid is a superfluid, and another is a normal fluid [84]. A more complete multi-fluid approach, which is the basis for advanced studies of neutron stars is considered in a next section. The standard two fluid hydrodynamics starts with a flux density for the components (we use tensor notation where summation over repeated indices is assumed):

$$j = \rho_s v_s + \rho_n v_n \tag{1.14}$$

where s labels the superfluid component, n normal component. The density in turn is:

$$\rho = \rho_n + \rho_s \tag{1.15}$$

Conservation laws are:

$$\frac{\partial j_i}{\partial t} + \frac{\partial \Pi_{ik}}{\partial r_k} = 0 \tag{1.16}$$

$$\frac{\partial \rho}{\partial t} + \nabla^i j_i = 0 \tag{1.17}$$

with Π_{ik} is a momentum flux tensor defined below in 1.21. Furthermore the flow is potential and entropy S (carried by the normal fluid) is conserved, so that:

$$\frac{\partial S}{\partial t} + \nabla^i(Sv_i^n) = 0 \tag{1.18}$$

$$\frac{\partial v_s}{\partial t} + \nabla(\frac{v_s^2}{2} + \mu) = 0 \tag{1.19}$$

where μ is the chemical potential. The conservation laws, together with the equations for the pressure and for the momentum flux tensor, given a temperature T:

$$p = \frac{\partial(E_0 V)}{\partial V} = -E_0 + TS + \mu\rho + \rho_n(v_n^i - v_s^i)(v_i^n - v_i^s) \tag{1.20}$$

$$\Pi_{ik} = \rho_n v_{ni} v_{nk} + \rho_s v_{si} v_{sk} + p\delta_{ik} \tag{1.21}$$

form the full hydrodynamical system of equations. The energy functional E_0 here is important and differs from that of a one fluid system, and is given by:

$$dE_0 = \mu d\rho + Td(\rho s) + (v_n - v_s)dj_0 \tag{1.22}$$

with

$$j_0^i = \rho_n(v_n^i - v_s^i) \tag{1.23}$$

Dissipative processes are usually taken into account by including additional linear terms, containing derivatives of velocity and temperature. The form of the terms then should satisfy the Onsager symmetry principle, in which the entropy of a system can only grow in time [85, 86].

An equivalent, but more versatile model, usually applied for neutron stars is used in this thesis and will be discussed in the next section. It is the one based on a flux-conservative formalism for convective and dissipative multi-fluid systems [85]. It allows to take into account more degrees of freedom (i.e. more components of the star), although in most glitch models the two fluid case is indeed applied. Unlike in the Landau model, the fluids are "real", i.e. they represent the fluxes of actual massive particles. The mediator between the fluids is the mutual friction force that includes both dissipative and conservative terms, and is due to the interaction between the vortices and the superfluid and normal components. An additional non-dissipative coupling between the fluids is represented by the entrainment effect [87, 88], which leads to the transport velocities and momenta of a fluid not being necessarily aligned.

1.6.3 A two fluid superfluid hydrodynamics of NSs

A hydrodynamical model is applicable to length-scales bigger then inter-vortex spacing, so we do not deal with the dynamics of individual vortices directly, but rather with averaged large scale degrees of freedom that describe superfluid neutron velocities and densities, and those of a charge neutral fluid of protons and electrons. For the purpose of investigating the timescales associated with glitches, protons and electrons are assumed to be locked by electromagnetic interactions and flow as a single fluid [89]. Following [17], conservation laws for each species are:

$$\partial_t \rho_{\rm x} + \nabla_i(\rho_{\rm x} v^i_{\rm x}) = 0, \tag{1.24}$$

where the constituent index x labels either protons (p) or neutrons (n), $v^i_{\rm x}$ is the velocity and $\rho_{\rm x}$ is a density of respective constituent x. Summation over repeated indices is implied. The Euler equations are the following:

$$\begin{aligned}&(\partial_t + v^j_{\rm x}\nabla_j)(v^{\rm x}_i + \varepsilon_{\rm x} w^{\rm yx}_i) + \nabla_i(\tilde{\mu}_{\rm x} + \Phi) + \varepsilon_{\rm x} w^j_{\rm yx}\nabla_i v^{\rm x}_j \\ &= f^{\rm x}_i/\rho_{\rm x},\end{aligned} \tag{1.25}$$

with $w^{\rm yx}_i = v^y_i - v^x_i$ and $\tilde{\mu}_{\rm x} = \mu_{\rm x}/m_{\rm x}$ is the chemical potential per unit mass ($m_{\rm p} = m_{\rm n}$ is taken). The gravitational potential is Φ and $\varepsilon_{\rm x}$ is the entrainment coefficient, that's particularly important in the crust [90], [91]. The term on the right hand side $f^{\rm x}_i$ is the vortex-mediated mutual friction, which, for straight vortices and laminar flows, takes the form of the Hall–Vinen–Bekarevich–Khalatnikov (HBVK) mutual friction [17]:

$$f^{\rm x}_i = \kappa n_{\rm v}\rho_{\rm n}\mathcal{B}'\epsilon_{ijk}\hat{\Omega}^i_{\rm n} w^k_{\rm xy} + \kappa n_{\rm v}\rho_{\rm n}\mathcal{B}\epsilon_{ijk}\hat{\Omega}^j_{\rm n}\epsilon^{klm}\hat{\Omega}^{\rm n}_l w^{\rm xy}_m, \tag{1.26}$$

where the vorticity is assumed to be parallel to $\Omega^j_{\rm n}$, the angular velocity of the neutron superfluid (a hat represents a unit vector), $\kappa = h/2m_{\rm n}$ is the quantum of circulation and $n_{\rm v}$ is the vortex density per unit area, ϵ_{ijk} is the Levi-Civita symbol.

The parameters $\mathcal{B}$ and $\mathcal{B}'$ in the expression for the mutual friction in (1.26) can be expressed in terms of a dimensionless drag parameter $\mathcal{R}$ and are defined as

$$\mathcal{B} = \frac{\mathcal{R}}{1+\mathcal{R}^2} \quad \text{and} \quad \mathcal{B}' = \frac{\mathcal{R}^2}{1+\mathcal{R}^2}. \tag{1.27}$$

The parameter $\mathcal{R}$ encodes the microphysics of the dissipation processes that take place in the stellar interior, and its value is highly uncertain, ranging from $\mathcal{R} \approx 10^{-10}$ for phonon scattering in the crust [92], to $\mathcal{R} \approx 10^{-4}$ for electrons scattering of vortex cores in the neutron star core [93] or as high as $\mathcal{R} \approx 1$ for Kelvon scattering in the crust [94]. Nevertheless the exact value of $\mathcal{R}$ is not crucial for the following discussion, and we will in general assume that $\mathcal{R} \ll 1$, and indicate the values we use explicitly in the examples provided.

The Feynman-Onsager relations link vortex density at a cylindrical radius ϖ to the rotation rate of a superfluid element:

$$\kappa n_{\rm v}(\varpi) = 2\left[\Omega_{\rm n} + \varepsilon_{\rm n}(\Omega_{\rm p} - \Omega_{\rm n})\right] + \varpi \frac{\partial}{\partial \varpi}\left[\Omega_{\rm n} + \varepsilon_{\rm n}(\Omega_{\rm p} - \Omega_{\rm n})\right] \tag{1.28}$$

The previous description is valid for a laminar flow and straight vortices. If the superfluid however is turbulent a vortex tangle will develop, and for isotropic turbulence the mutual friction takes the form of Gorter-Mellink mutual friction [95]

$$f^i_{\rm x} = -\frac{\rho_n}{\rho_{\rm x}} A_{GM} w^2_{\rm xy} w^i_{\rm xy} \tag{1.29}$$

where the parameter A_{GM} has the dimensions of the inverse of a circulation and $w^2_{\rm xy} = w^i_{\rm xy} w^{\rm xy}_i$. The functional form in this case is different (and a reasonable approximation also in the case of polarized turbulence in a pinned superfluid [96]), and will affect the observed behaviour of the fluid during a glitch [97, 98].

1.7 Superfluidity and Pulsar glitches

Most glitch models are based on the ability of vortex lines to store angular momentum, when vortices are pinned to the crystal lattice in the crust of a star, or to magnetic fluxtubes in a core. The number of vortex lines in a typical NS is huge. Introducing the spin period P in units 10 ms, $P_{10} = P/(10\,{\rm ms})$, the surface density of vortices [99] is of order of:

$$n_v \approx \frac{2\Omega_n}{\kappa} \approx 6 \times 10^5\, P_{10}^{-1}\,{\rm cm}^{-2}. \tag{1.30}$$

The average inter-vortex distance is:

$$d_v = \frac{1}{\sqrt{n_v}} \approx 1 \cdot 10^{-3}\, P_{10}^{1/2}\,{\rm cm} \tag{1.31}$$

If there were no pinning, vortices would gradually move to the surface, constantly spinning down the superfluid together with the normal component of the star. In the presence of pinning vortices cannot move out, and the superfluid cannot spin down. It stores angular momentum until vortices are forced to unpin. The exact unpinning trigger mechanism, that acts in NS interiors is not known, moreover a number of mechanisms has been proposed. They are crust quakes [100], thermally activated unpinning [101], two fluid instabilities [102] and vortex avalanches. A detailed study of unpinning triggers, based on Gross-Pitaevkiy simulations, was carried out by [103]. The authors found three unpinning triggers that can lead to vortex avalanches: rotational shear between the bulk condensate and the pinned

vortices (i.e. hydrodynamical lift forces), a vortex proximity effect driven by the repulsive vortex-vortex interaction, and sound waves emitted by moving and re-pinning vortices. Triggers may also be associated with fluid instabilities, for example the r-mode instability [104], or two-fluid instabilities, as we discuss in this thesis [70].

A very important ingredient of a glitch model is the ability of a vortex line to pin, until a certain threshold is reached. In order to calculate this one needs to calculate the pinning force between vortices and ions in the crust, or flux tubes in the core. This is a complex problem, as it depends on the interaction between a vortex and many pinning sites, but recent calculations for pinning in the crust, based both on static models and on time evolutions, suggest, despite the uncertainties, pinning forces, that are large enough to explain the observed glitch size [105, 106]. Vortex unpinning can also be approximated, in a model agnostic way, as a state-dependent, compound Poisson process in a single random variable, the spatially averaged crust-superfluid lag [107].

Once vortices unpin, they contribute to the mutual friction and recouple the components of the star. The coupling between the vortices and the "normal" components can be studied using glitch recoveries [108]. If glitches are due to large scale unpinning of superfluid vortices, the different regions in which this occurs and respective timescales on which they recouple can lead to the various observed signatures, and in fact some glitches show several exponentially relaxing components in the post-glitch recovery which can be used to constrain the physics of the different regions of the star.

Pulsar glitches are traditionally viewed as a manifestation of vortex dynamics associated with a neutron superfluid reservoir confined to the inner crust of the star. But the non-dissipative entrainment coupling between the neutron superfluid and the nuclear lattice may lead to a less mobile crust superfluid, effectively reducing the moment of inertia associated with the angular momentum reservoir. Combining the latest observational data for glitching pulsars with theoretical results for the crust entrainment, Andersson et al. [109] found that the required superfluid reservoir exceeds that available in the crust, so a core region superfluid should be taken into account.

Involving the flux-tube to neutron superfluid vortex line coupling in the core of the star allows to increase the angular momentum accessible for a glitch. A first consequence of the magnetic fluxtubes inclusion is a stronger coupling between the neutron superfluid in the core and the charged component of the star, leading to substantially shorter dynamical coupling times than without vortex lines [110], giving by the equation:

$$\frac{\tau_{pin}}{\tau} \approx 3.2 \times 10^{-7} - 8 \times 10^{-10} \tag{1.32}$$

where τ is the dynamical relaxation time and τ_{pin} is the dynamical timescale

over which the two fluids couple. This is however the case if vortices are free to cut through fluxtubes. If the Magnus force is not strong enough it remains favourable for vortices to pin to the fluxtubes, storing angular momentum, in the same way as described for the crust [38]. Also, outward(inward) motion of core superfluid neutron vortices during spin-down(up) may alter the core's magnetic field, resulting in movements of the stellar crust and changes in the star's surface magnetic field which reflect those in the core below, and can relax by large scale crust-cracking events [111].

Vortex-interface glitch generation [112] is possible on the crust-core interface in neutron stars, which acts as a potential barrier to the peripheral neutron vortices approaching the interface, in the model in which these are coupled to the proton vortex clusters. As a result of the stopping of the continuous neutron vortex current through the interface, angular momentum is stored in the superfluid layers in the vicinity of the crust-core interface during the inter-glitch period. Discontinuous annihilation of proton vortices on the boundary restores the neutron vortex current and spins up the observable crust on short time-scales, leading to a glitch.

Let us discuss in more detail the glitch models mentioned above and start with superfluid vortex avalanches models. They are based on the observations of a scale-invariant glitch statistics in individual pulsars, with exponential waiting-time and power-law size distributions in most cases, that are consistent with a critical self organization process, wherein superfluid vortices pin meta-stably in macroscopic domains and unpin collectively via nearest-neighbor avalanches [113]. Vortex hopping leads to avalanches [114]. In this process a vortex unpins from a pinning site, skipping multiple pinning sites and coming close enough to a neighbors, triggering avalanches, or simply hopping from one pinning site to another giving rise to a more gradual creep [115]. Scale-invariant vortex avalanches may occur when knock-on can take place. The observed glitch size distributions cannot be reproduced if superfluid vortices unpin independently via a Poisson process [116]. Alternatively, considering a macroscopic homogeneous distribution of lattice sites and defects, noncritical self-organization process may operate (coherent noise) [117].

Statistical tests on the hypothesis that glitches are resulting from an avalanche process (with 285 events from 101 pulsars) demonstrated, that the size distribution in individual pulsars is consistent with being scale invariant, as expected for an avalanche process. The measured power-law exponents fall in the range $-0.1 \leqslant a \leqslant 2.4$ with $a \approx 1.2$ for the youngest pulsars [118]. But the problem is more complex, since the effect of vortex coupling to the neutron and proton fluids in the neutron star may lead to deviations from power-law distributions for sizes, and from exponential distributions for waiting times, as was found in hydrodynamic simulations of Haskell [119] and may be caused by non linear terms in the mutual friction, as discussed in this thesis [65]. This can also explain why the glitches in a few pulsars like

Vela do not appear to be the result of a scale invariant process, but rather are quasi-periodic [120, 121].

Another group of models are based on the two fluid hydrodynamics. Modelling pulsar glitches with realistic pinning forces using the two fluid approach [122, 72] showed, that all stages of Vela glitches, from the rise to the post-glitch relaxation, can be reproduced with a set of physically reasonable parameters and that the sizes and waiting time between giant glitches in other pulsars are also consistent with the model, although in this case all pulsar glitches should be quasi-periodic. The model of Antonelli and Pizzochero [123] uses the projection from exactly 3D hydrodynamical problem to a 1D cylindrical problem. The result is a system of differential equations that take consistently into account the stratified spherical structure of the star, the dynamical effects of non-uniform entrainment, the differential rotation of the superfluid component and its coupling to the normal crust.

A model that can fully describe all the scales in a superfluid NS interior and the whole range of glitching behaviour of the pulsar population is still elusive. In this thesis I present a set of four papers that make progress in this direction.

The first paper [63], studies the effect of vortex accumulation at the edge of pinning regions, which introduces additional non linear terms in the equations for the vortex density, and changes the structure of the equations, giving rise to travelling waves, which can model at the hydrodynamical level the propagation of vortex avalanches at the microscopic scale.

The second paper [64] applies this model to glitch rises of the Crab and Vela pulsar, and shows that it can reproduce the slow rise of Crab glitches if the glitches are triggered in the crust, and the rapid rise of Vela glitches if glitches are triggered in the core of the star. This suggests that glitches of these two pulsars may originate in different regions of the NS.

The third paper [70] studies instabilities in a superfluid system, showing how these may indeed trigger a glitch when the flow is laminar, but then are stabilized if turbulence develops after the glitch. The timescale for the decay of the turbulence may then dictate the timescale to the next glitch.

The fourth paper [65] investigates the effect of nonlinear mutual friction in more detail, both for the case of turbulence and for the case of kelvon mediated mutual friction in the crust. The results show how realistic nonlinear forms for the mutual friction can naturally give rise to a bimodal glitch size distribution in pulsars, and explain why some pulsars appear to glitch quasi periodically while others do not.

Bibliography

[1] W. Baade and F. Zwicky. Cosmic Rays from Super-novae. *Proceedings of the National Academy of Science*, 20(5):259–263, May 1934. doi: 10.1073/pnas.20.5.259.

[2] J. Chadwick. The Existence of a Neutron. *Proceedings of the Royal Society of London Series A*, 136(830):692–708, June 1932. doi: 10.1098/rspa.1932.0112.

[3] J. R. Oppenheimer and G. M. Volkoff. On Massive Neutron Cores. *Physical Review*, 55(4):374–381, February 1939. doi: 10.1103/PhysRev.55.374.

[4] Gordon Baym, Hans A. Bethe, and Christopher J. Pethick. Neutron star matter. Nucl. Phys. A, 175(2):225–271, November 1971. doi: 10.1016/0375-9474(71)90281-8.

[5] H. A. Bethe and M. B. Johnson. Dense baryon matter calculations with realistic potentials. Nucl. Phys. A, 230(1):1–58, September 1974. doi: 10.1016/0375-9474(74)90528-4.

[6] V. R. Pandharipande and R. A. Smith. Nuclear matter calculations with mean scalar fields. *Physics Letters B*, 59(1):15–18, October 1975. doi: 10.1016/0370-2693(75)90143-4.

[7] V. R. Pandharipande, D. Pines, and R. A. Smith. Neutron star structure: theory, observation, and speculation. ApJ, 208:550–566, September 1976. doi: 10.1086/154637.

[8] J. D. Walecka. A theory of highly condensed matter. *Annals of Physics*, 83:491–529, January 1974. doi: 10.1016/0003-4916(74)90208-5.

[9] J. D. Walecka. Equation of state for neutron matter at finite T in a relativistic mean-field theory. *Physics Letters B*, 59(2):109–112, October 1975. doi: 10.1016/0370-2693(75)90678-4.

[10] A. Hewish, S. J. Bell, J. D. H. Pilkington, P. F. Scott, and R. A. Collins. Observation of a Rapidly Pulsating Radio Source. Nature, 217(5130):709–713, February 1968. doi: 10.1038/217709a0.

[11] R. Giacconi, H. Gursky, E. Kellogg, E. Schreier, and H. Tananbaum. Discovery of Periodic X-Ray Pulsations in Centaurus X-3 from UHURU. *Astrophysical Journal l*, 167:L67, July 1971. doi: 10.1086/180762.

[12] P. B. Demorest, T. Pennucci, S. M. Ransom, M. S. E. Roberts, and J. W. T. Hessels. A two-solar-mass neutron star measured using Shapiro delay. Nature, 467(7319):1081–1083, October 2010. doi: 10.1038/nature09466.

[13] James M. Lattimer and Madappa Prakash. Neutron star observations: Prognosis for equation of state constraints. Phys. Rep., 442(1-6):109–165, April 2007. doi: 10.1016/j.physrep.2007.02.003.

[14] Maurizio Salaris and Santi Cassisi. *Evolution of Stars and Stellar Populations*. 2005.

[15] J. A. Pons, S. Reddy, M. Prakash, J. M. Lattimer, and J. A. Miralles. Evolution of Proto-Neutron Stars. *The Astrophysical Journal*, 513(2): 780–804, Mar 1999. doi: 10.1086/306889.

[16] S. A. Olausen and V. M. Kaspi. The McGill Magnetar Catalog. *The Astrophysical Journal Supplement*, 212(1):6, May 2014. doi: 10.1088/0067-0049/212/1/6.

[17] Brynmor Haskell and Armen Sedrakian. *Superfluidity and Superconductivity in Neutron Stars*, volume 457 of *Astrophysics and Space Science Library*, page 401. 2018. doi: 10.1007/978-3-319-97616-7_8.

[18] Malvin Ruderman, Tianhua Zhu, and Kaiyou Chen. Neutron Star Magnetic Field Evolution, Crust Movement, and Glitches. *The Astrophysical Journal*, 492(1):267–280, Jan 1998. doi: 10.1086/305026.

[19] Sachiko Tsuruta. Temperature of neutron stars. *International Journal of Modern Physics D*, 25(10):1630026, Jul 2016. doi: 10.1142/S0218271816300263.

[20] Dmitrii G. Yakovlev, Kseniya P. Levenfish, and Yurii A. Shibanov. REVIEWS OF TOPICAL PROBLEMS: Cooling of neutron stars and superfluidity in their cores. *Physics Uspekhi*, 42(8):737–778, Aug 1999. doi: 10.1070/PU1999v042n08ABEH000556.

[21] N. Andersson, G. L. Comer, and K. Glampedakis. How viscous is a superfluid neutron star core? *Nuclear Physics A*, 763:212–229, Dec 2005. doi: 10.1016/j.nuclphysa.2005.08.012.

[22] Gregory Mendell. Superfluid Hydrodynamics in Rotating Neutron Stars. II. Dissipative Effects. *The Astrophysical Journal*, 380:530, Oct 1991. doi: 10.1086/170610.

[23] B. Haskell, N. Andersson, and G. L. Comer. Dynamics of dissipative multifluid neutron star cores. *Physical Review D (Particles, Fields, Gravitation, and Cosmology)*, 86(6):063002, Sep 2012. doi: 10.1103/PhysRevD.86.063002.

[24] A. Melatos and C. Peralta. Gravitational Radiation from Hydrodynamic Turbulence in a Differentially Rotating Neutron Star. *The Astrophysical Journal*, 709(1):77–87, Jan 2010. doi: 10.1088/0004-637X/709/1/77.

[25] Spencer Beloin, Sophia Han, Andrew W. Steiner, and Dany Page. Constraining Superfluidity in Dense Matter from the Cooling of Isolated Neutron Stars. *arXiv e-prints*, art. arXiv:1612.04289, Dec 2016.

[26] D. G. Yakovlev, O. Y. Gnedin, A. D. Kaminker, and A. Y. Potekhin. Cooling of Superfluid Neutron Stars. In W. Becker, H. Lesch, and J. Trumper, editors, *Neutron Stars, Pulsars, and Supernova Remnants*, page 287, Jan 2002.

[27] A. Y. Potekhin and G. Chabrier. Magnetic neutron star cooling and microphysics. *Astronomy and Astrophysics*, 609:A74, Jan 2018. doi: 10.1051/0004-6361/201731866.

[28] Brynmor Haskell and Andrew Melatos. Models of pulsar glitches. *International Journal of Modern Physics D*, 24(3):1530008, January 2015. doi: 10.1142/S0218271815300086.

[29] James J. Condon and Scott M. Ransom. *Essential Radio Astronomy*. 2016.

[30] Spencer Beloin, Sophia Han, Andrew W. Steiner, and Dany Page. Constraining superfluidity in dense matter from the cooling of isolated neutron stars. *Physical Review C*, 97(1):015804, Jan 2018. doi: 10.1103/PhysRevC.97.015804.

[31] P. Haensel, A. Y. Potekhin, and D. G. Yakovlev. *Neutron Stars 1 : Equation of State and Structure*, volume 326. 2007.

[32] D. G. Yakovlev and C. J. Pethick. Neutron Star Cooling. *Annual Review of Astronomy & Astrophysics*, 42(1):169–210, Sep 2004. doi: 10.1146/annurev.astro.42.053102.134013.

[33] D. Kobyakov and C. J. Pethick. Towards a Metallurgy of Neutron Star Crusts. *Physical Review Letters*, 112(11):112504, Mar 2014. doi: 10.1103/PhysRevLett.112.112504.

[34] D. A. Baiko and A. I. Chugunov. Breaking properties of neutron star crust. *Monthly Notices of the Royal Astronomical Society*, 480(4):5511–5516, Nov 2018. doi: 10.1093/mnras/sty2259.

[35] O. Elgaroy, L. Engvik, M. Hjorth-Jensen, and E. Osnes. Triplet pairing of neutrons in β-stable neutron star matter. *Nuclear Physics A*, 607: 425–441, Feb 1996. doi: 10.1016/0375-9474(96)00217-5.

[36] G. E. Volovik. *Exotic Properties of Superfluid Helium 3*. 1992. doi: 10.1142/1439.

[37] J. M. C. Chen, J. W. Clark, R. D. Dave, and V. V. Khodel. Pairing gaps in nucleonic superfluids. *Nuclear Physics A*, 555(1):59–89, Apr 1993. doi: 10.1016/0375-9474(93)90314-N.

[38] M. Ali Alpar. Flux-Vortex Pinning and Neutron Star Evolution. *Journal of Astrophysics and Astronomy*, 38(3):44, September 2017. doi: 10.1007/s12036-017-9473-6.

[39] William G. Newton. Neutron stars: A taste of pasta? *Nature Physics*, 9(7):396–397, Jul 2013. doi: 10.1038/nphys2663.

[40] B. P. et al. The LIGO Scientific Collaboration Abbott and Virgo Collaboration. Gw170817: Observation of gravitational waves from a binary neutron star inspiral. *Phys. Rev. Lett.*, 119:161101, Oct 2017. doi: 10.1103/PhysRevLett.119.161101. URL `https://link.aps.org/doi/10.1103/PhysRevLett.119.161101`.

[41] Luca Baiotti. Gravitational waves from neutron star mergers and their relation to the nuclear equation of state. *Progress in Particle and Nuclear Physics*, 109:103714, Nov 2019. doi: 10.1016/j.ppnp.2019.103714.

[42] Paul D. Lasky. Gravitational Waves from Neutron Stars: A Review. *PASA*, 32:e034, September 2015. doi: 10.1017/pasa.2015.35.

[43] Nils Andersson. TOPICAL REVIEW: Gravitational waves from instabilities in relativistic stars. *Classical and Quantum Gravity*, 20(7): R105–R144, Apr 2003. doi: 10.1088/0264-9381/20/7/201.

[44] Lee Lindblom and Gregory Mendell. r-modes in superfluid neutron stars. *Physical Review D (Particles, Fields, Gravitation, and Cosmology)*, 61(10):104003, May 2000. doi: 10.1103/PhysRevD.61.104003.

[45] Michel Rieutord. Ekman Layers and the Damping of Inertial R-Modes in a Spherical Shell: Application to Neutron Stars. *The Astrophysical Journal*, 550(1):443–447, Mar 2001. doi: 10.1086/319705.

[46] Stuart L. Shapiro and Saul A. Teukolsky. *Black Holes, White Dwarfs and Neutron Stars: The Physics of Compact Objects*. 1986.

[47] Oliver Hamil. Braking index of isolated pulsars: open questions and ways forward. *arXiv e-prints*, art. arXiv:1503.09110, Mar 2015.

[48] Simon Johnston and David Galloway. Pulsar braking indices revisited. MNRAS, 306(4):L50–L54, July 1999. doi: 10.1046/j.1365-8711.1999.02737.x.

[49] C. M. Espinoza, A. G. Lyne, B. W. Stappers, and M. Kramer. A study of 315 glitches in the rotation of 102 pulsars. *Monthly Notices of the Royal Astronomical Society*, 414(2):1679–1704, Jun 2011. doi: 10.1111/j.1365-2966.2011.18503.x.

[50] R. N. Manchester. Pulsar timing and its applications. In *Journal of Physics Conference Series*, volume 932 of *Journal of Physics Conference Series*, page 012002, Dec 2017. doi: 10.1088/1742-6596/932/1/012002.

[51] R. N. Manchester. 50 Years of Pulsars! In *Journal of Physics Conference Series*, volume 932 of *Journal of Physics Conference Series*, page 012001, Dec 2017. doi: 10.1088/1742-6596/932/1/012001.

[52] Duncan R. Lorimer. Binary and Millisecond Pulsars. *Living Reviews in Relativity*, 11(1):8, November 2008. doi: 10.12942/lrr-2008-8.

[53] R. N. Manchester, G. B. Hobbs, A. Teoh, and M. Hobbs. The Australia Telescope National Facility Pulsar Catalogue. *The Astronomical Journal*, 129(4):1993–2006, Apr 2005. doi: 10.1086/428488.

[54] F. E. Marshall, E. V. Gotthelf, J. Middleditch, Q. D. Wang, and W. Zhang. The Big Glitcher: The Rotation History of PSR J0537-6910. *The Astrophysical Journal*, 603(2):682–689, Mar 2004. doi: 10.1086/381567.

[55] Rim Dib and Victoria M. Kaspi. 16 yr of RXTE Monitoring of Five Anomalous X-Ray Pulsars. *The Astrophysical Journal*, 784(1):37, Mar 2014. doi: 10.1088/0004-637X/784/1/37.

[56] Paul S. Ray, Sebastien Guillot, Wynn C. G. Ho, Matthew Kerr, Teruaki Enoto, Keith C. Gendreau, Zaven Arzoumanian, Diego Altamirano, Slavko Bogdanov, Robert Campion, Deepto Chakrabarty, Julia S. Deneva, Gaurava K. Jaisawal, Robert Kozon, Christian Malacaria, Tod E. Strohmayer, and Michael T. Wolff. Anti-glitches in the Ultraluminous Accreting Pulsar NGC 300 ULX-1 Observed with NICER. *The Astrophysical Journal*, 879(2):130, Jul 2019. doi: 10.3847/1538-4357/ab24d8.

[57] R N Manchester. Pulsar glitches and their impact on neutron-star astrophysics. *arXiv e-prints*, art. arXiv:1801.04332, Jan 2018.

[58] B. Haskell and D. Antonopoulou. Glitch recoveries in radio-pulsars and magnetars. *Monthly Notices of the Royal Astronomical Society*, 438(1):L16–L20, Feb 2014. doi: 10.1093/mnrasl/slt146.

[59] Gregory Ashton, Paul D. Lasky, Vanessa Graber, and Jim Palfreyman. Rotational evolution of the Vela pulsar during the 2016 glitch. *Nature Astronomy*, page 417, Aug 2019. doi: 10.1038/s41550-019-0844-6.

[60] A. Montoli, M. Antonelli, F. Magistrelli, and P. M. Pizzochero. Bayesian estimate of the superfluid moments of inertia from the 2016 glitch in the Vela pulsar. A&A, 642:A223, October 2020. doi: 10.1051/0004-6361/202038340.

[61] B Shaw, A G Lyne, B W Stappers, P Weltevrede, C G Bassa, A Y Lien, M B Mickaliger, R P Breton, C A Jordan, M J Keith, and H A Krimm. The largest glitch observed in the Crab pulsar. *Monthly Notices of the Royal Astronomical Society*, 478(3):3832–3840, 05 2018. ISSN 0035-8711. doi: 10.1093/mnras/sty1294. URL `https://doi.org/10.1093/mnras/sty1294`.

[62] J. R. Fuentes, C. M. Espinoza, A. Reisenegger, B. Shaw, B. W. Stappers, and A. G. Lyne. The glitch activity of neutron stars. *Astronomy and Astrophysics*, 608:A131, December 2017. doi: 10.1051/0004-6361/201731519.

[63] V. Khomenko and B. Haskell. Modelling Pulsar Glitches: The Hydrodynamics of Superfluid Vortex Avalanches in Neutron Stars. PASA, 35:e020, May 2018. doi: 10.1017/pasa.2018.12.

[64] B. Haskell, V. Khomenko, M. Antonelli, and D. Antonopoulou. Crust or core? Insights from the slow rise of large glitches in the Crab pulsar. MNRAS, 481(1):L146–L150, November 2018. doi: 10.1093/mnrasl/sly175.

[65] T. Celora, V. Khomenko, M. Antonelli, and B. Haskell. The effect of non-linear mutual friction on pulsar glitch sizes and rise times. MNRAS, 496(4):5564–5574, August 2020. doi: 10.1093/mnras/staa1930.

[66] P. M. Pizzochero, M. Antonelli, B. Haskell, and S. Seveso. Constraints on pulsar masses from the maximum observed glitch. *Nature Astronomy*, 1:0134, Jul 2017. doi: 10.1038/s41550-017-0134.

[67] W. G. Newton, S. Berger, and B. Haskell. Observational constraints on neutron star crust-core coupling during glitches. *Monthly Notices of the Royal Astronomical Society*, 454(4):4400–4410, Dec 2015. doi: 10.1093/mnras/stv2285.

[68] Brynmor Haskell. Probing neutron star interiors with pulsar glitches. In P. Weltevrede, B. B. P. Perera, L. L. Preston, and S. Sanidas, editors, *Pulsar Astrophysics the Next Fifty Years*, volume 337 of *IAU Symposium*, pages 203–208, Aug 2018. doi: 10.1017/S1743921317010663.

[69] B. Link. Incompatibility of long-period neutron star precession with creeping neutron vortices. *Astronomy and Astrophysics*, 458(3):881–884, Nov 2006. doi: 10.1051/0004-6361:20065664.

[70] V. Khomenko, M. Antonelli, and B. Haskell. Hydrodynamical instabilities in the superfluid interior of neutron stars with background flows between the components. Phys. Rev. D, 100(12):123002, December 2019. doi: 10.1103/PhysRevD.100.123002.

[71] B. Haskell, P. M. Pizzochero, and S. Seveso. Investigating Superconductivity in Neutron Star Interiors with Glitch Models. *The Astrophysical Journal Letters*, 764(2):L25, Feb 2013. doi: 10.1088/2041-8205/764/2/L25.

[72] Vanessa Graber, Andrew Cumming, and Nils Andersson. Glitch Rises as a Test for Rapid Superfluid Coupling in Neutron Stars. *The Astrophysical Journal*, 865(1):23, Sep 2018. doi: 10.3847/1538-4357/aad776.

[73] Sushan Konar and Mihir Arjunwadkar. Glitch statistics of radio pulsars: Multiple populations. In *Astronomical Society of India Conference Series*, volume 13 of *Astronomical Society of India Conference Series*, pages 87–88, Jan 2014.

[74] A. Parthasarathy, R. M. Shannon, S. Johnston, L. Lentati, M. Bailes, S. Dai, M. Kerr, R. N. Manchester, S. Oslowski, C. Sobey, W. van Straten, and P. Weltevrede. Timing of young radio pulsars - I. Timing noise, periodic modulation, and proper motion. *Monthly Notices of the Royal Astronomical Society*, 489(3):3810–3826, Nov 2019. doi: 10.1093/mnras/stz2383.

[75] J. M. Cordes and G. Greenstein. Pulsar timing .IV. Physical models for timing noise processes. *The Astrophysical Journal*, 245:1060–1079, May 1981. doi: 10.1086/158883.

[76] Andrew Melatos and Bennett Link. Pulsar timing noise from superfluid turbulence. *Monthly Notices of the Royal Astronomical Society*, 437(1):21–31, Jan 2014. doi: 10.1093/mnras/stt1828.

[77] L. D. Landau and E. M. Lifshitz. *Statistical physics. Pt.1, Pt.2.* 1980.

[78] Sébastien Balibar. The Discovery of Superfluidity. *Journal of Low Temperature Physics*, 146(5-6):441–470, March 2007. doi: 10.1007/s10909-006-9276-7.

[79] L. Landau. Theory of the Superfluidity of Helium II. *Physical Review*, 60(4):356–358, August 1941. doi: 10.1103/PhysRev.60.356.

[80] A.B Migdal. Superfluidity and the moments of inertia of nuclei. *Soviet Physics JETP*, 10:176, 1960.

[81] Serena Cenatiempo. Bogoliubov theory for dilute Bose gases: The Gross-Pitaevskii regime. *Journal of Mathematical Physics*, 60(8): 081901, Aug 2019. doi: 10.1063/1.5096288.

[82] Lev Davidovich Landau and E. M. Lifshitz. *Fluid mechanics*. 1959.

[83] L. D. Landau and E. M. Lifshitz. *Statistical physics. Pt.1, Pt.2*. 1980.

[84] Isaac M Khalatnikov and I M Khalatnikov. *An introduction to the theory of superfluidity*. Frontiers in physics. Benjamin, New York, NY, 1965. URL `https://cds.cern.ch/record/106134`. Trans. from the Russian.

[85] N. Andersson and G. L. Comer. A flux-conservative formalism for convective and dissipative multi-fluid systems, with application to Newtonian superfluid neutron stars. *Classical and Quantum Gravity*, 23 (18):5505–5529, Sep 2006. doi: 10.1088/0264-9381/23/18/003.

[86] B. Haskell, N. Andersson, and G. L. Comer. Dynamics of dissipative multifluid neutron star cores. Phys. Rev. D, 86(6):063002, September 2012. doi: 10.1103/PhysRevD.86.063002.

[87] Nicolas Chamel and Pawel Haensel. Entrainment parameters in a cold superfluid neutron star core. *Physical Review C*, 73(4):045802, Apr 2006. doi: 10.1103/PhysRevC.73.045802.

[88] N. Chamel, J. Pearson, and S. Goriely. *Superfluidity and Entrainment in Neutron-star Crusts*, volume 466 of *Astronomical Society of the Pacific Conference Series*, page 203. 2012.

[89] Gregory Mendell. Superfluid Hydrodynamics in Rotating Neutron Stars. I. Nondissipative Equations. *Astrophysical Journal*, 380:515, October 1991. doi: 10.1086/170609.

[90] Reinhard Prix. Variational description of multifluid hydrodynamics: Uncharged fluids. *Physical Review D*, 69(4):043001, February 2004. doi: 10.1103/PhysRevD.69.043001.

[91] N. Chamel. Entrainment in Superfluid Neutron-Star Crusts: Hydrodynamic Description and Microscopic Origin. *Journal of Low Temperature Physics*, 189(5-6):328–360, December 2017. doi: 10.1007/s10909-017-1815-x.

[92] P. B. Jones. Rotation of the neutron-drip superfluid in pulsars : the resistive force. *MNRAS*, 243:257–262, March 1990.

[93] M. A. Alpar, S. A. Langer, and J. A. Sauls. Rapid postglitch spin-up of the superfluid core in pulsars. *Astrophysical Journal*, 282:533–541, July 1984. doi: 10.1086/162232.

[94] Richard I. Epstein and Gordon Baym. Vortex Drag and the Spin-up Time Scale for Pulsar Glitches. *Astrophysical Journal*, 387:276, March 1992. doi: 10.1086/171079.

[95] W. F. Vinen. Mutual Friction in a Heat Current in Liquid Helium II. III. Theory of the Mutual Friction. *Proceedings of the Royal Society of London Series A*, 242(1231):493–515, November 1957. doi: 10.1098/rspa.1957.0191.

[96] B. Haskell, D. Antonopoulou, and C. Barenghi. Turbulent, pinned superfluids in neutron stars and pulsar glitch recoveries. MNRAS, 499 (1):161–170, November 2020. doi: 10.1093/mnras/staa2678.

[97] C. Peralta, A. Melatos, M. Giacobello, and A. Ooi. Transitions between Turbulent and Laminar Superfluid Vorticity States in the Outer Core of a Neutron Star. ApJ, 651(2):1079–1091, November 2006. doi: 10.1086/507576.

[98] N. Andersson, T. Sidery, and G. L. Comer. Superfluid neutron star turbulence. MNRAS, 381(2):747–756, October 2007. doi: 10.1111/j.1365-2966.2007.12251.x.

[99] N. Chamel. Superfluidity and Superconductivity in Neutron Stars. *Journal of Astrophysics and Astronomy*, 38(3):43, Sep 2017. doi: 10.1007/s12036-017-9470-9.

[100] M. Ruderman. Neutron Starquakes and Pulsar Periods. *Nature*, 223 (5206):597–598, August 1969. doi: 10.1038/223597b0.

[101] Bennett Link and Richard I. Epstein. Thermally Driven Neutron Star Glitches. *Astrophysical Journal*, 457:844, February 1996. doi: 10.1086/176779.

[102] N. Andersson, G. L. Comer, and R. Prix. The superfluid two-stream instability and pulsar glitches. *arXiv e-prints*, art. astro-ph/0211151, November 2002.

[103] L. Warszawski, A. Melatos, and N. G. Berloff. Unpinning triggers for superfluid vortex avalanches. *Physical Review B*, 85(10):104503, Mar 2012. doi: 10.1103/PhysRevB.85.104503.

[104] Kostas Glampedakis and Nils Andersson. Hydrodynamical Trigger Mechanism for Pulsar Glitches. *Physical Review Letters*, 102(14): 141101, Apr 2009. doi: 10.1103/PhysRevLett.102.141101.

[105] S. Seveso, P. M. Pizzochero, F. Grill, and B. Haskell. Mesoscopic pinning forces in neutron star crusts. MNRAS, 455(4):3952–3967, February 2016. doi: 10.1093/mnras/stv2579.

[106] Gabriel Wlazłowski, Kazuyuki Sekizawa, Piotr Magierski, Aurel Bulgac, and Michael McNeil Forbes. Vortex Pinning and Dynamics in the Neutron Star Crust. Phys. Rev. Lett., 117(23):232701, December 2016. doi: 10.1103/PhysRevLett.117.232701.

[107] W. Fulgenzi, A. Melatos, and B. D. Hughes. Radio pulsar glitches as a state-dependent Poisson process. *MNRAS*, 470(4):4307–4329, October 2017. doi: 10.1093/mnras/stx1353.

[108] B. Haskell and D. Antonopoulou. Glitch recoveries in radio-pulsars and magnetars. *Monthly Notices of the Royal Astronomical Society*, 438(1):L16–L20, Feb 2014. doi: 10.1093/mnrasl/slt146.

[109] N. Andersson, K. Glampedakis, W. C. G. Ho, and C. M. Espinoza. Pulsar Glitches: The Crust is not Enough. *Physical Review Letters*, 109(24):241103, Dec 2012. doi: 10.1103/PhysRevLett.109.241103.

[110] T. Sidery and M. A. Alpar. The effect of quantized magnetic flux lines on the dynamics of superfluid neutron star cores. *Monthly Notices of the Royal Astronomical Society*, 400(4):1859–1867, Dec 2009. doi: 10.1111/j.1365-2966.2009.15575.x.

[111] Malvin Ruderman, Tianhua Zhu, and Kaiyou Chen. Neutron Star Magnetic Field Evolution, Crust Movement, and Glitches. *The Astrophysical Journal*, 492(1):267–280, Jan 1998. doi: 10.1086/305026.

[112] Armen Sedrakian and James M. Cordes. Vortex-interface interactions and generation of glitches in pulsars. *MNRAS*, 307(2):365–375, August 1999. doi: 10.1046/j.1365-8711.1999.02638.x.

[113] A. Melatos and L. Warszawski. Superfluid Vortex Unpinning as a Coherent Noise Process, and the Scale Invariance of Pulsar Glitches. *The Astrophysical Journal*, 700(2):1524–1540, Aug 2009. doi: 10.1088/0004-637X/700/2/1524.

[114] B. Haskell and A. Melatos. Pinned vortex hopping in a neutron star crust. *Monthly Notices of the Royal Astronomical Society*, 461(2): 2200–2211, Sep 2016. doi: 10.1093/mnras/stw1334.

[115] M. A. Alpar, D. Pines, P. W. Anderson, and J. Shaham. Vortex creep and the internal temperature of neutron stars. I - General theory. ApJ, 276:325–334, January 1984. doi: 10.1086/161616.

[116] L. Warszawski and A. Melatos. Knock-on processes in superfluid vortex avalanches and pulsar glitch statistics. *Monthly Notices of the Royal Astronomical Society*, 428(3):1911–1926, Jan 2013. doi: 10.1093/mnras/sts108.

[117] A. Melatos and L. Warszawski. Superfluid Vortex Unpinning as a Coherent Noise Process, and the Scale Invariance of Pulsar Glitches. ApJ, 700(2):1524–1540, August 2009. doi: 10.1088/0004-637X/700/2/1524.

[118] A. Melatos, C. Peralta, and J. S. B. Wyithe. Avalanche Dynamics of Radio Pulsar Glitches. *The Astrophysical Journal*, 672(2):1103–1118, Jan 2008. doi: 10.1086/523349.

[119] B. Haskell. The effect of superfluid hydrodynamics on pulsar glitch sizes and waiting times. *Monthly Notices of the Royal Astronomical Society*, 461(1):L77–L81, Sep 2016. doi: 10.1093/mnrasl/slw103.

[120] A. Melatos, C. Peralta, and J. S. B. Wyithe. Avalanche Dynamics of Radio Pulsar Glitches. ApJ, 672(2):1103–1118, January 2008. doi: 10.1086/523349.

[121] G. Howitt, A. Melatos, and A. Delaigle. Nonparametric Estimation of the Size and Waiting Time Distributions of Pulsar Glitches. ApJ, 867 (1):60, November 2018. doi: 10.3847/1538-4357/aae20a.

[122] B. Haskell, P. M. Pizzochero, and T. Sidery. Modelling pulsar glitches with realistic pinning forces: a hydrodynamical approach. *Monthly Notices of the Royal Astronomical Society*, 420(1):658–671, Feb 2012. doi: 10.1111/j.1365-2966.2011.20080.x.

[123] M. Antonelli and P. M. Pizzochero. Axially symmetric equations for differential pulsar rotation with superfluid entrainment. *Monthly Notices of the Royal Astronomical Society*, 464(1):721–733, Jan 2017. doi: 10.1093/mnras/stw2376.

Publications of the Astronomical Society of Australia (PASA), Vol. 35, e020, 15 pages (2018).

doi:10.1017/pasa.2018.12

Modelling Pulsar Glitches: The Hydrodynamics of Superfluid Vortex Avalanches in Neutron Stars

V. Khomenko and B. Haskell[1]

Nicolaus Copernicus Astronomical Center, Polish Academy of Sciences, ul. Bartycka 18, 00-716 Warsaw, Poland
[1]Email: bhaskell@camk.edu.pl

(Received January 5, 2018; Accepted March 22, 2018)

Abstract

The dynamics of quantised vorticity in neutron star interiors is at the heart of most pulsar glitch models. However, the large number of vortices (up to $\approx 10^{13}$) involved in a glitch and the huge disparity in scales between the femtometre scale of vortex cores and the kilometre scale of the star makes quantum dynamical simulations of the problem computationally intractable. In this paper, we take a first step towards developing a mean field prescription to include the dynamics of vortices in large-scale hydrodynamical simulations of superfluid neutron stars. We consider a one-dimensional setup and show that vortex accumulation and differential rotation in the neutron superfluid lead to propagating waves, or 'avalanches', as solutions for the equations of motion for the superfluid velocities. We introduce an additional variable, the fraction of free vortices, and test different prescriptions for its advection with the superfluid flow. We find that the new terms lead to solutions with a linear component in the rise of a glitch, and that, in specific setups, they can give rise to glitch precursors and even to decreases in frequency, or 'anti-glitches'.

Keywords: hydrodynamics – pulsars: general – stars: neutron

1 INTRODUCTION

Pulsar glitches are sudden increases in the rotational frequency of pulsars (predominantly observed in radio, but also seen in X-rays and gamma-rays), that are instantaneous to the accuracy of the data [with the best upper limits constraining the rise time to be less than approximately 1 min (Dodson, McCulloch, & Lewis 2002)] and are thought to be due to the presence of a large-scale superfluid component in the neutron star. Mature neutron stars are, in fact, cold enough for neutrons to be superfluid and protons superconducting (Migdal 1959; Baym, Pethick, & Pines 1969) [see Haskell & Sedrakian (2017) for a recent review]. Superfluidity has a strong impact on the dynamics of the stellar interior, as a superfluid rotates by forming an array of quantised vortices which carry the circulation and mediate angular momentum exchange between the superfluid neutrons and the normal component of the star, which is tracked by the electromagnetic emission.

If vortices are strongly attracted, or 'pinned' to ions in the crust or flux tubes in the core of the star they cannot move out, and the superfluid cannot spin-down with the normal component, thus storing angular momentum. Sudden recoupling of the components leads to rapid angular momentum exchange and a glitch (Anderson & Itoh 1975). Realistic models of pinning forces (Seveso et al. 2016; Wlazłowski et al. 2016) and effective masses (Chamel 2012, 2017; Watanabe & Pethick 2017) in the neutron star crusts can be used to calculate the amount of angular momentum transferred during a glitch (Pizzochero 2011; Haskell, Pizzochero, & Sidery 2012; Seveso, Pizzochero, & Haskell 2012; Andersson et al. 2012; Chamel 2013) and compared to observations to constrain the mass of a glitching pulsar and its equation of state (Newton, Berger, & Haskell 2015; Ho et al. 2015; Pizzochero et al. 2017). Nevertheless, the trigger mechanism for glitches is still unknown [see Haskell & Melatos (2015) for a recent review]. The main mechanisms that have been proposed are crust quakes (Ruderman 1969), hydrodynamical instabilities (Mastrano & Melatos 2005; Glampedakis & Andersson 2009), and vortex avalanches (Cheng et al. 1988; Warszawski & Melatos 2013).

In this paper, we will focus on this last mechanism, vortex avalanches. In this model, local, fast, interactions between neighbouring vortices release stresses built up gradually over time as the star spins down. This is the hall mark of Self Organised Criticality (SOC), and in fact quantum mechanical simulations of vortices in a spinning-down trap confirm that the spin-down of the superfluid occurs via discrete vortex avalanches, and that the distribution of glitch sizes is a

power-law, and the distribution of waiting times an exponential (Warszawski & Melatos 2011). This is consistent with the size and waiting time distributions of most pulsars, except for Vela and J0537-6910 (Melatos, Peralta, & Wyithe 2008), for which an excess of large avalanches appears, with a preferred size and waiting time. Furthermore, in J0537-6910, there is a correlation between waiting times and the size of the previous glitch (Middleditch et al. 2006; Antonopoulou et al. 2018), which some have suggested may be due to crust quakes (Middleditch et al. 2006), but may also be the consequence of rapid driving preventing the system from self-organising, and leading to the whole pinned vorticity being expelled once the maximum of the pinning force is reached, as is the case in the 'snowplow' model for giant glitches (Pizzochero 2011). An excess of large avalanches may also indicate a departure of the system from SOC behaviour, and the onset of a self-organised bistable state (di Santo et al. 2016).

Quantum mechanical simulations, however, suffer from numerical limitations that do not allow to simulate the full neutron star system, or to model the difference in scales in a neutron star, where vortices with a coherence length $\xi_c \approx 10$ fm are separated by a distance $d_{\rm v} \approx 10^{-3}$ cm. Recent work has, however, shown that even in a realistic neutron star, vortices can always move, on average, far enough to knock on neighbouring vortices without repinning, provided the relative velocity between the normal fluid and the superfluid W is close to critical velocity for unpinning, $W_{\rm cr}$, and in particular, $W \gtrsim 0.95\ W_{\rm cr}$ for standard superfluid drag parameters (Haskell & Melatos 2016).

In this paper, we take a first step towards including the microphysics of vortex avalanches in larger scale hydrodynamical simulations. The situation is complex, as for a hydrodynamical treatment, one has to average over several vortices to define a coarse-grained momentum for the superfluid condensate, thus losing information on the dynamics of individual vortex unpinning and knock-on events. Large-scale hydrodynamical coupling, however, can have a strong impact on the dynamics of the system, and it is well known since the pioneering work on vortex creep of Alpar et al. (1984a) that thermal unpinning of vortices can lead to non-linear terms in the hydrodynamical equations of motion for the superfluid velocities, and affect the post-glitch relaxation (Akbal et al. 2017).

Recently, Haskell (2016) showed that random unpinning events, drawn from microphysically motivated power-law distributions, can be included in simulations. The resulting glitch distribution, however, differs from the original distribution of vortex unpinning events, and has a cut-off at small sizes, which can explain the observed deviation from a power-law of the distribution of glitches in the Crab pulsar for small sizes (Espinoza et al. 2014). Furthermore, such an approach can also explain the different kinds of relaxation observed after glitches, also in the same star (Haskell & Antonopoulou 2014). Here we will follow this approach, but take a step forward in modelling the non-linear propagation of a vortex unpinning front during an avalanche.

2 SUPERFLUID HYDRODYNAMICS

We take as our starting point a hydrodynamical description of the superfluid interior of the star, in which we do not deal with the dynamics of individual vortices directly, but rather deal with averaged large-scale degrees of freedom that describe superfluid neutron velocities and densities, and those of a charge neutral fluid of protons and electrons. For the purpose of investigating the timescales associated with glitches, we will consider protons and electrons to be locked by electromagnetic interactions and flow as a single fluid (Mendell 1991). Following Andersson & Comer (2006), we can write conservation laws for each species:

$$\partial_t \rho_{\rm x} + \nabla_i(\rho_{\rm x} v^i_{\rm x}) = 0, \tag{1}$$

where the constituent index x labels either protons (p) or neutrons (n), $v^i_{\rm x}$ is the velocity, and $\rho_{\rm x}$ is a density of respective constituent x. Note also that summation over repeated indices is implied (with the exclusion of constituent indices). The Euler equations are

$$\begin{aligned}(\partial_t + v^j_{\rm x}\nabla_j)(v^{\rm x}_i + \varepsilon_{\rm x} w^{\rm yx}_i) + \nabla_i(\tilde{\mu}_{\rm x} + \Phi)^j \\ +\varepsilon_{\rm x} w^j_{\rm yx}\nabla_i v^{\rm x}_j = (f^{\rm x}_i + f^{\rm xp}_i)/\rho_{\rm x},\end{aligned} \tag{2}$$

where $w^{\rm yx}_i = v^{\rm y}_i - v^{\rm x}_i$ and $\tilde{\mu}_{\rm x} = \mu_{\rm x}/m_{\rm x}$ are the chemical potential per unit mass (in the following, we take $m_{\rm p} = m_{\rm n}$). The gravitational potential is Φ and $\varepsilon_{\rm x}$ is the entrainment coefficient which can account for the reduced mobility of neutrons, especially in the crust (Prix 2004; Chamel 2017). The terms on the right-hand side are the contribution to the vortex-mediated mutual friction due to pinned vortices $f^{\rm px}_i$ and to free vortices, $f^{\rm x}_i$, which, for straight vortices and laminar flows, takes the form

$$f^{\rm x}_i = \kappa n_{\rm v}\rho_{\rm n}\mathcal{B}'\epsilon_{ijk}\hat{\Omega}^i_{\rm n} w^k_{\rm xy} + \kappa n_{\rm v}\rho_{\rm n}\mathcal{B}\epsilon_{ijk}\hat{\Omega}^j_{\rm n}\epsilon^{klm}\hat{\Omega}^{\rm n}_l w^{\rm xy}_m, \tag{3}$$

where $\Omega^j_{\rm n}$ is the angular velocity of the neutrons (a hat represents a unit vector), $\kappa = h/2m_{\rm n}$ is the quantum of circulation, $n_{\rm v}$ is the vortex density per unit area, and ε_{ijk} is the Levi Civita symbol. Finally, the Feynman relations link vortex density at a cylindrical radius ϖ to the rotation rate of a superfluid element:

$$\kappa n_{\rm v}(\varpi) = 2\tilde{\Omega}_{\rm n} + \varpi\frac{\partial\tilde{\Omega}_{\rm n}}{\partial\varpi}, \tag{4}$$

with

$$\tilde{\Omega}_{\rm n} = \left[\Omega_{\rm n} + \varepsilon_{\rm n}(\Omega_{\rm p} - \Omega_{\rm n})\right]. \tag{5}$$

The parameters $\mathcal{B}$ and $\mathcal{B}'$ in the expression for the mutual friction in (3) can be expressed in terms of a dimensionless drag parameter $\mathcal{R}$, related to the standard drag parameter γ_d as

$$\mathcal{R} = \frac{\gamma_{\rm d}}{\kappa\rho_{\rm n}}, \tag{6}$$

and are defined as

$$\mathcal{B} = \frac{\mathcal{R}}{1+\mathcal{R}^2} \quad \text{and} \quad \mathcal{B}' = \frac{\mathcal{R}^2}{1+\mathcal{R}^2}. \tag{7}$$

The parameter $\mathcal{R}$ encodes the microphysics of the dissipation processes that take place in the stellar interior, and its value is highly uncertain. Nevertheless, the exact value of $\mathcal{R}$ is not crucial for the following discussion, and we will in general assume that $\mathcal{R} \ll 1$, and indicate the values we use explicitly in the examples provided.

Following Sidery, Passamonti, & Andersson (2010), we can simplify the problem by considering the evolution of the angular velocity of two axially symmetric rotating components. The evolution equations for the angular velocities thus take the form

$$\dot{\Omega}_{\rm n}(\varpi) = \frac{\mathcal{Q}(\varpi)}{\rho_{\rm n}} \frac{1}{1-\varepsilon_{\rm n}-\varepsilon_{\rm p}} + \frac{\varepsilon_{\rm n}}{(1-\varepsilon_{\rm n})}\dot{\Omega}_{\rm ext} + F_{\rm p}(\varpi), \quad (8)$$

$$\dot{\Omega}_{\rm p}(\varpi) = -\frac{\mathcal{Q}(\varpi)}{\rho_{\rm p}} \frac{1}{1-\varepsilon_{\rm n}-\varepsilon_{\rm p}} - \dot{\Omega}_{\rm ext} - \frac{\rho_{\rm n}}{\rho_{\rm p}} F_{\rm p}(\varpi), \quad (9)$$

where

$$\mathcal{Q}(\varpi) = \rho_{\rm n}\gamma\kappa n_{\rm v}\mathcal{B}(\Omega_{\rm p}-\Omega_{\rm n}), \quad (10)$$

and $\gamma = {\rm n}_f/n_{\rm v}$ is the fraction of vortices which are not pinned (with n_f the surface density of free vortices), while $\dot{\Omega}_{\rm ext}$ is the contribution from the external spin-down torque. $F_{\rm p}$ is the contribution from the pinning force. While recent progress has been made on determining the maximum value of the pinning force from microphysical calculations (Seveso et al. 2016; Wlazłowski et al. 2016), its exact form is not known. This does not, however, hinder our discussion, for which the exact form for $F_{\rm p}$ is not necessary. It will be sufficient to assume that $F_{\rm p}$ balances the contribution to the mutual friction from the $(1-\gamma)n_{\rm v}$ pinned vortices, below a critical threshold for the lag $\Delta\Omega_{\rm C}$. Above $\Delta\Omega_{\rm C}$, all vortices are free and $F_{\rm p} = 0$ [see, e.g., Seveso et al. (2016) for realistic estimates of the maximum lag the pinning force can sustain]. In the following, we will thus not explicitly consider the pinning force, but simply assume a value of the critical lag $\Delta\Omega_{\rm C}$.

We can further simplify the problem by assuming, as in Haskell et al. (2012) and Haskell (2016), that the proton component, consisting of the elastic crust and tightly coupled protons and electrons in the core, is rigidly rotating. This is likely to be a good approximation on timescales longer than the elastic and Alfven timescales in the crust, and simplifies our problem considerably [although see van Eysden (2014) for a discussion of the short-timescale dynamics that is neglected with this approximation]. In this approximation, the equation of motion for the protons can be obtained from (9) and is the following:

$$\dot{\Omega}_{\rm p} = -\dot{\Omega}_{\infty} - \int \frac{\varpi^2}{I_{\rm p}}\left[\frac{\mathcal{Q}(\varpi)}{1-\varepsilon_{\rm n}-\varepsilon_{\rm p}} + \rho_{\rm n}F_{\rm p}(\varpi)\right] {\rm d}V, \quad (11)$$

where $I_{\rm p}$ is the moment of inertia of the charged component.

Note that the above equations assume that vortices are straight and the rotation profile of the neutron fluid is axisymmetric. This may not be the case in the presence of strong density-dependent entrainment, as is expected in the crust (Chamel 2012). Antonelli & Pizzochero (2017) have analysed this problem and proposed a formalism that allows one to treat the problem as axially symmetric. Given that the equations are formally equivalent, and we do not consider a density-dependent entrainment profile, we will ignore this complication in the following and continue working with the above set of equations which allow for a more transparent interpretation of the results.

It is also expected that turbulence may develop in neutron star interiors, leading to a turbulent polarised tangle of vortices and additional non-linear terms in the mutual friction force (Andersson, Sidery, & Comer 2007). The importance of turbulence can be assessed by examining the evolution equation for the vorticity:

$$\frac{\partial \xi_{\rm n}^k}{\partial t} = (1-\mathcal{B}')\epsilon^{kim}\nabla_m(\epsilon_{ijl}v_{\rm n}^j\xi_{\rm n}^l) + \mathcal{B}\epsilon^{kim}\nabla_m(\xi_i^{\rm n}\hat{\xi}_j^{\rm n}v_{\rm n}^j - \hat{\xi}_j^{\rm n}\xi_{\rm n}^j v_{\rm n}^i)\,, \quad (12)$$

with $\xi_i^{\rm n} = \epsilon^{ijk}\nabla_j v_k^{\rm n}$, and where $\hat{\xi}_i$ is a unit vector along ξ_i.

The first term on the right-hand side represents transfer of energy to small length scales, while the second leads to damping that stabilises the flow. The relative importance of two effects is determined by a parameter:

$$q = \frac{\mathcal{B}}{1-\mathcal{B}'}. \quad (13)$$

It was shown by Finne et al. (2003) that turbulence sets in for $q \leqslant 1.3$. At high densities in the stellar interior $\mathcal{B}' \approx \mathcal{B}^2 \ll 1$ so that $q \ll 1$ and a superfluid neutron core is expected to be extremely susceptible to becoming turbulent, while the importance of turbulence in the crustal region is more uncertain, given the large uncertainties on $\mathcal{B}$ and $\mathcal{B}'$. To take into account the influence of turbulence and vortex curvature on the mutual friction force, one may rewrite

$$f_i^{mf} = \rho_{\rm n}L_R(\mathcal{B}'\epsilon_{ijk}k^j w_{\rm np}{}^k + \mathcal{B}\epsilon_{ijk}\epsilon^{klm}\hat{\kappa}^j\kappa_l w_m^{\rm np} - \tilde{\nu}[\mathcal{B}'\hat{\kappa}^j\nabla_j\kappa_i + \mathcal{B}\epsilon_{ijk}\kappa^j\hat{\kappa}^l]\nabla_l\hat{\kappa}^k) + \frac{2L_T}{3}\rho_{\rm n}k\mathcal{B}w_i^{\rm pn}, \quad (14)$$

where the last term represents polarised turbulence while the third and fourth describe the influence of an isotropic turbulent tangle. Here,

$$\tilde{\nu} = \frac{1}{1-\varepsilon_{\rm n}-\varepsilon_{\rm p}}\nu\,, \quad (15)$$

with L_R is the vortex length due to the rotation, such that $|\nabla\times\vec{v}_{\rm n}| = 2\Omega = L_R\kappa$, and $L_T = L - L_R$, with L the total length of vortex. The vector κ^i defines the orientation of vortex and ν is a parameter that determines the tension of the vortex [see Andersson et al. (2007) for a detailed description of the problem].

For polarised turbulence, the straight vortex term thus leads to the shortest timescales. In our work, we study the short-timescale dynamics of avalanches and ignore longer post-glitch timescale, for which additional physics regarding coupling timescales at different densities would, anyway, have to be included [see, e.g., Haskell et al. (2012) and Newton et al. (2015)]. Hence, turbulence is unlikely to make a qualitative

difference to our results, and for computational simplicity, we ignore it in the following.

3 VORTEX PINNING AND UNPINNING

To solve the system of equations in the previous section, we still require inputs from microphysics. Apart from the fraction of neutrons, the mutual friction parameters $\mathcal{B}$ are required. In the outer core of the neutron star, the main contribution to mutual friction is expected to come from electrons scattering on vortex cores, which leads to $\mathcal{B} \approx 10^{-4}$ (Alpar, Langer, & Sauls 1984b; Andersson, Sidery, & Comer 2006). In the crust, the situation is much more uncertain, as phonon scattering will lead to weak damping, with mutual friction parameters as low as $\mathcal{B} \approx 10^{-10}$, but if vortices move rapidly past pinning sites, Kelvin waves may be excited leading to $\mathcal{B} \approx 10^{-2}$ (Jones 1990, 1992; Epstein & Baym 1992). Given this level of uncertainty, and the small scales we consider, we will take $\mathcal{B}$ as a constant, free parameter, and study how our results depend on it.

In our description, however, we have also introduced an extra parameter that rescales the mutual friction coefficients, i.e., the fraction of unpinned vortices γ. This will depend specifically on the dynamics of vortices on scales smaller than the hydrodynamical scale we are discussing.

Before moving on, let us thus address the validity of our hydrodynamical description. Hydrodynamics is the natural tool to model macroscopic, observable, phenomena in neutron stars, and the key assumption is that we can track the evolution of fluid elements as they evolve. A fluid element must be small enough to be considered as a 'point' in the macroscopical hydrodynamical description, but also large enough to contain enough particles to allow for meaningful averaged hydrodynamical quantities and fluxes to be defined.

This is particularly relevant for a superfluid, which is irrotational and rotates by forming an array of quantised vortices which carry the circulation. In practice, this means that a coarse-grained description must average over several vortices in order to define a superfluid velocity for a fluid element, leading to a large-scale neutron fluid which is not irrotational. The minimum scale on which it is meaningful to discuss hydrodynamics is thus given by the typical inter-vortex spacing, which is of the order of

$$d_{\rm v} = 1 \times 10^{-3} \left(\frac{P}{10\ {\rm ms}} \right)^{1/2} {\rm cm}, \tag{16}$$

where P is the spin period of the star. Note, however that dynamics on a smaller inter-vortex scale (on which neutrons behave as an irrotational fluid, defined by the neutron–neutron scattering length scale of approximately a micron), is crucial for determining mutual friction and pinning parameters.

Knock-on effects between vortices are likely to be fundamental for the dynamics we observe in pulsar glitches. Consider a simple model in which such effects are neglected, and one simply has random, uncorrelated, unpinning of individual vortices. In this case, the probability of unpinning n vortices during an observation time Δt, is simply a Poissonian (Warszawski & Melatos 2013):

$$p(n) = \exp(-\theta \Delta t) \frac{(\theta \Delta t)^n}{n!}\ , \tag{17}$$

where θ is the unpinning rate for a single vortex. The result in (17) tends to a Gaussian for large Δt, suggesting that the average number of free vortices, and thus the average glitch size, should also follow a Gaussian distribution. However, this conflicts with the data in all pulsars except for PSR J0537-6910 and the Vela pulsar (Melatos et al. 2008). The glitch size distribution in other pulsars is consistent with a power-law, with the waiting times being exponentially distributed, which is in agreement with the results obtained with small-scale quantum mechanical Gross Pitaevskii simulations of superfluid vortices in a spinning-down trap (Warszawski & Melatos 2011). It is clear that we need to understand how to scale up the dynamics observed in such simulations of $\approx 10^2 - 10^3$ vortices, to the larger scale corse-grained hydrodynamical description where individual vortices are not resolved.

On the one side, the kind of vortex avalanches that are observed in simulations over scales of hundreds or thousands of vortices can lead to vortex depletion and accumulation on small scales and create sharp gradients in hydrodynamical simulations. On the other hand, large-scale dynamics can induce differential rotation, and significantly increase the local density of vortices, leading to knock on effects and unpinning (Warszawski, Melatos, & Berloff 2012; Haskell & Melatos 2016). For example, if vortex avalanches are free to propagate outward from high density regions at the base of the crust, towards lower density regions in which the pinning force peaks, individual vortice will encounter stronger pinning forces than in the region where they are originally unpinned. This can lead to vortices accumulating close to the maximum of the pinning force. A similar situation may occur even if vortices creep out, but the rate is not fast enough to keep up with the external driver (the electromagnetic spin-down), leading to vortex accumulation (Warszawski & Melatos 2013). This would create a vortex 'sheet' such as that suggested by Pizzochero (2011), in which the vortex density is significantly higher than the steady-state density $n_{\rm v} = 2\Omega_{\rm n}/\kappa$. Such a vortex sheet will gradually shift out, until the maximum lag that the pinning force can sustain is exceeded, after which all vortices are free and will rapidly move out transferring angular momentum catastrophically and giving rise to a 'giant' glitch, such as those observed in the Vela pulsar.

4 VORTEX SHEET

Let us now discuss this scenario in more detail and study, from a hydrodynamical point of view, how an avalanche can lead to angular momentum exchange between the superfluid and the crust.

First of all, let us define the lag between the two components:

$$\Delta\Omega = \Omega_{\rm p} - \Omega_{\rm n}\ . \tag{18}$$

By combining equations (8) and (9), we can obtain the following evolution equation:

$$\frac{\partial \Delta\Omega}{\partial t} = -\kappa n_{\rm v} \frac{\gamma \mathcal{B}}{x_{\rm p}(1-\varepsilon_{\rm n}-\varepsilon_{\rm p})} \Delta\Omega \,, \tag{19}$$

where $x_{\rm p} = \rho_{\rm p}/\rho$ with $\rho = \rho_{\rm p} + \rho_{\rm n}$, and we have assumed that vortices are free ($F_{\rm p} = 0$). We ignore the external torque, as we will be studying dynamics on much shorter timescales than those on which the external spin-down is relevant.

In the standard case, one neglects differential rotation and assumes that $\kappa n_v \approx 2\Omega_{\rm n}$. Neglecting the small change in overall frequency, and taking $\Omega_{\rm n}$ and $\mathcal{B}$ to be a constant, the approximate solution for the lag between the two components $\Delta\Omega$, is a damped exponential of the form (Andersson et al. 2006):

$$\Delta\Omega \approx \Delta_0 \exp -(t/\tau) \,, \tag{20}$$

with Δ_0 a constant and

$$\tau = \frac{x_{\rm p}(1-\varepsilon_{\rm n}-\varepsilon_{\rm p})}{2\Omega_{\rm n}\gamma\mathcal{B}} \,, \tag{21}$$

with γ taken to be constant. This is the mutual friction timescale that is usually compared to exponentially relaxing components of the spin frequency observed after glitches.

We intend to investigate a different situation here. We continue to consider the γ =constant case, and follow Cheng et al. (1988), thus considering a vortex accumulation region in which a large number of vortices (compared to the steady-state number present in the region) has repinned, i.e., such that

$$\kappa n_v \approx \varpi \frac{\partial}{\partial \varpi}[\Omega_{\rm n} + \varepsilon_{\rm n}(\Omega_{\rm p} - \Omega_{\rm n})] \,, \tag{22}$$

where the steady-state contribution $\kappa n_{\rm v} \approx 2\Omega_{\rm n}$ is neglected and $\varpi = r\sin\theta$ is the cylindrical radius.

In this situation, it is likely that strong pinning will force vortices to repin immediately and they will not be able to adjust to the lattice-equilibrium position that would be needed for this large increase in density. By the time the approximation $\varpi\partial\Omega_{\rm n}\partial\varpi > 2\Omega_{\rm n}$ is satisfied, one has a change in vortex density of order unity, corresponding to a similar change in vortex spacing $l_v \approx \sqrt{n_v}$. This leads to a large change in Magnus force as vortices get closer to each other, and the vortex sheet is thus very likely to unpin (Warszawski & Melatos 2013; Haskell 2016).

In the presence of significant differential rotation, the equation of motion for the lag $\Delta\Omega$ takes the following form:

$$\frac{\partial \Delta\Omega(\varpi,t)}{\partial t} = \varpi \frac{\gamma\mathcal{B}(1-\varepsilon_{\rm n})}{x_{\rm p}(1-\varepsilon_{\rm n}-\varepsilon_{\rm p})} \Delta\Omega(\varpi,t) \frac{\partial \Delta\Omega(\varpi,t)}{\partial \varpi} \,, \tag{23}$$

where we have assumed that, at least locally, the proton fluid (possibly the crust in this case) is rigidly rotating so that $\partial_\varpi \Omega_{\rm p} = 0$ and thus $\partial_\varpi \Delta\Omega = -\partial\varpi\Omega_{\rm n}$. If we make the further approximation that in the crust the amount by which the vortices move is small compared to $\varpi_s \approx 10^6$ cm, and thus consider $\varpi = \varpi_s$ constant, the equation above becomes

$$\frac{\partial \Delta\Omega(\varpi,t)}{\partial t} = -\beta \Delta\Omega(\varpi,t) \frac{\partial \Delta\Omega(\varpi,t)}{\partial \varpi} \,, \tag{24}$$

with

$$\beta = \varpi_s \frac{\gamma\mathcal{B}}{x_{\rm p}(1-\varepsilon_{\rm n}-\varepsilon_{\rm p})}(\varepsilon_{\rm n}-1). \tag{25}$$

Finally, with the substitution $\Delta^* = \beta\Delta\Omega$, we obtain as a general form of equation

$$\frac{\partial \Delta^*(\varpi,t)}{\partial t} = -\Delta^*(\varpi,t) \frac{\partial \Delta^*(\varpi,t)}{\partial \varpi}. \tag{26}$$

This is a Burgers equation, and allows travelling waves as solutions. In particular, let us consider the following initial conditions, corresponding to a large number of vortices accumulated close to the maximum of the pinning force, such that the lag is negligible prior to the vortex accumulation region, and approximately the maximum value $\Delta\Omega_M$ after an infinitesimally thin accumulation region located at ϖ_0:

$$\Delta\Omega(t=0) = \Delta\Omega_M \Theta(\varpi - \varpi_0) \,, \tag{27}$$

corresponding to (given that we take β to be a constant)

$$\Delta^*(t=0) = \Delta^*_M \Theta(\varpi - \varpi_0) \,, \tag{28}$$

where $\Theta(x)$ is the Heaviside step function. A solution to this equation which conserves the total number of vortices (in the approximation ϖ_s = constant) is a fan wave:

$$\Delta^*(t,\varpi) = \frac{\varpi - \varpi_0}{t} \quad \text{for} \quad \varpi < \varpi_F, \tag{29}$$

$$\Delta^*(t,\varpi) = \Delta^*_M \quad \text{for} \quad \varpi \geq \varpi_F \,, \tag{30}$$

with $\varpi_F = v_F t$, with $v_F = \Delta^*_M$. For our physical variable, $\Delta\Omega$ this corresponds to

$$\Delta\Omega(t,\varpi) = \frac{\varpi - \varpi_0}{\beta t} \quad \text{for} \quad \varpi < \varpi_F, \tag{31}$$

$$\Delta\Omega(t,\varpi) = \Delta\Omega_M \quad \text{for} \quad \varpi \geq \varpi_F \,, \tag{32}$$

where the position of the front ϖ_F moves at a speed $v_F = \beta\Delta\Omega_M = -\Delta\Omega_M \varpi_s \frac{\gamma\mathcal{B}}{x_{\rm p}(1-\varepsilon_{\rm n}-\varepsilon_{\rm p})}(1-\varepsilon_{\rm n})$ (keeping in mind that in a pulsar the lag $\Delta\Omega$ is negative). After the wave has travelled a distance $d \approx 10^2$ cm, our approximation ($\varpi \frac{\partial}{\partial\varpi}\left[\Omega_{\rm n} + \varepsilon_{\rm n}(\Omega_{\rm p} - \Omega_{\rm n})\right] > 2\Omega_{\rm n}$) breaks down and one has once again $\kappa n_v \approx 2\Omega$. Furthermore, as the lag is below the critical value, one can expect repinning. However, the above analysis shows vortex accumulation can lead to rapid outward motion of vortices, on length scales much larger that the inter vortex motion, that may drive further avalanches as it travels through the medium.

The number of vortices in the front is (assuming ϖ constant)

$$N_{\rm v} = \int \frac{n_{\rm v}}{\kappa} {\rm d}S \approx 2\pi \int \frac{\varpi_s^2}{\kappa} \frac{\partial \Delta\Omega}{\partial \varpi} {\rm d}r$$
$$= \frac{\varpi_s^2}{\kappa} \Delta\Omega \Big|_{\varpi_0}^{\varpi_F} \approx \frac{\Delta\Omega_M}{\kappa} \,, \tag{33}$$

which is conserved by the solution.

Let us now consider the region upstream from the vortex accumulation region. Here, there must be a depletion region in which the lag has to change from its equilibrium value $\Delta\Omega_e$ to 0 over a short lengthscale. This can be determined by imposing that vortex density vanish, i.e.

$$\kappa n_{\rm v} = 2\Omega_{\rm n} + \varpi \frac{\partial \Omega_{\rm n}}{\partial \varpi} = 0 \,, \tag{34}$$

which gives, close to a point ϖ_d

$$\Omega_{\rm n} = \Omega_0 \left(\frac{\varpi_d}{\varpi}\right)^2 . \tag{35}$$

Expanding around ϖ_d in $\delta r = (\varpi - \varpi_0)$, we see that the lag decreases as

$$\Delta\Omega = \Delta\Omega_0 - 2\Omega_0 \frac{\delta r}{\varpi_0}. \tag{36}$$

For typical parameters, this gives a decrease in lag over a lengthscale $\delta r \approx$ 10–100 cm, which is the same lengthscale over which our approximation is valid.

Nevertheless, to continue our initial analysis, we will make the simplifying assumption that in this region the drop in lag can be approximated as a steep drop of the form

$$\Delta\Omega = \Delta\Omega_M \Theta(\varpi_d - \varpi) \,, \tag{37}$$

but one should keep in mind that this is at the limit of validity for using equation (24), given the estimate in (36) In this case, as vortex unpinning causes a perturbation in Magnus force due to the lack of vortices in their equilibrium positions, there will be a backward propagating unpinning avalanche. The solution corresponds to a forward moving shock that describes vortices moving out to fill the void, of the form

$$\Delta\Omega = \Delta\Omega_M \Theta(\varpi_d - \varpi) \,, \tag{38}$$

where the position of the shock is determined by $\varpi_d = v_S t$, with $v_S = \beta \Delta\Omega_M/2$.

5 UNPINNING VORTEX WAVES

In the previous section, we showed how, by solving analytically equation (19), we can describe an unpinning wave that travels as a shock in the fluid. In doing so, however, we have had to make the assumption that γ, the fraction of unpinned vortices, is a constant, and neglect the steady-state contribution to the vortex number density $\kappa n_{\rm v} \approx 2\Omega_{\rm n}$. In practice, this allows us to only evolve the equations of motion as long as $\varpi\partial_\varpi\Omega_{\rm n} \ll 2\Omega$.

To go beyond this approximation, we have to provide an evolution equation for the unpinned fraction γ. This is a complex problem, given that the microphysics that governs vortex pinning acts on scales much smaller than the hydrodynamical scale. Attempts have been made in this direction in the context of superfluid turbulence, in which case an additional equation is included to model the evolution of the vortex length (Mongiovì, Russo, & Sciacca 2017). Here, however, we will not derive a full mean-field description of vortex unpinning, but rather focus on how different prescriptions for short-timescale movement of vortices during an avalanche can affect astrophysical observables. Another approach to constructing global models was taken in Fulgenzi, Melatos, & Hughes (2017), where the angular velocity lag between the pulsars's superfluid interior and a rigid crust is considered as fluctuating according to a state-dependent Poisson process. In this case, local vortex motion and knock-on effects are not taken into account in the hydrodynamics.

In analogy with mean-field approaches to the study of sand piles and of self-organised critical systems more generally, we can assume that one has a time evolution equation for γ, with local terms which depend only on powers of γ itself, that govern the long-scale relaxation of the system close to equilibrium, due to random unpinning and repinning. The evolution equations for γ thus take the form

$$\frac{\partial \gamma}{\partial t} = \sum_n \alpha_n \gamma^n + \xi f(\gamma, \partial_r \gamma) \,, \tag{39}$$

where α_n and ξ are coefficients, and $f(\gamma, \partial_r\gamma)$ is a function of γ and its spatial derivatives that models transport of vortices. In standard SOC models, f would simply be a diffusion term of the form $f = \nabla^2\gamma$. In our case, the Magnus force sets a preferred direction for vortex motion, so we will consider different forms of advection terms rather than diffusion. The terms $\Sigma_n\alpha_n\gamma^n$ model the competition between unpinning and repinning on the microscopic level, and set the steady-state equilibrium of the system. The addition of noise to (39) can then lead to departures from equilibrium and avalanches. This is, however, a complex problem, well beyond the scope of the current analysis. Here, we intend to take a first step towards the analysis of the propagation of avalanches; therefore, we will neglect the terms $\Sigma_n\alpha_n\gamma^n$, that set the background equilibrium on timescales longer that those of an avalanche and simply analyse how a large perturbation propagates by considering an evolution equation of the form:

$$\frac{\partial \gamma}{\partial t} = \xi f(\gamma, \partial_r \gamma). \tag{40}$$

5.1. Vortex advection

Let us consider different setups to describe the evolution of the unpinned fraction γ, neglecting the entrainment for simplicity. Given the phenomenological nature of this investigation, we consider three setups.

In the first setup, we consider a non-linear problem with non-constant coefficient in the advection term so that we allow vortices to advect with the velocity that is equal to the velocity of the shock wave. This is done to synchronise the repining process and angular momentum exchange, and account for vortex unpinning in the front. We explicitly take into account the steady-state contribution $\kappa n_{\rm v} \approx 2\Omega_{\rm n}$ in equation (22), but assume that all vortices are unpinned in the front ($\gamma = 1$) in order to decouple the advection term in the lag from the equations of motion for γ. Our first setup (case I) thus takes the following form for $\Delta\Omega$:

$$\frac{\partial \Delta\Omega}{\partial t} = \frac{B}{x_{\rm p}} \varpi_s \Delta\Omega \frac{\partial \Delta\Omega}{\partial \omega} - 2\Omega\Delta\Omega \frac{\gamma \mathcal{B}}{x_{\rm p}} \,, \tag{41}$$

and the equation for γ is

$$\frac{\partial \gamma}{\partial t} = \frac{\mathcal{B}}{2x_{\rm p}} \varpi_s \Delta\Omega \frac{\partial \gamma}{\partial \omega}. \tag{42}$$

Equations (41) and (42) form a system to solve for two independent variables, γ and $\Delta\Omega$. An extension to this setup has been made by reducing $\mathcal{B}$ by a factor 10 in the first term on the right-hand side of equation (41), thus obtaining

$$\frac{\partial \Delta\Omega}{\partial t} = \frac{\mathcal{B}}{10x_{\rm p}} \varpi_s \Delta\Omega \frac{\partial \Delta\Omega}{\partial \omega} - 2\Omega\Delta\Omega \frac{\gamma \mathcal{B}}{x_{\rm p}}, \tag{43}$$

which corresponds to slowing down the velocity of free vortices and longer term evolution of the lag, while leaving unaltered the short-term dynamics leading to the glitch rise. This allows us to mimic the physical situation in which a fast rise is followed by an unpinning wave in which not all vortices are unpinned in the front, but still retain the numerical advantage of decoupling the advection terms in (43) and (42). Essentially, the velocity of the unpinning wave is reduced while that of the initial exponential rise is not.

In a second setup (case II), we allow advection of γ with a constant velocity equal to the initial velocity of the shock wave in $\Delta\Omega$. In this case, the equation describing the evolution of γ and $\Delta\Omega$ are

$$\frac{\partial \Delta\Omega}{\partial t} = \frac{\mathcal{B}}{x_{\rm p}} \varpi_s \Delta\Omega \frac{\partial \Delta\Omega}{\partial \omega} - 2\Omega\Delta\Omega \frac{\gamma \mathcal{B}}{x_{\rm p}}, \tag{44}$$

$$\frac{\partial \gamma}{\partial t} = \frac{\mathcal{B}}{2x_{\rm p}} \varpi_s \Omega_{\rm init} \frac{\partial \gamma}{\partial \omega}, \tag{45}$$

where $\Omega_{\rm init}$ is initial angular velocity. This case is interesting because here γ advects with a constant velocity that does not depend on spatial changes in lag. Decoupling these processes means that the exchange of angular momentum between normal and superfluid component does not affect the propagation of free vortices. Both in cases I and II, we provide as initial conditions a pulse in γ and a flat profile in $\Delta\Omega$, as shown in Figure 1. As we shall see the linear terms in the equations of motion for $\Delta\Omega$, in the presence of an increase in γ lead to an exponential rise and rapidly lead to a step in $\Delta\Omega$.

The third setup (case III) is closely related to case II with constant advection, but now the parameter γ is explicitly included in the equation for the lag $\Delta\Omega$, which is thus coupled to the evolution of γ. In order to make the problem numerically tractable, the linear term is also excluded and we have an equation in the same form as (24). The initial conditions differ from the previous ones, as the absence of a linear term mean that we cannot trigger a glitch simply with an increase in γ. Rather, we provide an initial step profile for γ and $\Delta\Omega$, meaning that the lag is already formed and we force vortices to move as a result of a previous, unspecified, and unpinning event. Examples of these initial conditions are also shown in Figure 1. The equations to solve are

$$\frac{\partial \Delta\Omega}{\partial t} = \frac{\mathcal{B}}{x_{\rm p}} \varpi_s \gamma \Delta\Omega \frac{\partial \Delta\Omega}{\partial \omega}, \tag{46}$$

$$\frac{\partial \gamma}{\partial t} = \frac{\mathcal{B}}{2x_{\rm p}} \varpi_s \Omega_{\rm init} \frac{\partial \gamma}{\partial \omega}. \tag{47}$$

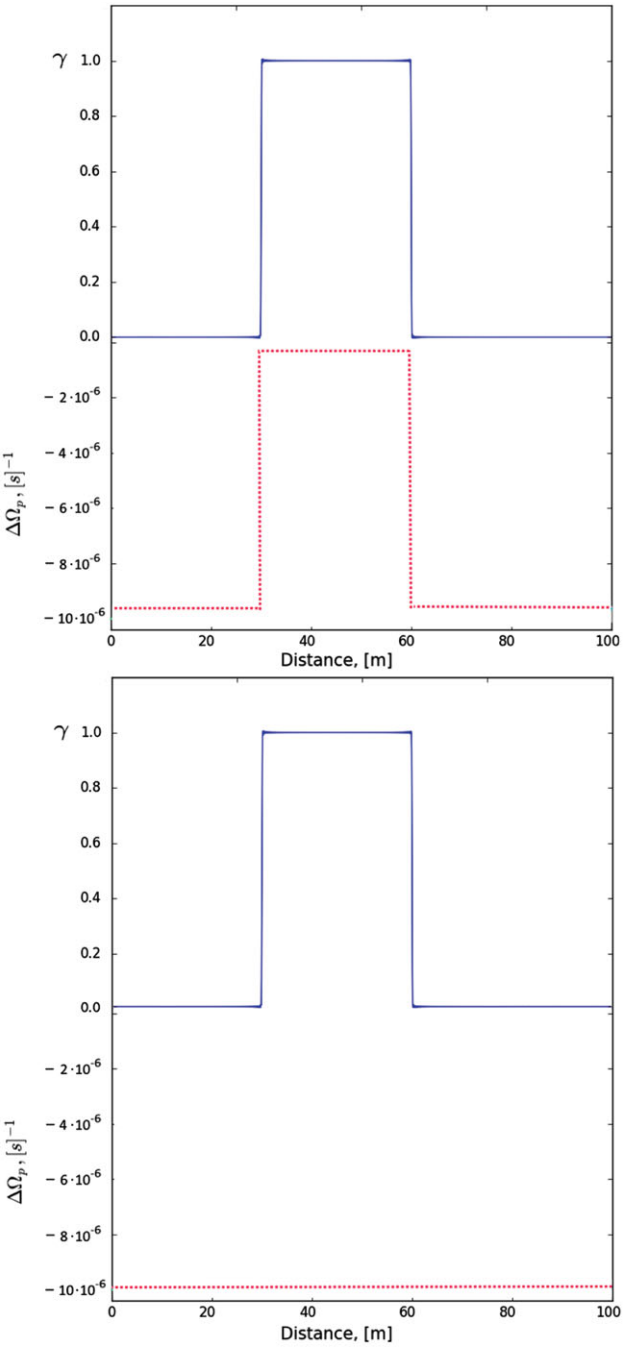

Figure 1. Examples of initial conditions for step profiles both in $\Delta\Omega$ and γ (top), as used in case III simulations, and those with a flat profile in $\Delta\Omega$ and step in γ, used in case I and II to initiate a glitch (bottom).

The three setups are summarised in Table 1.

These pairs of equations for the evolution of the lag and the fraction of unpinned vortices for the considered setups have been solved using the Dedalus spectral code (K. J. Burns, G. M. Vasil, J. S. Oishi, D. Lecoanet, B. P. Brown, and E. Quataert, in preparation) as well as with a two-order Godunov finite difference code. Tests of the numerical solution's accuracy have also been implemented for both codes by means of

Table 1. Summary of the three different prescriptions that are used to couple vortex motion (evolution of the unpinned vortex fraction γ) and angular momentum exchange (evolution of the lag $\Delta\Omega$).

Case I:
$\frac{\partial\Delta\Omega}{\partial t} = \frac{\mathcal{B}}{x_\mathrm{p}}\varpi_s\Delta\Omega\frac{\partial\Delta\Omega}{\partial\omega} - 2\Omega\Delta\Omega\frac{\gamma\mathcal{B}}{x_\mathrm{p}}$
$\frac{\partial\gamma}{\partial t} = \frac{\mathcal{B}}{2x_\mathrm{p}}\varpi_s\Delta\Omega\frac{\partial\gamma}{\partial\omega}$
Case II:
$\frac{\partial\Delta\Omega}{\partial t} = \frac{\mathcal{B}}{x_\mathrm{p}}\varpi_s\Delta\Omega\frac{\partial\Delta\Omega}{\partial\omega} - 2\Omega\Delta\Omega\frac{\gamma\mathcal{B}}{x_\mathrm{p}}$
$\frac{\partial\gamma}{\partial t} = \frac{\mathcal{B}}{2x_\mathrm{p}}\varpi_s\Omega_\mathrm{init}\frac{\partial\gamma}{\partial\omega}$
Case III:
$\frac{\partial\Delta\Omega}{\partial t} = \frac{\mathcal{B}}{x_\mathrm{p}}\varpi_s\gamma\Delta\Omega\frac{\partial\Delta\Omega}{\partial\omega}$
$\frac{\partial\gamma}{\partial t} = \frac{\mathcal{B}}{2x_\mathrm{p}}\varpi_s\Omega_\mathrm{init}\frac{\partial\gamma}{\partial\omega}$

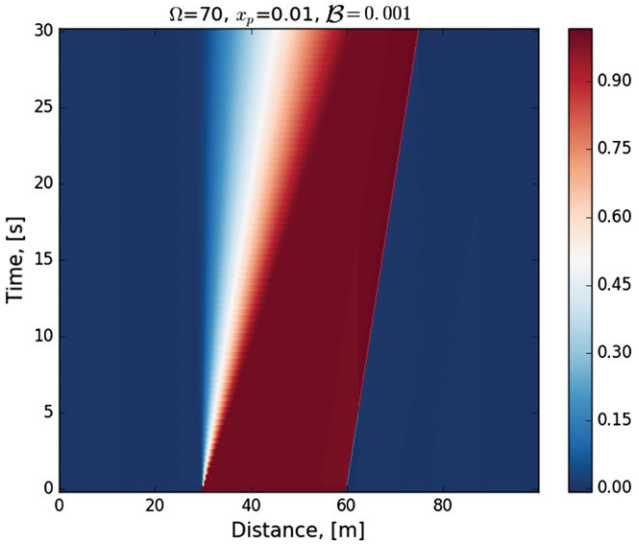

Figure 2. Evolution of γ for case I with step initial condition, as described in the text and seen in Figure 1. The fraction of unpinned vortices decreases, thus approximating a repining process.

direct measurements of the velocity of a shock wave in test problems.

We assume a constant mutual friction parameter $\mathcal{B}$ and assume that the distance travelled by vortices is small compared to the radius ϖ_s, which we take constant. In a realistic case, mutual friction will depend on density and composition, thus on ϖ_s, and will be due to different processes in the crust and core, thus depending strongly on the location of our simulation box in the star.

A typical evolution of $\Delta\Omega$ is shown in Figure 2 for the synchronised velocity case (case I), while the evolution of γ is shown in Figure 3 . The pattern of the process is as follows: an initially flat profile creates a difference in angular velocities, due to the exchange of angular momentum between a normal and a superfluid component, and creates large gradients in $\Delta\Omega$. The decrease in lag then spreads out. The typical time for the rise in frequency is less than a second in our setup,

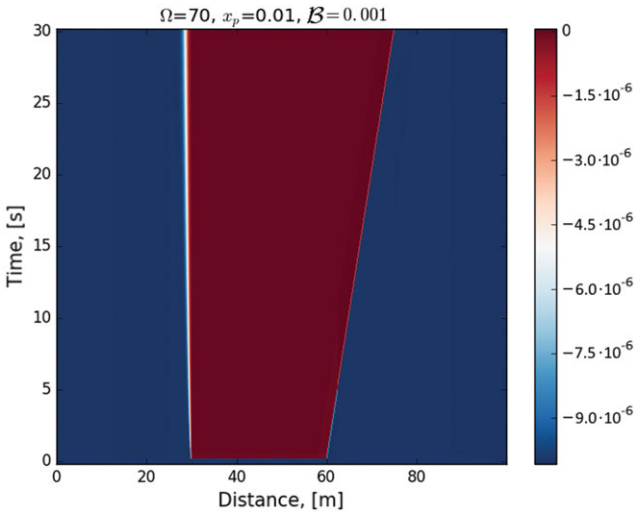

Figure 3. Evolution of $\Delta\Omega$ for case I with step initial condition, as described in the text and seen in Figure 1.

but strongly depends on the poorly known mutual friction parameter $\mathcal{B}$.

The evolution of the fraction of unpinned vortices is characterised by a decrease with time, which mimics vortex repining. Note that, in order to solve the equations numerically, artificial dissipation has been introduced.

Let us now turn our attention to the (internal) torque acting on the protons, i.e., on the 'normal' component of the star that is coupled to the magnetic field and thus to the observable electromagnetic emission. Locally, the proton angular velocity evolves as

$$\Omega_\mathrm{p} = \Omega_\mathrm{n} - \Delta\Omega\,. \tag{48}$$

The equation for the proton component for cases I and II in Table 1 is

$$\Omega_\mathrm{p} = \Omega_\mathrm{n} - \int\left(\frac{\mathcal{B}}{x_\mathrm{p}}\varpi_s\Delta\Omega\frac{\partial\Delta\Omega}{\partial\omega} - 2\Omega\Delta\Omega\frac{\gamma\mathcal{B}}{x_\mathrm{p}}\right)\mathrm{d}t\,. \tag{49}$$

And for case III is

$$\Omega_\mathrm{p} = \Omega_\mathrm{n} - \int\frac{\mathcal{B}}{x_\mathrm{p}}\varpi_s\gamma\Delta\Omega\frac{\partial\Delta\Omega}{\partial\omega}\mathrm{d}t\,. \tag{50}$$

In order to consider the motion of a rigid crust, we will average over the interval by integrating between $[\varpi_1\,,\varpi_2]$ that in our case represent the boundaries of our computational domain, i.e., minimum and maximum radial distance in a star at which the evolution of a system is simulated. This leads to

$$\langle\dot{\Omega}_\mathrm{p}\rangle = \langle\dot{\Omega}_\mathrm{n}\rangle - \frac{1}{\varpi_1-\varpi_2}\int_{\varpi_1}^{\varpi_2}\left(\frac{\varpi_s\mathcal{B}}{x_\mathrm{p}}\Delta\Omega\frac{\partial\Delta\Omega}{\partial\omega} - 2\Omega\Delta\Omega\frac{\gamma\mathcal{B}}{x_\mathrm{p}}\right)\mathrm{d}\omega\,, \tag{51}$$

and

$$\langle\dot{\Omega}_\mathrm{p}\rangle = \langle\dot{\Omega}_\mathrm{n}\rangle - \frac{1}{\omega_1-\omega_2}\int_{\omega_1}^{\omega_2}\frac{\mathcal{B}}{x_\mathrm{p}}\varpi_s\gamma\Delta\Omega\frac{\partial\Delta\Omega}{\partial\omega}\mathrm{d}\omega\,. \tag{52}$$

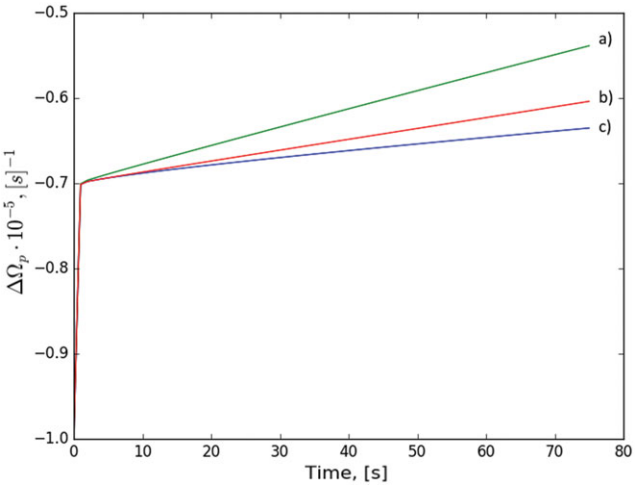

Figure 4. Comparison of the charged component evolution for the different setups. (a) Synchronised velocity setup (case I): [(41), (42)] with an initially flat profile for $\Delta\Omega$ and step in γ; (b) Constant advection setup (case III) [(46), (47)] with initial step profiles in both $\Delta\Omega$ and γ; (c) Synchronised velocity (case I) with artificially decreased speed of free vortex propagation ($\mathcal{B}$ reduced as described in the text).

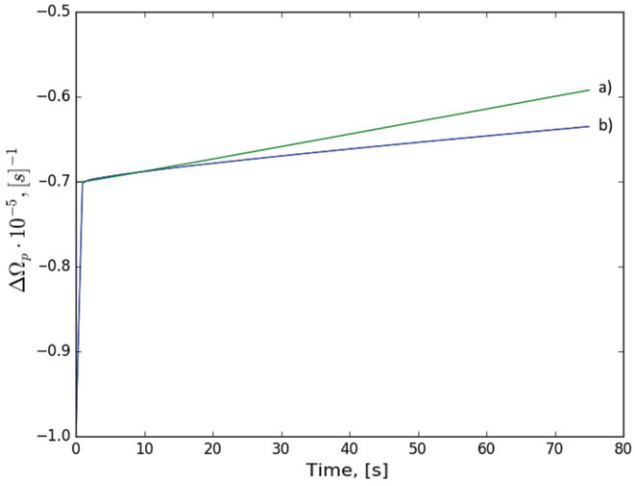

Figure 5. Comparison of the charged component evolution for two setups with the constant advection term. (a) Constant advection (case II) ([(44), (45)]; (b) Constant advection of knocked on vortices (case III) [(46), (47)].

In this initial calculation, we neglect $\langle\dot{\Omega}_n\rangle$, in the assumption that the proton fluid has a smaller moment of inertia and thus the background average neutron rotation rate does not change very much compared to the proton rotation rate, i.e., $|\langle\dot{\Omega}_p\rangle| >> |\langle\dot{\Omega}_n\rangle|$. This is not always the case, however, and a more realistic calculation should retain both terms (Haskell et al. 2012).

Using the previously obtained results for the lags $\Delta\Omega$, we average over the computational domain for each setup and show the results in Figure 4. The comparison of the related scenarios for constant advection are shown in Figure 5.

Generally, for the reference value $\mathcal{B} = 10^{-3}$ as well as for the lower value $\mathcal{B} = 10^{-4}$, the behaviour of the 'normal' component is characterised by a rapid exponential rise, on timescales of seconds, followed by a slower, apparently linear, increase in frequency on timescales of a minute. This behaviour is, in fact, suggestive of what was observed for the 1989 glitch of the Crab pulsar, in which a fast and unresolved rise was followed by a slower component (Lyne, Smith, & Pritchard 1992).

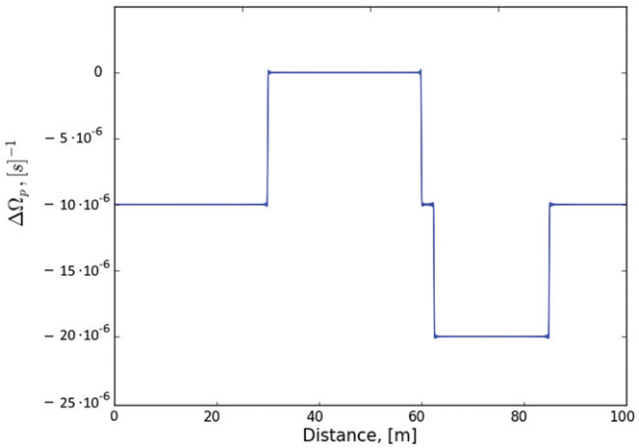

Figure 6. Initial condition for the lag with a sequence of steps, physically corresponding to different pinning strengths.

As can be seen from Figures 4 and 5, the rise time for the three major setups is almost the same, while there are differences in the linear responses. However, the differences in frequency and frequency derivative are still small, and of order of 30% for the frequency derivative, indicating that in the study of the short-term rise and post-glitch behaviour, the choice of setup does not strongly influence the conclusions.

5.2. Glitch precursors

We now discuss how differences in pinning strengths in the neutron star crust can influence the evolution of the frequency, and in particular whether unpinning in lower strength pinning regions can trigger unpinning and glitches in regions with stronger pinning and thus larger lags. In other words, we are interested in examining whether smaller unpinning events, that may show up simply as changes in spin-down rate, rather than steps in frequency, could be glitch precursors, as observed, for example, in the pulsar J0537–6910 (Middleditch et al. 2006).

To do this, let us consider the evolution of a system with the lag between the normal and the superfluid component that is not simply a step but a sequence of steps. Initial conditions for this case are shown in Figure 6. Different lags $\Delta\Omega$ correspond to a different pinning strength, as stronger pinning leads to a larger critical lag.

To study the evolution, we use the equations from case III, i.e., [(46), (47)], with initial conditions for γ being a step located at the same distance and with the same width as in Figure 1. Note that the lag in the second region is twice that

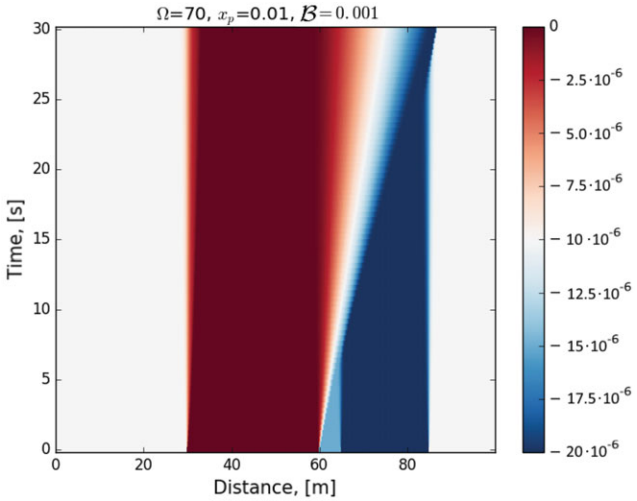

Figure 7. Evolution of the lag $\Delta\Omega$ for the initial conditions in Figure 6.

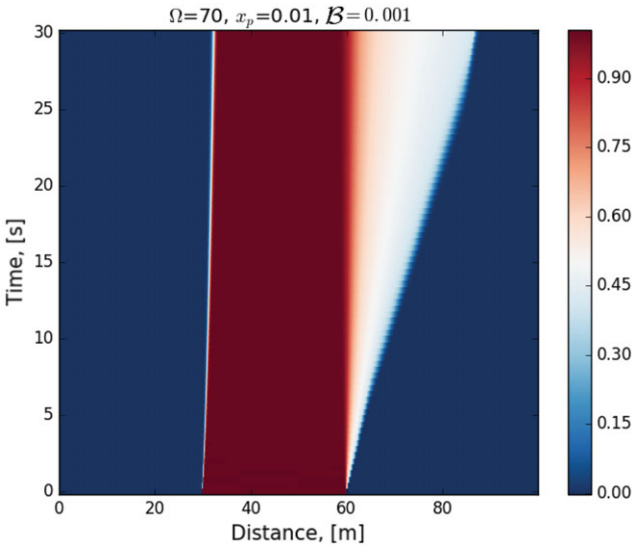

Figure 8. Evolution of the parameter γ for the initial conditions in Figure 6.

in the first (i.e., the pinning is twice as strong). Larger differences can be expected in neutron star crusts, but cannot be treated in our current numerical setup. The results of solving (46) and (47) are in Figure 7 for the evolution of the lag $\Delta\Omega$, and in Figure 8 for the evolution γ.

A propagating wave begins to travel due to the unpinned vortices. When reaching the region with a higher lag, the transfer of angular momentum is much more effective and this results in increase of rotational rate as seen in the evolution of the charged component. Due to the presence of regions with a non-uniform distribution of pinning forces, and thus of lag between the normal and the superfluid component, in real NSs a more complex pattern is likely to appear. The fraction of free vortices, in turn, goes through two transitions. The first transition occurs when free vortices reach the region with a higher lag, where the amount of free vortices that are able to continue moving further decreases. The second transition

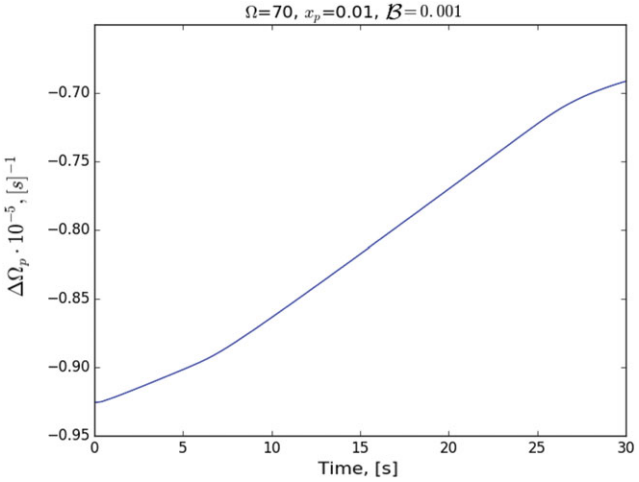

Figure 9. Evolution of the lag $\Delta\Omega$ for initial conditions in Figure 6. The difference in critical lags leads to an initial slower rise, followed by a faster increase in frequency when the unpinning front reaches the stronger pinning region. Even larger differences in critical lag (and equivalently pinning force) could lead to a faster and larger glitch after the initial precursor, but are numerically intractable in our setup.

occurs when vortices pass this region. Their amount then decreases with a constant rate.

The evolution of the charged component is shown in Figure 9. Unlike the other setups now, the initial rise time is much longer. When free vortices reach the region with a higher lag, the slope increases and decreases again after passing the region. This means that amplification of the initial rise is possible if in the outer region the pinning force is stronger.

As a result, the star's angular velocity may change not only abruptly, showing a glitch-like rise, but also more gradually, depending on local properties of the region, i.e., the distribution of areas with uneven pinning but also the local value of the mutual friction and the moment of inertia of the fluid. In general, our results indicate that an initial increase in the spin-down rate (decrease in absolute value) may be the precursor of a larger glitch, although the differences in pinning required for this scenario are larger than those that our numerical setup allows. We are thus unable to simulate physically realistic sizes and timescales.

This behaviour, however, is similar to what has been observed in pulsar J0537–6910 (Middleditch et al. 2006; Ferdman et al. 2018), where the preglitch behaviour exhibits brief 'upticks' and 'downticks' in $\dot{\nu}$ of varying amplitudes and durations. The timescales are different from those that we simulate, due to our numerical limitations. However, our results, although they depend on poorly known physical quantities in the crust of the star, indicate that it is possible that the same process in a NS may lead to different phenomena. In the case presented here, the interaction between the superfluid and the normal component gives a rise to a glitch precursor, while the same process in an isolated strong pinning region leads to a standard glitch.

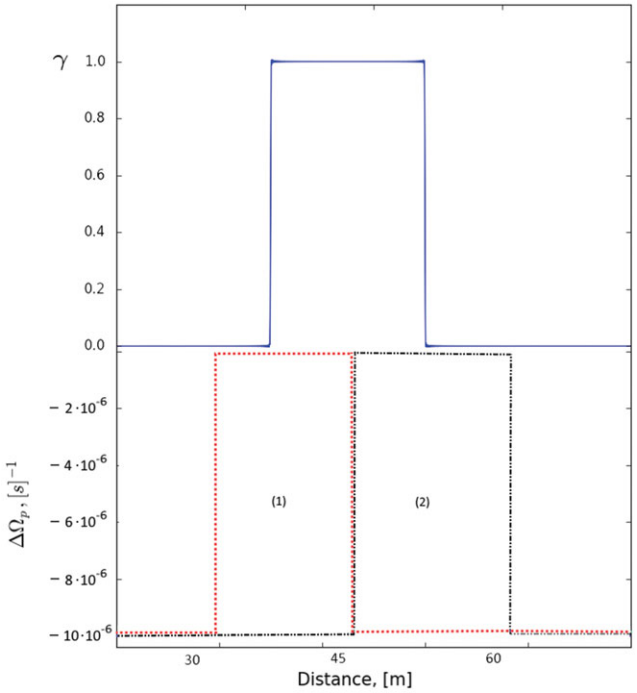

Figure 10. Initial conditions for γ and $\Delta\Omega$ for the antiglitch test cases described in the text. Two cases are shown: (1) conditions leading to and increase of the angular velocity; (2) conditions leading to a decrease of the angular velocity, or 'antiglitch'.

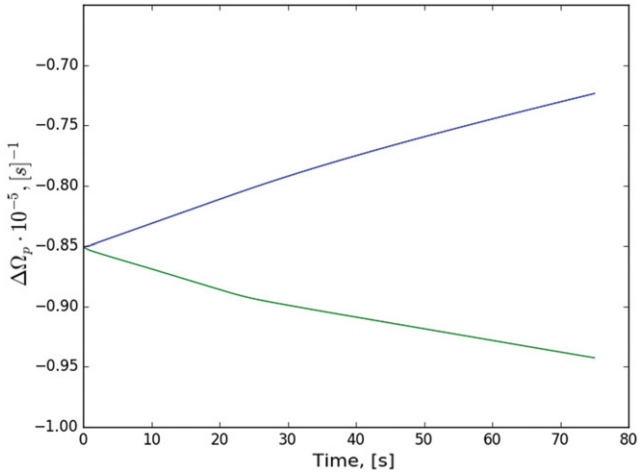

Figure 11. Evolution in time of the angular velocity of a charged component for a glitch–'antiglitch' test. The blue rising curve corresponds to the glitch-like rise, the green decreasing curve to the antiglitch-like behaviour.

5.3. Frequency decrease and antiglitches

The non-linear evolution we consider can, however, lead to other surprising results in the framework of the standard glitch model. In particular, we find setups in which not only an increase, but also a decrease in a star's angular velocity can be obtained. To do this, we study the evolution of a system with step initial conditions using the setup in case III, corresponding to equations (46) and (47). Initial conditions for two cases are shown in Figure 10.

The difference between the two setups is that in the first case the region with null lag is located 'behind' the region with free vortices and these regions partially coincide while in the second case the null-lag region is located further out than the front. Results for this case are shown in Figure 11.

As can be seen from the figure, unpinned vortices in the area behind the zero lag region start to exchange angular momentum, which tends to increase the angular velocity. However, propagation tends to decrease the extent of the coupled region at a faster rate, resulting in an 'anti-glitch', i.e., a local decrease of angular velocity. This behaviour is intriguing, given observations of such antiglitches in magnetars (Archibald et al. 2013). However, since the decrease in frequency is the result of a competition of process, it is possible that the overall antiglitch behaviour is the consequence of our particular setup. As for the influence of the numerical dissipation, several tests have been made in order to study the changes of the 'antiglitch' behaviour appearance as well as the time of rise. It was found that it has minimal impact on the results, and the feature is robust for our setup. However, further investigation in a more realistic scenario will be required to determine whether this evolution is physically significant.

Other initial conditions, in fact, result in much more predictable evolutions and show an increase of angular velocity, as shown in Figure 11 as a blue curve, while the 'antiglitch' is shown as green curve.

Let us study in detail the evolution of the solution where the 'antiglitch' appears. For this, we show four snapshots for γ and $\Delta\Omega$ on Figure 12.

Initially, unpinned vortices form a small peak in $\Delta\Omega$ behind the main region of the lag. This peak grows with time until it reaches the main region with zero lag. Next, these two regions start to interact, forcing the initial region with vortices to decrease in size and move. Further interaction makes both regions move, γ decrease and an unpinning wave propagate. The overall outcome, whether an increase or decrease in frequency, is thus sensitive to the timescale on which these processes occur and the speed of propagation of γ.

6 PARAMETER STUDY

To study the influence of the different parameters on the evolution of the solution, we first change the mutual friction, i.e., the $\mathcal{B}$ parameter. In a realistic star, this parameter depends on density, and will thus depend on the location of the computational box in the NS. Since we take the mutual friction to be constant, it represents the averaged value over the computational domain, i.e., over the path of vortex movement. Decreasing the mutual friction will generally increase the timescale for the rise, while higher mutual friction leads to a faster glitch, for a fixed initial setup.

The dependance is intuitively correct since the mutual friction is the mechanism that is responsible for an angular's momentum transfer strength, it is a 'bridge' between the normal

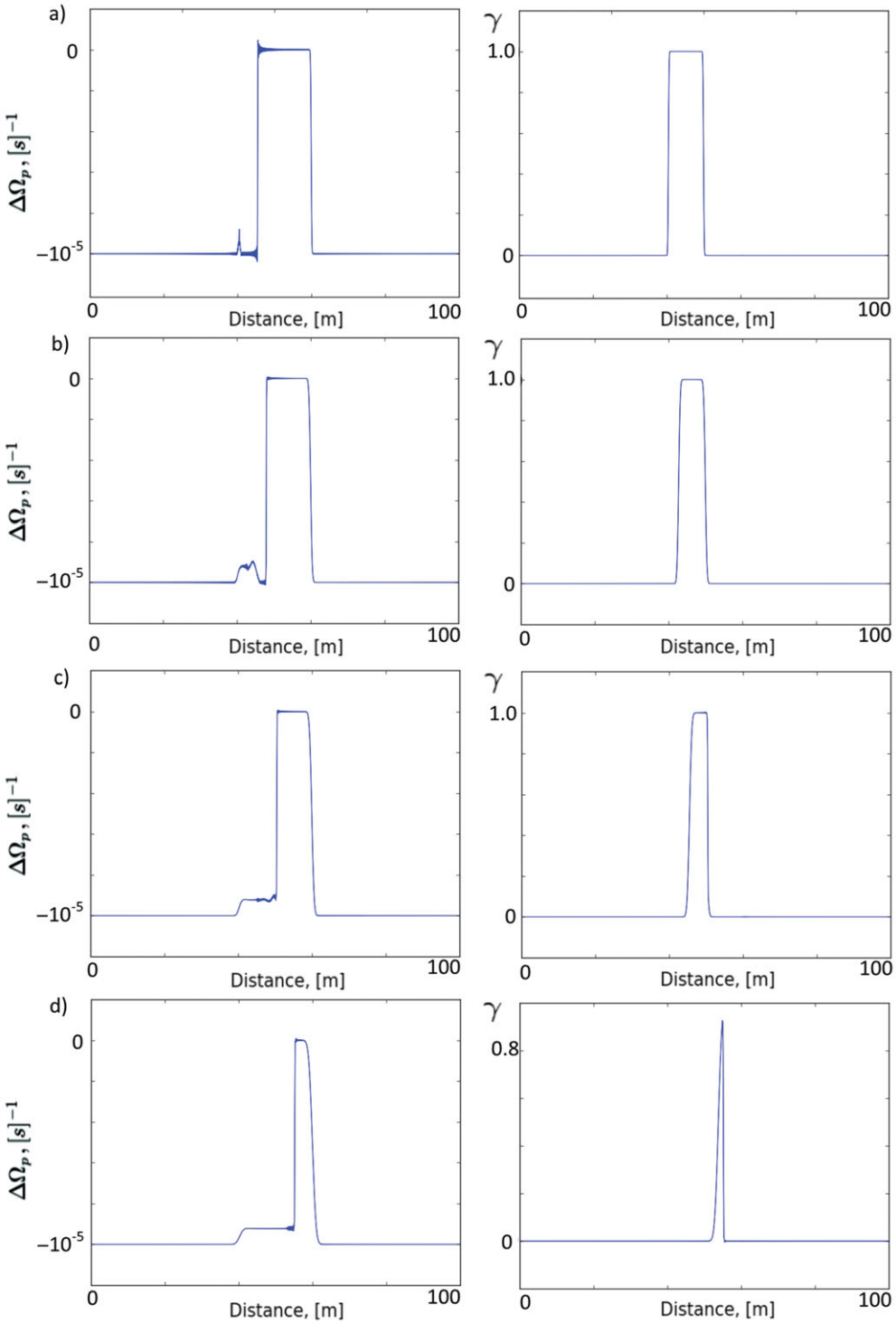

Figure 12. Snapshots of evolution in time for $\Delta\Omega$ (left column) and γ (right column) (a) After 1 s; (b) after 6 s; (c) after 12 s; (d) after 30 s.

and the superfluid component, and the behaviour can easily be understood from equation (21) for the coupling timescale between components, if we neglect non-linear terms. The consequences of the mutual friction variations are shown in Figure 13 for case II as a representative of a non-constant advection family and in Figure 14 for case I with constant advection.

Note that $\gamma\mathcal{B}$ is the parameter that affects the character of a glitch. Its evolution leads, for example, to different kinds of relaxation even in a single pulsar, given that in a realistic

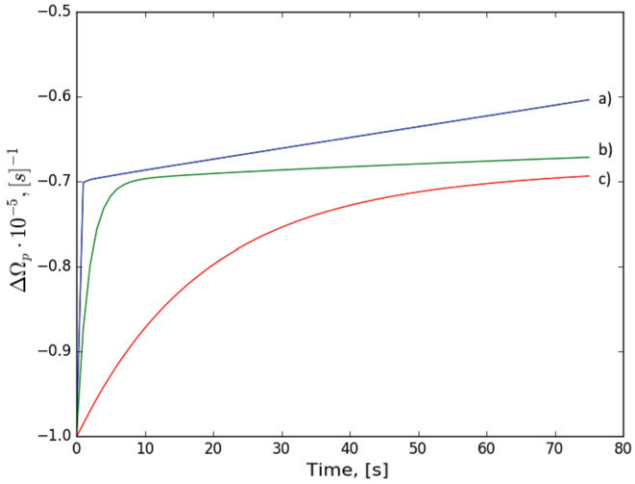

Figure 13. Influence of the mutual friction parameter $\mathcal{B}$ on the speed of rise for case II. (a) $\mathcal{B} = 10^{-3}$; (b) $\mathcal{B} = 10^{-4}$; (c) $\mathcal{B} = 10^{-5}$.

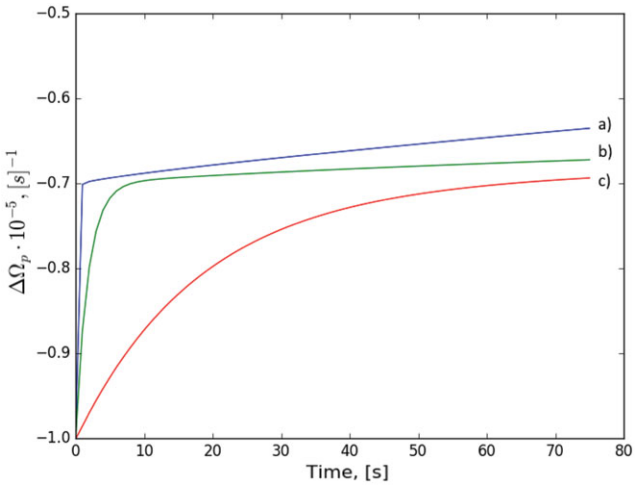

Figure 14. Influence of the mutual friction parameter $\mathcal{B}$ on the speed of rise for case I. (a) $\mathcal{B} = 10^{-3}$; (b) $\mathcal{B} = 10^{-4}$; (c) $\mathcal{B} = 10^{-5}$.

system it is not constant in time (due to vortex pinning and unpinning) or constant along the path of vortex movement (Haskell & Antonopoulou 2014).

Next, let us study the influence of the angular frequency of a star. In all of the simulations, the angular frequency is initially equal to 70 s^{-1} which is approximately equal to the Vela pulsar's angular velocity. In order to see how the unpinning wave propagation reacts, we experiment with changing it to 7 s^{-1}. Results are shown on Figure 15. As expected from the linear analysis in (21), decreasing the angular velocity of a star increases the rise time but does not strongly affect the results in the non-linear regime.

Changing the proton fraction x_p acts as a simple rescaling of the mutual friction parameter $\mathcal{B}$ in our simple setup, and thus does not significantly affect the results for reasonable values of the parameter in the crust.

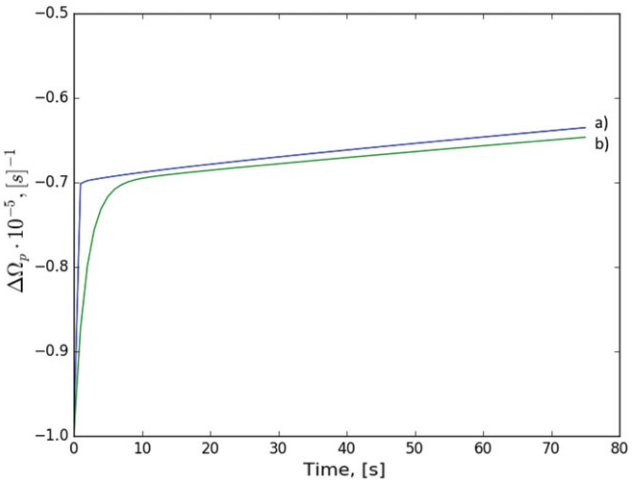

Figure 15. Influence of the angular frequency Ω of a star on the charged component evolution for constant advection, i.e., case I: (a) $\Omega = 70$ s^{-1}, (b) $\Omega = 7$ s^{-1}.

7 CONCLUSIONS

In this paper, we have outlined a formalism for simulating the motion of superfluid vortex over-densities and fronts in hydrodynamical two-fluid simulations of pulsar glitches. We have shown that accounting explicitly for the differential rotation that is built up due to vortex accumulation introduces additional non-linear terms in the evolution equations for the lag $\Delta\Omega$, which allow for travelling waves ('unpinning' waves) as solutions. The observational consequence of this setup is that coupling between the normal and superfluid components of the neutron star, mediated by vortex motion, can lead not only to exponential terms in the evolution of a pulsar's frequency, but also linear terms, and generally slower, longer term variations in the spin frequency of a neutron star.

We take our model one step further and introduce an additional parameter to the evolution, namely the fraction of free vortices in the system, γ. This parameter encodes the sub-grid physics of vortex motion that is not resolved on a hydrodynamical level, and depends on the complex quantum mechanical statistical processes that govern vortex interactions at a microscopic level. While microphysical simulations have been relatively successful in investigating the relation between pulsar glitches and SOC (Warszawski & Melatos 2011; Haskell & Melatos 2015) in small systems, or pinning of a vortex to a single defect (Wlazłowski et al. 2016), they are still not at the level where contact can be made with large-scale descriptions. We thus propose three phenomenological models for vortex motion, all of which mimic advection of free vortices together with propagating fronts in the lag between the normal component and the superfluid neutrons.

We study the evolution of the lag $\Delta\Omega$ and the free vortex fraction γ in several setups for all three our prescriptions for varying mutual friction parameters $\mathcal{B}$ and rotation rates Ω. The main conclusion is that localised unpinning leads to an initial rapid rise, on the timescale of seconds or less for

mutual friction parameters $\mathcal{B} > 10^{-4}$, as one may expect due to electron scattering of magnetised vortex cores in the presence of superconducting protons (Alpar et al. 1984b), or due to Kelvin waves as the vortices move past nuclear clusters in the crust (Jones 1992; Epstein & Baym 1992). This phase is, however, generally followed by a slower, quasi-linear rise on timescales of a minute, which is similar to what was observed in the 1989 glitch of the Crab pulsar (Lyne et al. 1992). Overall, the prescription we use for motion of the vortex fraction has little influence on the exponential rise, which is mainly due to the linear terms, but impacts on the slower long-term evolution. Nevertheless, the evolution of the normal component frequency is qualitatively similar, with only modest differences in rotational rates and frequency derivatives, between the three cases, which gives us confidence that our conclusions are robust and do not depend strongly on how we approximate the sub-grid physics of vortex motion.

We have also investigated how changes in pinning strength, approximated by different initial conditions for the lag, can impact the evolution of the frequency and the glitch. We find that if there are regions in which pinning decreases with density, as one expects in the deep crust (Seveso et al. 2016), then an initial unpinning event may lead to a slow change in frequency as a precursor of a larger glitch, triggered when the unpinning front reaches the stronger pinning region. Such precursor events may, in fact, have been observed before a number of glitches in pulsar J0537–6910 (Middleditch et al. 2006; Ferdman et al. 2018), where 'upticks' and 'downticks' in $\dot{\nu}$ of varying amplitudes and durations were observed prior to several glitches.

We also find specific setups in which vortex motion can lead to a decrease in frequency, or an antiglitch, such as that observed in the magnetar 1E 2259+586 (Archibald et al. 2013). This behaviour is intriguing, as it would provide an explanation for this phenomenon in the standard glitch model [see also Kantor & Gusakov (2014) for an alternative approach]. In our setup, the feature is robust to changes in numerical dissipation, and does not appear to be a numerical artefact. Nevertheless, a more detailed study in a more realistic setup is necessary to understand whether such an evolution is physically significant and would occur in a neutron star.

Despite the uncertainties, both due to the implementation of vortex motion, and poorly constrained physical parameters in the interior of the neutron stars, our simple models highlight the importance of allowing for vortex motion and accumulation in hydrodynamical simulations, as this allows for new and qualitatively different behaviour before, during and after a glitch. On the other hand, our models are also further confirmation that the large-scale response of the star strongly impacts on conclusions drawn from small-scale vortex dynamics alone, as was already shown to be the case for size and waiting time distributions (Haskell 2016). Future work should thus focus on further bridging the gap in scales between microscopic quantum mechanical simulations of vortex motion and large-scale hydrodynamical models of superfluid neutron stars.

PASA, 35, e020 (2018)
doi:10.1017/pasa.2018.12

ACKNOWLEDGEMENTS

We acknowledge support from the Polish National Science Centre (SONATA BIS 2015/18/E/ST9/00577, P.I.: B.Haskell) and from the European Union's Horizon 2020 research and innovation programme under grant agreement no. 702713. Partial support comes from NewCompStar, COST Action MP1304.

We thank Varadarajan Parthasarathy and Morgane Fortin for constructive discussions.

REFERENCES

Akbal, O., Alpar, M. A., Buchner, S., & Pines, D. 2017, MNRAS, 469, 4183
Alpar, M. A., Pines, D., Anderson, P. W., & Shaham, J. 1984a, ApJ, 276, 325
Alpar, M. A., Langer, S. A., & Sauls, J. A. 1984b, ApJ, 282, 533
Anderson, P. W., & Itoh, N. 1975, Nature, 256, 25
Andersson, N., & Comer, G. L. 2006, CQGra, 23, 5505
Andersson, N., Glampedakis, K., Ho, W. C. G., & Espinoza, C. M. 2012, PhRvL, 109, 241103
Andersson, N., Sidery, T., & Comer, G. L. 2006, MNRAS, 368, 162
Andersson, N., Sidery, T., & Comer, G. L. 2007, MNRAS, 381, 747
Antonelli, M., & Pizzochero, P. M. 2017, MNRAS, 464, 721
Antonopoulou, D., Espinoza, C. M., Kuiper, L., & Andersson, N. 2018, MNRAS, 473, 1644
Archibald, R. F., et al. 2013, Nature, 497, 591
Baym, G., Pethick, C., & Pines, D. 1969, Nature, 224, 673
Chamel, N. 2012, PhRvC, 85, 035801
Chamel, N. 2013, PhRvL, 110, 011101
Chamel, N. 2017, J. Low Temp. Phys., 189, 328
Cheng, K. S., Pines, D., Alpar, M. A., & Shaham, J. 1988, ApJ, 330, 835
di Santo, S., Burioni, R., Vezzani, A., & Muñoz, M. A. 2016, PhRvL, 116, 240601
Dodson, R. G., McCulloch, P. M., & Lewis, D. R. 2002, ApJ, 564, L85
Epstein, R. I., & Baym, G. 1992, ApJ, 387, 276
Espinoza, C. M., Antonopoulou, D., Stappers, B. W., Watts, A., & Lyne, A. G. 2014, MNRAS, 440, 2755
Ferdman, R. D., Archibald, R. F., Gourgouliatos, K. N., & Kaspi, V. M. 2018, ApJ, 852, 123
Finne, A. P., et al. 2003, Nature, 424, 1022
Fulgenzi, W., Melatos, A., & Hughes, B. 2017, MNRAS, 470, 4307
Glampedakis, K., & Andersson, N. 2009, PhRvL, 102, 141101
Haskell, B. 2016, MNRAS, 461, L77
Haskell, B., & Antonopoulou, D. 2014, MNRAS, 438, L16
Haskell, B., & Melatos, A. 2015, IJMPD, 24, 1530008
Haskell, B., & Melatos, A. 2016, MNRAS, 461, 2200
Haskell, B., & Sedrakian, A. 2017, preprint (arXiv 1709.10340)
Haskell, B., Pizzochero, P. M., & Sidery, T. 2012, MNRAS, 420, 658
Ho, W. C. G., Espinoza, C. M., Antonopoulou, D., & Andersson, N. 2015, SciA, 1, e1500578
Jones, P. B. 1990, MNRAS, 243, 257
Jones, P. B. 1992, MNRAS, 257, 501
Kantor, E. M., & Gusakov, M. E. 2014, ApJ, 797, L4
Lyne, A. G., Smith, F. G., & Pritchard, R. S. 1992, Nature, 359, 706

Mastrano, A., & Melatos, A. 2005, MNRAS, 361, 927
Melatos, A., Peralta, C., & Wyithe, J. S. B. 2008, ApJ, 672, 1103
Mendell, G. 1991, ApJ, 380, 515
Middleditch, J., Marshall, F. E., Wang, Q. D., Gotthelf, E. V., & Zhang, W. 2006, ApJ, 652, 1531
Migdal, A. B. 1959, NuPhA, 13, 655
Mongiovì, M. S., Russo, F. G., & Sciacca, M. 2017, MNRAS, 469, 2141
Newton, W. G., Berger, S., & Haskell, B. 2015, MNRAS, 454, 4400
Pizzochero, P. M. 2011, ApJ, 743, L20
Pizzochero, P. M., Antonelli, M., Haskell, B., & Seveso, S. 2017, NatAs, 1, 0134
Prix, R. 2004, PhRvD, 69, 043001
Ruderman, M. 1969, Nature, 223, 597
Seveso, S., Pizzochero, P. M., & Haskell, B. 2012, MNRAS, 427, 1089
Seveso, S., Pizzochero, P. M., Grill, F., & Haskell, B. 2016, MNRAS, 455, 3952
Sidery, T., Passamonti, A., & Andersson, N. 2010, MNRAS, 405, 1061
Warszawski, L., & Melatos, A. 2011, MNRAS, 415, 1611
van Eysden, C. A. 2014, ApJ, 789, 142
Warszawski, L., & Melatos, A. 2013, MNRAS, 428, 1911
Warszawski, L., Melatos, A., & Berloff, N. G. 2012, PhRvB, 85, 104503
Watanabe, G., & Pethick, C. J. 2017, Phys. Rev. Lett., 119, 062701
Wlazłowski, G., Sekizawa, K., Magierski, P., Bulgac, A., & Forbes, M. M. 2016, PhRvL, 117, 232701

Monthly Notices
of the
ROYAL ASTRONOMICAL SOCIETY

MNRAS **481,** L146–L150 (2018)
Advance Access publication 2018 September 20

doi:10.1093/mnrasl/sly175

Crust or core? Insights from the slow rise of large glitches in the Crab pulsar

B. Haskell,★ V. Khomenko, M. Antonelli and D. Antonopoulou

Nicolaus Copernicus Astronomical Center, Polish Academy of Sciences, ul. Bartycka 18, PL-00-716 Warsaw, Poland

Accepted 2018 September 19. Received 2018 September 10; in original form 2018 July 4

ABSTRACT

Pulsar glitches are attributed to the sudden recoupling of weakly coupled superfluid components in the neutron star interior. The transfer of angular momentum between the components is regulated by mutual friction, whose strength defines the spin-up time-scale of a glitch. Hence, observations of glitch rises can be used to shed light on the dominant microphysical interactions at work in the interior of the star. We present a model which naturally produces a fast spin-up followed by a more gradual rise, as observed in large glitches of the Crab pulsar, including the largest recent glitch of 2017. Our model is then used to determine whether the glitch driving region is located in the crust or core of the star. To do this, we compare our results to observations of large glitches in the Crab and Vela pulsars and obtain constraints on the mutual friction parameters that govern the coupling between the superfluid and the crust. Our results are consistent with theoretical estimates for mutual friction in the core for the Vela, but with estimates for the crust in the Crab. This suggests a crustal origin for Crab glitches, but an outer core contribution for Vela glitches.

Key words: stars: neutron – pulsars: individual (PSR J0534+2200, PSR J0835-4510).

1 INTRODUCTION

Neutron Stars (NSs) offer a unique opportunity to study fundamental physics in an extreme environment. In particular, the ratio of thermal to Fermi energy is generally small enough that neutrons are superfluid throughout most of the star.

Superfluidity has profound consequences for the dynamics of the system, as a superfluid is irrotational and can only mimic rigid body rotation by forming an array of quantized vortices. If vortex motion is impeded by 'pinning' (see e.g. Alpar 1977), the superfluid spin-down lags behind that of the normal component. The excess of angular momentum is then released catastrophically, leading to a fast increase in the observed frequency of the star, or a 'glitch' (Anderson & Itoh 1975).

A complete theory of glitches is still elusive (see Haskell & Melatos 2015, for a recent review of glitch models), despite hundreds of such events having now been observed in over 100 pulsars (e.g. Espinoza et al. 2011; Yu et al. 2013). One of the pressing open questions is the physical location of the glitch-driving superfluid reservoir. Early models suggested that only the crustal superfluid, where vortices pin to nuclear clusters, is involved in glitches; an expectation in accordance with initial observational estimates that approximately a few percent of the moment of inertia of the star is decoupled (Alpar et al. 1984a; Link, Epstein & Lattimer 1999).

This scenario has been, however, recently reevaluated by several authors (Andersson et al. 2012; Chamel 2013; Hooker, Newton & Li 2015) who have shown that the crustal superfluid alone cannot account for the measured activity of the Vela pulsar in the presence of strong crustal entrainment (e.g. Chamel 2012). Similar constraints are obtained when considering the largest glitches in pulsars, which generally require the core's superfluid to be, at least partially, contributing. This issue is still unsettled as there are considerable uncertainties on the entrainment parameters, superfluid gaps, and the nature of both the pinning force and the superfluid coupling time-scales due to mutual friction in the core and crust of NSs. These aspects introduce large uncertainties when trying to extract parameters related to the equation of state of NSs (Newton, Berger & Haskell 2015), or estimate their masses (Ho et al. 2015; Pizzochero et al. 2017).

Many pulsars, including the Crab, have spin-up size distributions consistent with power laws, and exponentially distributed waiting times (Melatos, Peralta & Wyithe 2008). On the other hand, the Vela and few other pulsars glitch regularly, with similar spin-up sizes each time.[1] Another such pulsar is PSR J0537-6910, for which there is even a strong correlation between size and waiting time to the next event (Middleditch et al. 2006; Antonopoulou et al. 2018). This difference in behaviour led to suggestions that the glitching mecha-

★ E-mail: bhaskell@camk.edu.pl

[1] A catalogue of observed glitches can be found at www.jb.man.ac.uk/pulsar/glitches.html (Espinoza et al. 2011).

nism may differ in these two classes of pulsars. Crustquakes might act as triggers in pulsars like the Crab (Akbal & Alpar 2018), while for Vela, vortex accumulation close to the strongest pinning layers ('snowplow' model, Pizzochero 2011) can explain the observed behaviour (Haskell, Pizzochero & Sidery 2012; Seveso, Pizzochero & Haskell 2012).

In this Letter, we attempt to shed light on the region where pinning occurs by studying the dynamics of the glitch rise. Until recently, the only strong observational constraint on a glitch's rise time came from single-pulse observations of the 2000 Vela glitch, which had a 3σ detection limit of $\lesssim$40 s (Dodson, McCulloch & Lewis 2002). A similar upper limit is inferred for the 2016 Vela glitch (Palfreyman et al. 2018). In both cases, the spin-up remains unresolved. However, Palfreyman et al. (2018) observed emission changes and excursions of the phase on time-scales of seconds, likely linked to the glitch evolution.

Features of the rise were recently revealed by observations of the largest recorded glitch in the Crab pulsar (Shaw et al. 2018), for which a fast rise (inferred to be less than 6 h long) is followed by a slower component on a time-scale of $\sim$2 d, a trait that had already been noted in another two large Crab glitches (Lyne, Smith & Pritchard 1992; Wong, Backer & Lyne 2001).

Such a two stage rise is not present in most theories (although note that thermal glitch models predict slower rise for younger pulsars, e.g. Larson & Link 2002), but can be modelled on general grounds by accounting for vortex accumulation in strong pinning regions, which leads to differential rotation and the propagation of vortex fronts. This naturally produces a slower component of the rise after the initial fast step in frequency (Khomenko & Haskell 2018).

In the following, we apply the model of Khomenko & Haskell (2018) to describe the (slow) rise of the 2017 Crab glitch, and the 2016 glitch of the Vela pulsar. We obtain constraints on the extent of the pinning region and crucially, on the local mutual friction parameters. The results suggest that glitches in the Vela pulsar originate in a higher density region in which mutual friction is stronger, thus strengthening the conclusion that the superfluid in the outer core of neutron stars must be involved.

2 MODEL

Let us consider a two component star, in which we have superfluid neutrons, labelled with 'n', and a charge neutral non-superfluid component of protons and electrons, labelled 'p'. If we define their rotation rates as $\Omega_{\rm n}$ and $\Omega_{\rm p}$ respectively (where we assume that $\Omega_{\rm p}$ is the observable rate tracked by the pulsed emission), and their difference, the lag, at time t and cylindrical radius ϖ, as $\Delta\Omega(t,\varpi) = \Omega_{\rm p}(t,\varpi) - \Omega_{\rm n}(t,\varpi)$, we can write an evolution equation of the form (Andersson & Comer 2006; Khomenko & Haskell 2018)

$$\frac{\partial \Delta\Omega}{\partial t} = \varpi\tilde{\beta}\Delta\Omega\frac{\partial \Delta\Omega}{\partial \varpi} - 2\tilde{\beta}\frac{\Omega_{\rm n}\Delta\Omega}{(1-\varepsilon_{\rm n})} + \frac{\dot{\Omega}_{\infty}}{(1-\varepsilon_{\rm n})}, \tag{1}$$

where $\varepsilon_{\rm n}$ is the neutron entrainment parameter, $\dot{\Omega}_{\infty}$ is the contribution of the external spin-down torque and $\tilde{\beta} = \gamma\mathcal{B}/\tilde{\epsilon}$, where we have defined $\tilde{\epsilon} = x_p(1-\varepsilon_n-\varepsilon_p)/(1-\varepsilon_n)$. The parameters $x_{\rm p}$ and $\varepsilon_{\rm p}$ are the proton fraction and entrainment parameter, respectively, γ the fraction of free vortices, and $\mathcal{B}$ the dimensionless mutual friction parameter. For simplicity, and in order to compare our results directly with observational results from which a pre-glitch spin-down model is subtracted, we will hereafter ignore the last term of equation (1). This is justified as a first approximation for the short time-scales involved in the rise, but can have an effect on some of the longer time-scales discussed in the following, over which changes in dynamical coupling may lead to spin-down rate changes (Haskell et al. 2012; Graber, Cumming & Andersson 2018).

The mutual friction parameter $\mathcal{B}$ determines the coupling time-scale between the two components. In the core, electron scattering off vortex cores is thought to give the strongest contribution, with $\mathcal{B} \approx 10^{-4}$ (Alpar, Langer & Sauls 1984b). In the crust, vortex interactions with the lattice are likely to dominate, but the exact value of $\mathcal{B}$ is highly uncertain. Current estimates range from $\mathcal{B} \approx 10^{-8}$ for phonon excitations, up to $\mathcal{B} \approx 10^{-1}$ for kelvon mutual friction (for a recent review see e.g. Haskell & Sedrakian 2017).

A fundamental parameter that governs the system's dynamics is the fraction of free vortices γ. This parameter depends on local interactions between neighbouring vortices, and to solve equation (1) an evolution equation for γ is needed. In Khomenko & Haskell (2018) several prescriptions for the advection of γ with the superfluid flow are tested, and found to give qualitatively similar results. Before moving on to the application of these prescriptions, it is, however, instructive to consider a simpler model.

2.1 Analytic model

We assume that the normal component is rotating rigidly with frequency $\Omega_{\rm p}$, and that the superfluid is perfectly pinned ($\gamma = 0$) with a locally uniform lag $\Delta\Omega_{\rm M}$ at the moment before the glitch. Unpinning of all vortices in this region leads to $\gamma = 1$ and according to equation (1) the recoupling of the two components proceeds over a time-scale

$$\tau_{\rm r} = \frac{1-\varepsilon_{\rm n}}{2\Omega_{\rm p}\tilde{\beta}}\,. \tag{2}$$

At the edges of the region over which $\Delta\Omega \longrightarrow 0$ strong differential rotation can develop, turning the first term in equation (1) much larger than the second term which is responsible for the rapid recoupling in equation (2). Physically this corresponds to vortex repinning and accumulation at the edges of the unpinning region, which creates a vortex sheet with high vortex density that most likely drives further unpinning (Pizzochero 2011; Warszawski, Melatos & Berloff 2012; Haskell 2016). In this case, we can simply consider the first term in equation (1), set $\gamma = 1$, and approximate the equation of motion for the lag $\Delta\Omega$ as

$$\frac{\partial \Delta\Omega}{\partial t} = \varpi_{\rm r}\tilde{\beta}\Delta\Omega\frac{\partial \Delta\Omega}{\partial \varpi}. \tag{3}$$

If we assume a constant cylindrical radius $\varpi_{\rm r} \approx 10^6$ cm and an initial condition $\Delta\Omega = H(\varpi-\varpi_0)\,\Delta\Omega_{\rm M}$, the solution of equation (3) takes the form of an outwards travelling fan wave

$$\Delta\Omega = \begin{cases} \Delta\Omega_{\rm M}(\varpi-\varpi_0)/(v_{\rm F}\,t) & \text{for} \quad \varpi < \varpi_{\rm F} \\ \Delta\Omega_{\rm M} & \text{for} \quad \varpi \geq \varpi_{\rm F} \end{cases}, \tag{4}$$

where ϖ_0 is the initial value of the front's position $\varpi_{\rm F}$, which subsequently moves at a speed

$$v_{\rm F} = -\varpi_{\rm r}\tilde{\beta}\Delta\Omega_{\rm M}\,. \tag{5}$$

Keeping in mind that in a pulsar $\Delta\Omega$ is negative, we find that $\varpi_{\rm F}$ moves towards larger radii (for a detailed description see Khomenko & Haskell 2018).

From angular momentum conservation, we have that the size of the glitch $\Delta\Omega_{\rm o}$ is related to the critical lag in the star $\Delta\Omega_{\rm M}$ via

$$\Delta\Omega_{\rm o} = -\frac{I_{\rm s}}{I_{\rm T}}\Delta\Omega_{\rm M}\,, \tag{6}$$

where $I_{\rm s}$ is the moment of inertia of the superfluid reservoir and $I_{\rm T} \sim 10^{45}$ g cm^2 the moment of inertia of the star that follows the

Table 1. Observational summary of relevant glitches.

Glitch	$\Delta\nu_G$ (10^{-6}Hz)	Rise limit τ_r	$\Delta\nu_d$ (10^{-7}Hz)	τ_d (d)	References[a]
Crab 1989	1.85	0.1 d	7	0.8	(1)
Crab 1996	0.66	0.5 d*	3.1	0.5	(2)
Crab 2017	14	0.45 d	11	1.7	(3)
Vela 2000	35	40 s	–	–	(4)
Vela 2017	16	48 s⋆	–	–	(5)

Notes: We present Crab glitches for which a delayed spin-up was observed, and the two Vela glitches for which high-resolution data have been used to constrain the rise time. $\Delta\nu_G$ denotes the unresolved initial spin-up, with an upper limit τ_r for its rise time-scale, and $\Delta\nu_d$ the delayed component, fitted as an exponential rise with time-scale τ_d.
*Value inferred from the timing residuals in Wong et al. (2001).
⋆Taking $(t_3 - t_0)$ of Palfreyman et al. (2018) as the maximum spin-up duration.
[a]References: (1) Lyne et al. (1992); (2) Wong et al. (2001); (3) Shaw et al. (2018); (4) Dodson et al. (2002); (5) Palfreyman et al. (2018).

Table 2. Summary of results for the mutual friction parameter $\mathcal{B}$ from both the analytic model and the numerical simulations (for which we present the range of limiting values for which the delayed rise is present).

	Crab	Vela
Analytic Model:		
$\mathcal{B}$ in the core:	4×10^{-7}	10^{-3}
$\mathcal{B}$ in the crust:	3×10^{-5}	0.1
Non-linear simulations:		
$\mathcal{B}$ in the core:	$5 \times 10^{-7} - 5 \times 10^{-6}$	$3 \times 10^{-4} - 10^{-3}$
$\mathcal{B}$ in the crust:	$3 \times 10^{-4} - 10^{-5}$	$0.01 - 0.1$

initial spin-up. We approximate I_s as the moment of inertia of a cylindrical shell of constant density ρ, at a radius R_r and thickness Δr, $I_s \approx 4\pi\rho R_r^4 \Delta r$.

If we focus on the delayed component of the rise, i.e. take $\Delta\Omega_o = 2\pi\Delta\nu_d$ (see Table 1) and assume that the associated time-scale τ_d is the time it takes the vortex front to cross Δr, we can combine equations (5) and (6) to estimate $\mathcal{B}$

$$\mathcal{B} = \tilde{\epsilon}\,\frac{I_T}{4\pi\rho R_r^5}\,\frac{\Delta\Omega_d}{\Delta\Omega_M^2\tau_d}\,, \tag{7}$$

3 RESULTS

Let us now use the solution in equation (4) to describe the prolonged spin-up observed in the 2017 Crab glitch (the observations are summarized in Table 1).

We consider two models: a crustal pinning one (denoted with 'k' hereafter) and an outer core pinning one (denoted with 'c' from now on), with $\rho_k = 7 \times 10^{13}$ g cm^{-3} and $\rho_c = 3 \times 10^{14}$ g cm^{-3}, respectively. For the inner crust we take $\tilde{\epsilon} \sim 1$ and for the outer core $\tilde{\epsilon} \sim 0.05$, which is in good agreement with the microphysical models of Chamel (2012) and Potekhin et al. (2013). For both cases we take $R_r = 11$ km and $\Delta\Omega_M \sim -10^{-3}$ rad s^{-1}.[2]

First, using equation (6) for the initial, unresolved step $\Delta\Omega_0 = \Delta\Omega_G$, we find that in the crust, unpinning must be over a region with $\Delta_k r \approx 680$ m. This confirms the expectation that most of the inner crust must be involved in large glitches. For core glitches, this is reduced to $\Delta_c r \approx 150$ m. In the case of the smaller, gradual, spin-up $\Delta\Omega_d$, one has $\Delta_k r \approx 54$ m and $\Delta_c r \approx 12$ m.

From equation (7), we find $\mathcal{B}_k \approx 3 \times 10^{-5}$ for the crust, while for the core model $\mathcal{B}_c \approx 4 \times 10^{-7}$. From equation (2), and setting $\varepsilon_n = -5$ in the crust and $\varepsilon_n = 0$ in the core, we see that both values of $\mathcal{B}$ would give rise times $\tau_r \approx 0.1$ h for the unresolved jump, consistent with the observational limit. However, a value of $\mathcal{B}_c \approx 4 \times 10^{-7}$ is much lower than expected for the core (Graber et al. 2018), especially in the presence of strong vortex-flux tube interactions (Link 2003; Sidery & Alpar 2009; Haskell, Pizzochero & Seveso 2013; Gügercinoğlu & Alpar 2016), which suggests a crust model is more likely. Furthermore, we note that our model predicts a longer time-scale for the delayed rise if the amplitude of that component is larger, as is observed. Applying our method to the other Crab glitches in Table 1, we obtain $\mathcal{B}_k \approx 2 \times 10^{-5}$ and $\mathcal{B}_c \approx 3 \times 10^{-7}$ for the 1989 glitch, while for the 1996 event $\mathcal{B}_k \approx 2 \times 10^{-5}$ and $\mathcal{B}_c \approx 2 \times 10^{-7}$, in good agreement with the results for the 2017 glitch.

Let us now shift our attention to the 2016 Vela glitch. The first thing to note is that the $\mathcal{B}$ values obtained for the Crab would lead to rise times $\tau_r \approx 1$ h for the slower rotating Vela pulsar. This is inconsistent with the upper observational limits of ∼48 s of the 2016 (and 2000) Vela glitch. Furthermore, the initial fast rise would be followed by a delayed rise on a similar time-scale to that of the Crab, contrary to observations.

We will thus assume that the rise, including any delayed component, must be over before 48 s. Given the similarity in sizes, we use the same size ratio for the regions involved in the glitch for the Vela 2016 glitch as that obtained above for the 2017 Crab glitch. Imposing the constraint $\tau_d < 48$ s, we find for Vela $\mathcal{B}_k \gtrsim 0.1$ and $\mathcal{B}_c \gtrsim 10^{-3}$. We note that the latter is a reasonable value of the mutual friction parameter $\mathcal{B}$ for the core, consistent with expectations from electron scattering off vortex cores (Alpar et al. 1984b; Andersson, Sidery & Comer 2006), while the former is an extreme value for kelvon mutual friction in the crust (Epstein & Baym 1992; Jones 1992; Graber et al. 2018). For these values the rapid time-scale for the rise is $\tau_r \approx 0.5$ s, which is close to the shorter time-scales of few seconds reported in Palfreyman et al. (2018) and to the predictions of more accurate Newtonian and general relativistic results (Haskell et al. 2012; Sourie et al. 2017). The results are summarized in Table 2.

[2]This choice of $\Delta\Omega_M^k$ is motivated by the crustal pinning calculations of Seveso et al. (2016), however, in the case of the outer core the vortex-flux tubes interactions and respective pinning strengths are less constrained by the theory and could potentially sustain larger lags.

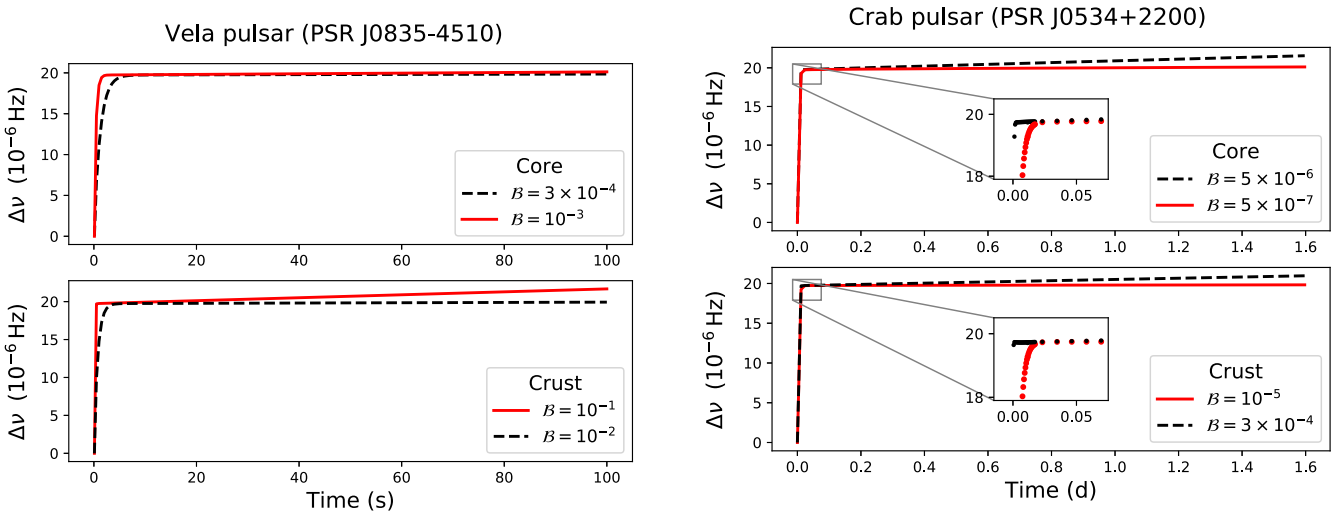

Figure 1. Examples of glitch simulations for the Vela (using $\nu = 11$ Hz) and Crab (using $\nu = 30$ Hz). Both models show a rapid rise which, in each pulsar, is followed by a delayed rise for larger values of $\mathcal{B}$. Overall results for the range of $\mathcal{B}$ in which a delayed rise is present are shown in Table 2, and confirm that a crustal origin for Crab glitches is in line with theoretical estimates for the mutual friction, while a core contribution is favoured for the Vela pulsar.

3.1 Results from non-linear simulations

We complete the analysis above by running numerical simulations of a full model in which, complementary to (1), we provide the following evolution equation for the free vortex fraction γ:

$$\frac{\partial \gamma}{\partial t} = \frac{\mathcal{B}}{2\tilde{\epsilon}} \varpi_0 \Delta\Omega_{\rm M} \frac{\partial \gamma}{\partial \varpi} \ . \tag{8}$$

Physically this corresponds to the free vortex density being advected with the unpinning wave.

As initial conditions we take $\gamma = 1$ in a region Δ_r with $\gamma = 0$ in the rest of the computational domain (of total length L). For numerical convenience we set the ratio $\Delta_r/L = 0.67$, which implies that for our simulations the ratio of moments of inertia involved in the glitch is $I_{\rm s}/I_{\rm T} \approx \Delta_r/L \approx 0.67$. To obtain glitches of a similar size as those observed we thus take an initially constant lag $\Delta\Omega_{\rm M} = -1.82 \times 10^{-4}\,{\rm rad\,s^{-1}}$. We set $\varpi_0 = 11\,{\rm km}$ and $\tilde{\epsilon} = 1$, $\varepsilon_{\rm n} = -5$ for crust models, $\tilde{\epsilon} = 0.05$, $\varepsilon_{\rm n} = 0$ for core models. We evolve the system over the time-scales of interest (∼2 d for the Crab, ∼1 min for the Vela) for a range of $\mathcal{B}$ values, to assess when a delayed rise with amplitude $\Delta\nu_{\rm d} \approx 0.1\,\Delta\nu_{\rm G}$ appears. In general, for low values of $\mathcal{B}$ the delayed rise does not develop on the observed time-scales, while for high values of $\mathcal{B}$ a large delayed component is visible, as the unpinning wave travels through the simulation region.

Fig. 1 presents characteristic examples of the spin evolution. Overall, the results, summarized in Table 2, confirm the qualitative picture from the analytic model, suggesting that the crust model is preferred for Crab and the core model for Vela. Note, however, that if the initial pulse in γ is set to be $\gamma = 1$ over a region Δr and $\gamma = 0.1$ elsewhere (i.e. imperfect pinning, where 10 per cent of vortices are free at all time), the linear term in equation (1) always dominates, and no delayed rise is present. If this is the case in Vela but not the Crab, it would explain the lack of a delayed component in the glitches of the former, but is contrary to theoretical expectations that a higher number of free vortices should be present in the Crab, which is younger and hotter than Vela. Our estimates for $\mathcal{B}$ in the core of Vela are roughly consistent with those of (Graber et al. 2018), but at the lower end of their estimates for the inner crust of Crab. We note, however, that (Graber et al. 2018) calculate $\mathcal{B}$ due to kelvons, which is likely to drive the fast rise. On the other hand, during the slower prolonged rise that we model, weaker phonon excitations are likely to be the dominant source of mutual friction (Jones 1992).

4 DISCUSSION

In this Letter, we present a hydrodynamical glitch model that predicts an initial fast rise, followed by a smaller gradual spin-up, as observed in the 2017 Crab glitch (Shaw et al. 2018) and also two previous glitches (Lyne et al. 1992; Wong et al. 2001). We then compare our model to observations of Crab and Vela glitches, to estimate the value of the mutual friction parameter $\mathcal{B}$, considering two separate cases in which the glitch originates either in the crust or the core of the star.

Our model generally reproduces well the delayed rise observed in several Crab glitches, naturally producing longer time-scales for larger glitch amplitudes, and returning consistent values of $\mathcal{B}$ for all glitches.

We also find that, independently of the model used, the qualitative features of Crab glitches require much smaller values of $\mathcal{B}$. In particular, for core models, we obtain values that are much smaller than what is theoretically expected, while for the crust the results fall in the theoretically predicted range. For the Vela pulsar, on the other hand, larger values are required, which are in line with theoretical estimates for the core but generally at the very upper end of predictions for crustal models.

Theoretically, if we assume that both events originate in the same region of the star it is difficult to justify a larger value of $\mathcal{B}$ in the Vela pulsar. The Vela is older and colder than the Crab pulsar but most mutual friction mechanisms are roughly temperature independent, and even other mechanisms that may be at work, such as coupling of electrons to quasiparticles in vortex cores via interactions the magnetic moment of the neutrons (Bildsten & Epstein 1989), generally become less effective at lower temperatures (see Haskell & Sedrakian 2017, for a review of possible mutual friction mechanisms).

We thus conclude that it is likely that Crab glitches originate in the crust of the star, and Vela glitches in the outer core. This is also supported by the need to consider the core superfluid to explain

the observed activity of the Vela pulsar (Andersson et al. 2012; Chamel 2013; Ho et al. 2015; Newton et al. 2015; Pizzochero et al. 2017), and would justify the striking difference in the glitch size and waiting time distributions of the two pulsars (Melatos et al. 2008).

Future high sensitivity, dense observations of glitches and prompt post-glitch response in other pulsars would allow to confirm whether this interpretation can be validated throughout the pulsar population, and used to explain the general differences between Vela-like pulsars (such as J0537-6910, for which its glitch predictability can be used to plan increased monitoring) and Crab-like pulsars which exhibit a large range in glitch sizes and waiting times. Such differences between pulsars may be due to the combination of effects, such as different masses (leading to different core compositions and pinning strengths), but also different temperatures or spin-down rates.

At the same time, future work on the theoretical front should focus on the vortex-cluster and vortex-flux tube interaction, in order to obtain microphysical constraints on the mutual friction parameters, as are already being developed for pinning forces (Wlazłowski et al. 2016). In conclusion, astrophysical limits on the mutual friction parameters, such as those that we have obtained, can be very powerful if combined with theoretical estimates. Our results come at the right time and provide input on the range of parameters to explore with microscopic models and numerical simulations.

ACKNOWLEDGEMENTS

We acknowledge support from the Polish National Science Centre grant SONATA BIS 2015/18/E/ST9/00577, and the European Union's Horizon 2020 research and innovation programme under grant agreement No. 702713. Partial support comes from The multi-messenger physics and astrophysics of neutron stars, COST Action CA16214.

REFERENCES

Akbal O., Alpar M. A., 2018, MNRAS, 473, 621
Alpar M. A., 1977, ApJ, 213, 527
Alpar M. A., Pines D., Anderson P. W., Shaham J., 1984a, ApJ, 276, 325
Alpar M. A., Langer S. A., Sauls J. A., 1984b, ApJ, 282, 533
Anderson P. W., Itoh N., 1975, Nature, 256, 25
Andersson N., Comer G. L., 2006, Class. Quantum Gravity, 23, 5505
Andersson N., Sidery T., Comer G. L., 2006, MNRAS, 368, 162
Andersson N., Glampedakis K., Ho W. C. G., Espinoza C. M., 2012, Phys. Rev. Lett., 109, 241103
Antonopoulou D., Espinoza C. M., Kuiper L., Andersson N., 2018, MNRAS, 473, 1644
Bildsten L., Epstein R. I., 1989, ApJ, 342, 951
Chamel N., 2012, Phys. Rev. C, 85, 035801
Chamel N., 2013, Phys. Rev. Lett., 110, 011101
Dodson R. G., McCulloch P. M., Lewis D. R., 2002, ApJ, 564, L85
Epstein R. I., Baym G., 1992, ApJ, 387, 276
Espinoza C. M., Lyne A. G., Stappers B. W., Kramer M., 2011, MNRAS, 414, 1679
Graber V., Cumming A., Andersson N., 2018, preprint (arXiv:1804.02706)
Gügercinoğlu E., Alpar M. A., 2016, MNRAS, 462, 1453
Haskell B., 2016, MNRAS, 461, L77
Haskell B., Melatos A., 2015, Int. J. Mod. Phys., 24, 1530008
Haskell B., Sedrakian A., 2017, preprint (arXiv:1709.10340)
Haskell B., Pizzochero P. M., Sidery T., 2012, MNRAS, 420, 658
Haskell B., Pizzochero P. M., Seveso S., 2013, ApJ, 764, L25
Ho W. C. G., Espinoza C. M., Antonopoulou D., Andersson N., 2015, Sci. Adv., 1, e1500578
Hooker J., Newton W. G., Li B.-A., 2015, MNRAS, 449, 3559
Jones P. B., 1992, MNRAS, 257, 501
Khomenko V., Haskell B., 2018, PASA, 35, e020
Larson M. B., Link B., 2002, MNRAS, 333, 613
Link B., 2003, Phys. Rev. Lett., 91, 101101
Link B., Epstein R. I., Lattimer J. M., 1999, Phys. Rev. Lett., 83, 3362
Lyne A. G., Smith F. G., Pritchard R. S., 1992, Nature, 359, 706
Melatos A., Peralta C., Wyithe J. S. B., 2008, ApJ, 672, 1103
Middleditch J., Marshall F. E., Wang Q. D., Gotthelf E. V., Zhang W., 2006, ApJ, 652, 1531
Newton W. G., Berger S., Haskell B., 2015, MNRAS, 454, 4400
Palfreyman J., Dickey J. M., Hotan A., Ellingsen S., van Straten W., 2018, Nature, 556, 219
Pizzochero P. M., 2011, ApJ, 743, L20
Pizzochero P. M., Antonelli M., Haskell B., Seveso S., 2017, Nature Astron., 1, 0134
Potekhin A. Y., Fantina A. F., Chamel N., Pearson J. M., Goriely S., 2013, A&A, 560, A48
Seveso S., Pizzochero P. M., Haskell B., 2012, MNRAS, 427, 1089
Seveso S., Pizzochero P. M., Grill F., Haskell B., 2016, MNRAS, 455, 3952
Shaw B. et al., 2018, MNRAS, 414, 3832
Sidery T., Alpar M. A., 2009, MNRAS, 400, 1859
Sourie A., Chamel N., Novak J., Oertel M., 2017, MNRAS, 464, 4641
Warszawski L., Melatos A., Berloff N. G., 2012, Phys. Rev. B, 85, 104503
Wlazłowski G., Sekizawa K., Magierski P., Bulgac A., Forbes M. M., 2016, Phys. Rev. Lett., 117, 232701
Wong T., Backer D. C., Lyne A., 2001, ApJ, 548, 447
Yu M. et al., 2013, MNRAS, 429, 688

This paper has been typeset from a TEX/LATEX file prepared by the author.

Hydrodynamical instabilities in the superfluid interior of neutron stars with background flows between the components

V. Khomenko, M. Antonelli, and B. Haskell

Nicolaus Copernicus Astronomical Center, Polish Academy of Sciences, ul. Bartycka 18, 00-716 Warsaw, Poland

(Received 25 June 2019; published 2 December 2019)

The interiors of mature neutron stars are expected to host superfluid neutrons that can flow relative to the normal component tracked by electromagnetic emission. Hence, analogously to the hydrodynamic description of terrestrial superfluids like ^{4}He, the system is best described by means of a two-fluid model. We study wave propagation in the crust and core of a neutron star by conducting a local plane-wave analysis of the two-fluid hydrodynamic equations for a homogeneous macroscopic element of nuclear matter. We explicitly account for a background flow between the two components (as would be expected in the presence of pinning of superfluid vortex lines) and the entrainment coupling, and we consider both standard (Hall-Vinen) and isotropic (Gorter-Mellink) forms of the mutual friction. We find that for standard mutual friction there are families of unstable inertial and sound waves both in the case of a counter-flow along the superfluid vortex axis and for counterflow perpendicular to the vortex axis and find that entrainment leads to a quantitative difference between instabilities in the crust and core of the star. For isotropic mutual friction, we find no unstable branches of the dispersion law and speculate that instabilities in a straight vortex array may be linked to glitching behavior, which then ceases until the turbulence has decayed.

DOI: 10.1103/PhysRevD.100.123002

I. INTRODUCTION

Describing the inner structure of a neutron star (NS) requires theoretical methods consistent with astronomical observations. Despite the recent detection of gravitational waves emitted during an NS merger [1], which delivered interesting constraints on the equation of state of matter at high densities [2], direct data from the deep layers of an NS are inaccessible.

To date, most of the signals we receive from NSs consist of electromagnetic radiation emitted by the star, which carries mostly information on the processes in the magnetosphere or outermost, low density, layers. However, in some cases, the electromagnetic spectra allow to constrain the surface temperature controlled by the heat conduction and neutrino emission, which in turn depends on the physics of deep layers, i.e., whether the interior contains superfluid components or not [3]. In fact, neutrons can pair and form a superfluid in the inner crust and core of an NS, with protons also expected to be superconducting in the core (see Haskell and Sedrakian [4] for a recent review). Superfluidity and superconductivity profoundly alter the dynamics of the internal components that can now flow relative to each other with small dissipation for extended periods of time.

In particular, the presence of superfluid matter in the outer core and inner crust of an NS is believed to be connected with glitches, sporadic, and small increments of the rotational frequency of a pulsar [5].

In fact, glitches are generally assumed to be due to the sudden recoupling of the interior superfluid neutrons and the normal crust, which is tracked by the electromagnetic emission [6,7]. Glitches allow for an indirect probe of the NS interior and can be used to obtain constraints on physical parameters of the star [8–12]. The superfluid component, however, also has a strong impact on the spectrum of global oscillations of the NS, as the increase of degrees of freedom leads to an increase in the number of modes [13,14]. Furthermore, the presence of a superfluid may affect the oscillation modes of an NS as also Tkackenko waves in the vortex array could be excited [15,16]. This in turn will have observational consequences, as global modes of oscillation can lead to gravitational wave emission [13,14,17,18] and may be at the heart of the observed quasiperiodic oscillations in the tail of magnetar giant flares [19–21].

The hydrodynamics of coupled superfluid and normal fluid systems plays a key role in the analysis of not only NSs, but also laboratory superfluids. In particular, it is well known that thermal counterflow of the normal fluid with respect to the superfluid can generate turbulence, and that the vortex array will be disrupted by the so-called Donnelly-Glaberson (DG) instability [22]. Many experimental and theoretical studies have recently investigated counterflow turbulence and the link between the motion of the normal fluid and that of the superfluid [23–26]. The instability is a general feature of superfluids with vorticity,

and is thus likely to operate in NS interiors [27,28], as phenomena such as precession and Ekman flow can lead to large scale motions along the rotation axis [29]. The DG instability is not stabilized by the magnetic field and could play an important role in an NS [30].

Very few experiments (see, e.g., Swanson *et al.* [31], Finne *et al.* [32]), however, have dealt with instabilities due to counterflow coupled to rotation, which is a setup reminiscent of the neutron star interior, in which the normal component can rotate at a different rate with respect to the neutron superfluid. A notable exception is represented by the experiment of [33], who considered rotating spherical containers of superfluid He II, that abruptly changed angular velocity, and studied the relaxation of the fluid (see Eysden and Melatos [34] for a recent analysis of the experiment).

To make progress in the neutron star problem, we adopt a hydrodynamical approach similar to that used in the study of superfluid He II, the so-called Hall-Vinen-Bekarevich-Khalatnikov (HVBK) two-fluid model [35,36], and based on the multifluid neutron star hydrodynamics proposed by Andersson and Comer [37]. This allows us to study the dispersion relation of waves propagating in the coupled fluids and investigate not only their spectrum, but also which branches of the dispersion relation may be driven unstable by the counterflow of the superfluid and normal components. Such instabilities may signal the transition to a turbulent state and may both trigger a glitch and affect the response of the fluid after the event. An example of such trigger is the Kelvin-Helmholtz instability on the isotropic-anisotropic interface between the $^1S_0$ and $^3P_2$ neutron superfluids close to the crust-core transition [38]. Another group of instabilities, namely two stream instabilities, may also be related to glitches since the entrainment effect could provide a sufficiently strong coupling for the instability to be astrophysically plausible [39–42]. Instabilities in pinned superfluids have been studied by Link [43,44], who considered a regime in which vortices are pinned either to nuclei in the crust, or to superconducting fluxtubes in the core of the star, with only a small number of them "creeping" out. On a larger scale, the global flow in an NS may also be susceptible to various instabilities in spherical Couette flow [45–47], and such instabilities may also be related to timing noise in radio pulsars [48], and precession of the rotational axis of NSs [49,50].

In the present work, a local three-dimensional plane wave analysis of equations of motion for a multiconstituent fluid [37] is performed. We consider two fluids, the superfluid neutrons and a normal charge neutral fluid that consist of electrons and protons [51]. Dissipative coupling between the fluids is given by mutual friction, while a nondissipative coupling is due the entrainment effect, that accounts for the reduced mobility of neutrons especially in the crust [52,53]. We start from the analysis of Sidery *et al.* [28], who analyzed the oscillations of such a system, assuming the fluids to be locked in the background configuration, and in our calculation also allow for a velocity difference between the constituents in the background, and explicitly account for entrainment. Physically, such a background velocity difference will be built up if vortices are pinned in the crust or core of the star and is crucial for our analysis.

II. TWO-FLUID HYDRODYNAMICS

Our starting point will be the multifluid formalism of [37]. We consider the hydrodynamical equations of motion for two dynamical degrees of freedom, the superfluid neutrons, and a charge neutral fluid consisting of protons and electrons locked together by electromagnetic interactions on timescales shorter than those of interest for our problem. The momentum equations take the form

$$\left(\frac{\partial}{\partial t}+v_{\mathrm{x}}^{j}\nabla_{j}\right)\tilde{p}_{i}^{\mathrm{x}}+\varepsilon_{\mathrm{x}}w_{j}^{\mathrm{yx}}\nabla_{i}v_{\mathrm{x}}^{j}+\nabla_{i}(\Phi_{R}+\tilde{\mu}_{\mathrm{x}}) +2\epsilon_{ijk}\Omega^{j}v_{\mathrm{x}}^{k}=f_{i}^{\mathrm{x}}. \tag{1}$$

Indices x and y label the constituents, and the inequality $\mathrm{x}\neq\mathrm{y}$ is always understood to be true. The proton-electron fluid will be denoted as p (and often referred to as the "proton" fluid, as electrons ensure charge neutrality, but only carry a small fraction of the inertia of the fluid) and superfluid neutrons, labeled as n. Indices i, j, k label the spacial coordinates. Summation over repeated indices is implied (excluding the summation over constituent x and y indices). The velocity of constituent x is v_i^{x} while $w_i^{\mathrm{yx}}=v_i^{\mathrm{y}}-v_i^{\mathrm{x}}$ is the difference between velocities of components. The angular velocity of the star in the background configuration is given by the vector Ω^i, and we have included the centrifugal term in the potential Φ_R, that in spherical coordinates can be written as

$$\Phi_R=\Phi-\frac{1}{2}\Omega^2r^2\sin\theta^2, \tag{2}$$

where Φ is the gravitational potential which is given by the Poisson equation

$$\nabla^2\Phi=4\pi G\sum_{\mathrm{x}}\rho_{\mathrm{x}}. \tag{3}$$

$\tilde{\mu}_{\mathrm{x}}=\mu_{\mathrm{x}}/m_{\mathrm{x}}$ is the chemical potential per unit mass, and ρ_{x} is the density of the x constituent. In the following, we make the approximation $m_{\mathrm{p}}=m_{\mathrm{n}}=m$. Finally, the momentum per unit mass $\tilde{p}_i^{\mathrm{x}}$, which due to entrainment is not aligned with the velocity v_{x}^i, is

$$\tilde{p}_i^{\mathrm{x}}=v_i^{\mathrm{x}}+\varepsilon_{\mathrm{x}}w_i^{\mathrm{yx}}, \tag{4}$$

where ε_{x} is the entrainment coefficient. Assuming that individual species are conserved, the continuity equations are

$$\frac{\partial \rho_{\rm x}}{\partial t} + \nabla_j(\rho_{\rm x} v_{\rm x}^j) = 0. \tag{5}$$

The force $f_i^{\rm x}$ on the right-hand side of Eq. (1) is the vortex mediated mutual friction [35], and it represents an average of individual interactions between vortices and the normal fluid on the subhydrodynamical scale. As such its form depends strongly on the properties of the vortex configuration within the fluid. For straight vortices and laminar flow, vortex mediated mutual friction force takes the form [54]

$$f_i^{\rm x} = \frac{\rho_{\rm n}}{\rho_{\rm x}} n_{\rm v} \mathcal{B}' \epsilon_{ijk} \kappa^j w_{\rm xy}^k + \frac{\rho_{\rm n}}{\rho_{\rm x}} n_{\rm v} \mathcal{B} \epsilon_{ijk} \hat{\kappa}^j \epsilon^{klm} \kappa_l w_m^{\rm xy}, \tag{6}$$

where hats represent unit vectors, and the vector $\kappa^i = \kappa \hat{\Omega}^i$ points along the vortex array, which is colinear with the rotation axis, and $\kappa = h/2m_{\rm n}$ is the quantum of circulation. The vortex density per unit area, $n_{\rm v}$, can be linked to the average large scale vorticity ω^i of the superfluid as

$$\kappa^i n_{\rm v} = \omega^i = \epsilon^{ijk} \nabla_j \tilde{p}_k^{\rm n} + 2\Omega^i, \tag{7}$$

which for two fluids rotating rigidly around a common axis with angular velocities $\Omega_{\rm p}$ and $\Omega_{\rm n}$ reduces to

$$\kappa_i n_{\rm v} = 2\Omega_i^{\rm n} + 2\varepsilon_{\rm n}(\Omega_i^{\rm p} - \Omega_i^{\rm n}). \tag{8}$$

For vanishing entrainment, or if the two fluids corotate, the above expression reduces to the standard Feynman-Onsager relation for rotating superfluids, $\kappa^i n_{\rm v} = 2\Omega_{\rm n}^i$.

The mutual friction parameters $\mathcal{B}$ and $\mathcal{B}'$ in (6) can be expressed in terms of dimensionless drag parameter $\mathcal{R}$ as

$$\mathcal{B} = \frac{\mathcal{R}}{1+\mathcal{R}^2}, \quad \text{and} \quad \mathcal{B}' = \frac{\mathcal{R}^2}{1+\mathcal{R}^2}, \tag{9}$$

where $\mathcal{R}$ encodes the microphysics of the dissipation processes that give rise to mutual friction in the stellar interior.

Theoretical calculations provide values for the drag parameter $\mathcal{R} \approx 10^{-4}$ for electron scattering on the magnetized vortex cores in the NS core [55] and $\mathcal{R} \approx 10^{-10}$ for phonon scattering in the crust [56] (however, see [57] for the discussion of additional dissipation mechanisms in the case of type-I superconductor in the core).

Higher values of $\mathcal{R} \approx 1$ are expected due to Kelvon in the crust [58,59], if vortices are moving rapidly past pinning sites. Using the two-fluid model of Khomenko and Haskell [60], that allows for vortex accumulation in the presence of differential rotation and based on the observational data of glitches in Vela and Crab pulsar, Haskell *et al.* [12] have recently derived values of $\mathcal{B}$ in the ranges $\mathcal{B} \approx 10^{-4}$–$10^{-3}$ for the Vela core and $\mathcal{B} \approx 10^{-5} - 10^{-4}$ for the Crab crust. Similar results have been obtained by [61], who also calculated the density dependence of the Kelvon mutual friction parameter.

In the presence of turbulence, however, the vortex array is disrupted, and a vortex tangle is likely to develop. In this case, the form of the mutual friction in (6) will no longer be appropriate. The form of the mutual friction to be used in the case of a polarized turbulent tangle in a neutron star is highly uncertain [62]; however, in analogy to the cause of homogeneous isotropic turbulence in He-II, we will consider the form proposed by Gorter and Mellink [63]

$$f_{\rm x}^i = -\frac{\rho_{\rm n}}{\rho_{\rm x}} A_{GM} w_{\rm xy}^2 w_{\rm xy}^i, \tag{10}$$

where the parameter A_{GM} has the dimensions of the inverse of a circulation and $w_{\rm xy}^2 = w_{\rm xy}^i w_i^{\rm xy}$. As discussed by [62], this form is essentially phenomenological and its relevance for neutron stars is still unclear. However, it is interesting to use this form of mutual friction as a completely different, physically motivated, alternative to (6), to investigate the effects of fully developed turbulence on the mode structure of the star.

III. PERTURBED EQUATIONS OF MOTION

We begin our analysis by linearizing the equations of motion in a frame rotating with angular velocity $\Omega = \Omega_{\rm p}$. Formally, we expand a generic quantity Q in a neighborhood of a certain position $\mathbf{r}$ as

$$Q(\mathbf{r}, t) = Q_B(\mathbf{r}) + \delta Q(\mathbf{r}, t), \tag{11}$$

where Q_B is the background (time independent) value of the field, and the perturbation is assumed to be such that $|\delta Q| \ll |Q_B|$. With this in mind, the perturbed continuity equation follows from (5) and is

$$\frac{\partial \delta\rho_{\rm x}}{\partial t} + \nabla^j(v_j^{\rm x}\delta\rho_{\rm x} + \rho_{\rm x}\delta v_j^{\rm x}) = 0, \tag{12}$$

while from (1), we obtain

$$\begin{aligned}(\partial_t + v_{\rm x}^j\nabla_j)(\delta v_i^{\rm x}(1-\varepsilon_{\rm x}) + w_i^{\rm yx}\delta\varepsilon_{\rm x} + \varepsilon_{\rm x}\delta v_i^{\rm y}) + \delta v_{\rm x}^j \nabla_j \tilde{p}_i^{\rm x} \\ + \delta(\varepsilon_{\rm x} w_j^{\rm yx}\nabla_i v_{\rm x}^j) + \nabla_i(\delta\tilde{\mu}_{\rm x} + \delta\Phi_R) + 2\epsilon_{ijk}\Omega^j\delta v_{\rm x}^k = \delta f_i^{\rm x},\end{aligned} \tag{13}$$

where $\delta f_i^{\rm x}$ is a perturbed mutual friction contribution. In order to keep our equations tractable, we apply the Cowling approximation, taking $\delta\Phi_R = 0$. Using Eq. (4), we can thus expand (13) to write

$$\begin{aligned}(\partial_t + v_{\rm x}^j\nabla_j)(\delta v_i^{\rm x}(1-\varepsilon_{\rm x}) + \varepsilon_{\rm x}\delta v_i^{\rm y} + w_i^{\rm yx}\delta\varepsilon_{\rm x}) + \delta v_{\rm x}^j\nabla_j v_i^{\rm x} \\ + \varepsilon_{\rm x}\delta v_{\rm x}^j\nabla_j w_i^{\rm yx} + \varepsilon_{\rm x}(\delta w_j^{\rm yx}\nabla_i v_{\rm x}^j + w_j^{\rm yx}\nabla_i\delta v_{\rm x}^j) + \delta\varepsilon_{\rm x} w_j^{\rm yx}\nabla_i v_{\rm x}^j \\ + \nabla_i\delta\tilde{\mu}_{\rm x} + 2\epsilon_{ijk}\Omega^j\delta v_x^k = \delta f_i^x,\end{aligned} \tag{14}$$

where

$$\delta w_i^{xy} = \delta v_i^x - \delta v_i^y. \tag{15}$$

A. Thermodynamical relations

As it is clear from the form of the perturbation equations in the previous section, to compute the effect of a velocity perturbation we need to calculate perturbations of the chemical potential and of the entrainment. For a charge neutral two-fluid system, it is known that a complete thermodynamic description in the zero temperature limit can be achieved by considering the two densities ρ_x, the squared velocity lag between the two species w_{yx}^2 and the related intensive variables, namely the two chemical potentials per unit mass $\tilde{\mu}_x$ and a dimensionless parameter α which regulates the strength of the conservative entrainment coupling between the two species [52]. In particular, the first law of thermodynamics can be expressed as [54,64]

$$dE = \tilde{\mu}_x d\rho_x + \tilde{\mu}_y d\rho_y + \alpha dw_{yx}^2, \tag{16}$$

where E is the energy density of the fluid mixture, while the intensive variables are given by

$$\tilde{\mu}_x = \left.\frac{\partial E}{\partial \rho_x}\right|_{\rho_y w_{yx}^2} \quad \text{and} \quad \alpha = \left.\frac{\partial E}{\partial w_{yx}^2}\right|_{\rho_x \rho_y}. \tag{17}$$

The parameter α has the dimensions of a mass density and is related to the usual dimensionless entrainment parameters ε_x via [52,65]

$$\varepsilon_x = \frac{2\alpha}{\rho_x}. \tag{18}$$

Therefore, the variation $\delta\varepsilon_x$ is related to the variations of the more basic thermodynamic quantities α and $\tilde{\mu}_x$ as

$$\delta\varepsilon_x = \frac{2\delta\alpha}{\rho_x} - \frac{\varepsilon_x \delta\rho_x}{\rho_x}. \tag{19}$$

While for the chemical potential, we need to calculate

$$\delta\tilde{\mu}_x = \frac{\partial\tilde{\mu}_x}{\partial\rho_x}\delta\rho_x + \frac{\partial\tilde{\mu}_x}{\partial\rho_y}\delta\rho_y + \frac{\partial\tilde{\mu}_x}{\partial w_{yx}^2}\delta(w_{yx}^2). \tag{20}$$

The derivatives of chemical potential with respect to the squared background velocity may be computed using the first law of thermodynamics in (16), which leads to

$$\frac{\partial\tilde{\mu}_x}{\partial w_{yx}^2} = \frac{\partial^2 E}{\partial w_{yx}^2 \partial\rho_x} = \frac{\partial}{\partial\rho_x}\left(\frac{\partial E}{\partial w_{yx}^2}\right) = \frac{\partial\alpha}{\partial\rho_x}, \tag{21}$$

which, from (18) gives

$$\frac{\partial\tilde{\mu}_x}{\partial w_{yx}^2} = \frac{1}{2}\varepsilon_x + \frac{1}{2}\rho_x\frac{\partial\varepsilon_x}{\partial\rho_x}. \tag{22}$$

We are now ready to calculate perturbations of the entrainment and chemical potential. To do this, we introduce the sound velocities c_x, the chemical couplings C_x [66], and two additional parameters related to the dependence on the lag of α and the chemical potentials,

$$\begin{aligned} c_x^2 &= \rho_x\frac{\partial\tilde{\mu}_x}{\partial\rho_x} \\ C_x &= \rho_y\frac{\partial\tilde{\mu}_x}{\partial\rho_y} = \rho_y\frac{\partial\tilde{\mu}_y}{\partial\rho_x} \\ A_x &= \frac{4}{\rho_x}\frac{\partial\alpha}{\partial w_{np}^2} \\ \alpha_x &= 2\frac{\partial\alpha}{\partial\rho_x} = 2\frac{\partial\tilde{\mu}_x}{\partial w_{np}^2} = \varepsilon_x + \rho_x\frac{\partial\varepsilon_x}{\partial\rho_x}. \end{aligned} \tag{23}$$

Note that our definition of c_x^2 coincides with the one used by [28]. In our more general analysis, we let the entrainment vary according to the thermodynamic relations, which forces us to introduce also A_x and α_x, at least at this formal level. There are no estimates in the literature for the parameters A_x in a neutron star, so in the following we will neglect it and set $A_x = 0$ in practical examples [67]. The parameter C_x is also highly uncertain and generally computed from phenomenological models [39], while for α_x one can obtain an estimate in the inner crust, shown in Fig. 1, by assuming that the ratio between the densities of the two species is frozen at its chemical equilibrium value. In this case, one has that

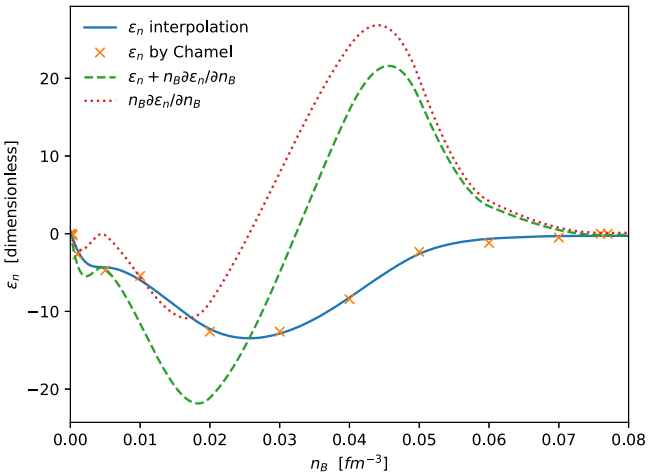

FIG. 1. Estimate of the quantity α_x as a function of the total baryon number density n_B in the inner crust of a neutron star. We interpolate the orange crosses, that indicate the entrainment parameters ε_x in the inner crust calculated by Chamel [68]. The green dashed line is a rough estimate of α_x, the red dotted line quantifies the absolute error that arises by considering $\alpha_x \approx \varepsilon_x$, according to Eq. (24).

$$\varepsilon_{\rm x}+\rho_{\rm x}\frac{\partial\varepsilon_{\rm x}}{\partial\rho_{\rm x}}\approx\varepsilon_{\rm x}+n_B\frac{\partial\varepsilon_{\rm x}}{\partial n_B}, \tag{24}$$

where n_B represents the total baryon number density. This rough argument gives a plausibility interval for the unknown values of α.

Thanks to the fact that $\delta w_{\rm xy}^2=2(v_i^{\rm x}-v_i^{\rm y})(\delta v_{\rm x}^i-\delta v_{\rm y}^i)$, the variation of the chemical potentials can be conveniently written as

$$\begin{aligned}\delta\tilde{\mu}_{\rm x}&=\frac{\partial\tilde{\mu}_{\rm x}}{\partial\rho_{\rm x}}\delta\rho_{\rm x}+\frac{\partial\tilde{\mu}_{\rm x}}{\partial\rho_{\rm y}}\delta\rho_{\rm y}+\frac{\partial\tilde{\mu}_{\rm x}}{\partial w_{\rm yx}^2}\delta w_{\rm yx}^2\\&=c_{\rm x}^2\frac{\delta\rho_{\rm x}}{\rho_{\rm x}}+C_{\rm x}\frac{\delta\rho_{\rm y}}{\rho_{\rm y}}+\alpha_{\rm x}w_i^{\rm yx}\delta w_{\rm yx}^i.\end{aligned} \tag{25}$$

Following the same procedure, we can write for the entrainment

$$\begin{aligned}\delta\alpha&=\frac{\partial\alpha}{\partial\rho_{\rm x}}\delta\rho_{\rm x}+\frac{\partial\alpha}{\partial\rho_{\rm y}}\delta\rho_{\rm y}+\frac{\partial\alpha}{\partial w_{\rm yx}^2}\delta w_{\rm yx}^2\\&=\frac{\alpha_{\rm x}\rho_{\rm x}}{2}\frac{\delta\rho_{\rm x}}{\rho_{\rm x}}+\frac{\alpha_{\rm y}\rho_{\rm y}}{2}\frac{\delta\rho_{\rm y}}{\rho_{\rm y}}+\frac{A_{\rm x}\rho_{\rm x}}{2}w_i^{\rm yx}\delta w_{\rm yx}^i.\end{aligned} \tag{26}$$

which, combined with Eqs. (25) and (26) with (19), leads to

$$\delta\varepsilon_{\rm x}=A_{\rm x}w_{\rm yx}^i\delta w_i^{\rm yx}+(\alpha_{\rm x}-\varepsilon_{\rm x})\frac{\delta\rho_{\rm x}}{\rho_{\rm x}}+\alpha_{\rm y}\frac{\delta\rho_{\rm y}}{\rho_{\rm x}}. \tag{27}$$

B. Perturbing the mutual friction

The next step is to perturb the mutual friction. Let us start by considering the anisotropic form valid for a straight vortex array, given in (6). In this case, it is

$$\begin{aligned}\delta f_i^{\rm x}=&\,\delta\left(\frac{\rho_{\rm n}}{\rho_{\rm x}}\right)[n_{\rm v}\kappa^j\mathcal{B}'\epsilon_{ijk}w_{\rm xy}^k+n_{\rm v}\kappa_l\mathcal{B}\epsilon_{ijk}\hat{\kappa}^j\epsilon^{klm}w_m^{\rm xy}]\\&+\frac{\rho_{\rm n}}{\rho_{\rm x}}n_{\rm v}\kappa^j\mathcal{B}'\varepsilon_{ijk}\delta w_{\rm xy}^k+\frac{\rho_{\rm n}}{\rho_{\rm x}}n_{\rm v}\kappa_l\mathcal{B}\varepsilon_{ijk}\hat{\kappa}^j\varepsilon^{klm}\delta w_m^{\rm xy}\\&+\frac{\rho_{\rm n}}{\rho_{\rm x}}\delta(n_{\rm v}\kappa^j)\mathcal{B}'\varepsilon_{ijk}w_{\rm xy}^k+\frac{\rho_{\rm n}}{\rho_{\rm x}}\delta(n_{\rm v}\kappa_l)\mathcal{B}\varepsilon_{ijk}\hat{\kappa}^j\epsilon^{klm}w_m^{\rm xy}\\&+\frac{\rho_{\rm n}}{\rho_{\rm x}}n_{\rm v}\kappa_l\mathcal{B}\varepsilon_{ijk}\delta(\hat{\kappa}^j)\epsilon^{klm}w_m^{\rm xy},\end{aligned} \tag{28}$$

where we have assumed that $\delta\mathcal{B}=\delta\mathcal{B}'=0$. In principle, one could vary also these quantities, but given the large uncertainties on these coefficients, and to simplify our analysis, we choose to ignore their perturbations. In order to discuss the terms in a more tractable form, and keep track of their physical origin, we separate the expression above in the following way:

$$\delta f_i^{\rm x}=(\delta f_i)_{\rm sound}+(\delta f_i)_w+(\delta f_i)_{n_{\rm v}\kappa}+(\delta f_i)_{\hat{\kappa}}. \tag{29}$$

The first term $(\delta f_i)_{\rm sound}$ connects sound waves and the mutual friction and takes the form

$$\begin{aligned}(\delta f_i)_{\rm sound}=&\left(\frac{\delta\rho_{\rm n}}{\rho_{\rm x}}-\frac{\rho_{\rm n}}{\rho_{\rm x}^2}\delta\rho_{\rm x}\right)(n_{\rm v}\kappa^j\mathcal{B}'\epsilon_{ijk}w_{\rm xy}^k\\&+n_{\rm v}\kappa_l\mathcal{B}\epsilon_{ijk}\hat{\kappa}^j\epsilon^{klm}w_m^{\rm xy}).\end{aligned} \tag{30}$$

The term, containing the perturbations of the background velocity, which would exist also if the fluids corotate in the background, is

$$(\delta f_i)_w=\frac{\rho_{\rm n}}{\rho_{\rm x}}n_{\rm v}(\kappa^j\mathcal{B}'\epsilon_{ijk}\delta w_{\rm xy}^k+\kappa_l\mathcal{B}\epsilon_{ijk}\hat{\kappa}^j\epsilon^{klm}\delta w_m^{\rm xy}). \tag{31}$$

The final two terms $(\delta f_i)_{n_{\rm v}\kappa}$ and $(\delta f_i)_{\hat{\kappa}}$ depend on variations of the vorticity, both in magnitude and direction, and to calculate them we need to perturb the vorticity $\omega^i=\kappa^i n_{\rm v}$, so that

$$\delta(\kappa^i n_{\rm v})=\delta\omega^i=\epsilon^{ijk}\nabla_j\delta\tilde{p}_k^{\rm n}, \tag{32}$$

which using

$$\delta\tilde{p}_{\rm x}^i=(1-\varepsilon_{\rm x})\delta v_{\rm x}^i+\varepsilon_{\rm x}\delta v_{\rm y}^i+w_{\rm yx}^i\delta\varepsilon_{\rm x} \tag{33}$$

gives

$$\begin{aligned}\delta\omega^i=&(1-\varepsilon_{\rm n})\epsilon^{ijk}\nabla_j\delta v_k^{\rm n}+\varepsilon_{\rm n}\epsilon^{ijk}\nabla_j\delta v_k^{\rm p}\\&+\epsilon^{ijk}\nabla_j(\delta\varepsilon_{\rm n})w_k^{\rm pn}.\end{aligned} \tag{34}$$

We also need to perturb the vorticity unit vector $\hat{\kappa}^i=\hat{\omega}^i$, which can be done readily in terms of a projection operator $\perp$ that projects orthogonally to the vortex lines,

$$\delta\hat{\kappa}^i=\delta\hat{\omega}^i=\frac{1}{|\boldsymbol{\omega}|}\perp_a^i\delta\omega^a=\frac{1}{|\boldsymbol{\omega}|}(\delta_a^i-\hat{\omega}^i\hat{\omega}_a)\delta\omega^a. \tag{35}$$

We can thus write

$$\begin{aligned}(\delta f_i)_{n_{\rm v}\kappa}=&-\frac{\rho_{\rm n}}{\rho_{\rm x}}\mathcal{B}'(w_{\rm xy}^k\nabla_k\delta\tilde{p}_{\rm n}^i-w_{\rm xy}^k\nabla_i\delta\tilde{p}_k^{\rm n})\\&+\frac{\rho_{\rm n}}{\rho_{\rm x}}\mathcal{B}(\hat{\kappa}^m w_m^{\rm xy}\epsilon_{ith}\nabla^t\delta\tilde{p}_{\rm n}^h-w_i^{\rm xy}\hat{\kappa}^l\epsilon_{lth}\nabla^t\delta\tilde{p}_{\rm n}^h)\end{aligned} \tag{36}$$

and

$$(\delta f_i)_{\hat{\kappa}}=\frac{\rho_{\rm n}}{\rho_{\rm x}}\mathcal{B}\hat{\kappa}_i(w_{\rm xy}^s\epsilon_{slm}\nabla^l\delta\tilde{p}_{\rm n}^m-w_q^{\rm xy}\hat{\kappa}^q\epsilon_{tlm}\hat{\kappa}^t\nabla^l\delta\tilde{p}_{\rm n}^m), \tag{37}$$

which, together with (33), completes our calculation of the perturbed mutual friction. Before moving on, let us remark that we could have obtained our expression directly in terms of the perturbed vorticity $\delta\omega^i$, by noting that the term $\epsilon_{ijk}\hat{\omega}^j\epsilon^{klm}\omega_l w_m^{\rm yx}$ in the expression in (6) for the mutual

friction, can be written in terms of the projection operator in (35) as

$$\epsilon_{ijk}\hat{\omega}^j\epsilon^{klm}\omega_l w_m^{\mathrm{yx}} = -|\boldsymbol{\omega}|\perp_i^j w_j^{\mathrm{yx}} \tag{38}$$

and that

$$-\delta(|\boldsymbol{\omega}|\perp_i^j w_j^{\mathrm{yx}}) = \delta\omega_i(\hat{\omega}^j w_j^{\mathrm{yx}}) + \hat{\omega}_i(w_{\mathrm{yx}}^j\delta\omega_j) + -(\hat{\omega}^j\delta\omega_j)(\perp_i^k w_k^{\mathrm{yx}}) - |\boldsymbol{\omega}|(\perp_i^k \delta w_k^{\mathrm{yx}}). \tag{39}$$

We consider also perturbations of the isotropic mutual friction force in (10), proposed for the case in which we have fully developed turbulence and an isotropic vortex tangle. In this case, the perturbations of the vorticity play no role and from Eq. (10), we have

$$\delta f_i^{\mathrm{x}(GM)} = -\frac{\rho_{\mathrm{n}}}{\rho_{\mathrm{x}}}A_{GM}\{|\mathbf{w}_{\mathrm{xy}}|^2\delta w_i^{\mathrm{xy}} + 2(w_{\mathrm{xy}}^j\delta w_j^{\mathrm{xy}})w_i{}^{\mathrm{xy}}\} + -\delta\left(\frac{\rho_{\mathrm{n}}}{\rho_{\mathrm{x}}}\right)A_{GM}|\mathbf{w}_{\mathrm{xy}}|^2 w_{\mathrm{xy}}^i. \tag{40}$$

IV. PLANE WAVE ANALYSIS

We are now ready to derive the dispersion relation for waves propagating in a neighborhood of the position $\mathbf{r}$ inside the star. To do so, we use a plane wave ansatz into the linearized hydrodynamical equations derived in the previous section. Let $\mathbf{r}+\mathbf{x}$ be a vector in the neighborhood of $\mathbf{r}$, so that we can write

$$Q(\mathbf{r}+\mathbf{x},t) = Q_B(\mathbf{r}) + \delta Q_{\mathbf{r}}(\mathbf{x},t), \tag{41}$$

with

$$\delta Q_{\mathbf{r}} = \bar{Q}e^{i(k_j x^j-\omega t)}. \tag{42}$$

We assume that $|\mathbf{x}| \ll |\mathbf{r}|$ and $R^{-1} \ll |\mathbf{k}|$, so that all gradients of background quantities (that vary on length scales comparable to the stellar radius R) are ignored in our perturbation equations. We use a local cartesian coordinate system, as sketched in Fig. 2, which is taken to be corotating with the normal component, such that $\Omega = \Omega_{\mathrm{p}}$ and $v_{\mathrm{p}} = 0$ in the following. This naturally implies that

$$w_{\mathrm{np}}^i = v_{\mathrm{n}}^i. \tag{43}$$

Each perturbed quantity δQ can be expressed in terms of the two fields δv_{n}^i and δv_{p}^i by means of the continuity equations and of the thermodynamic relations and it will be convenient to express the amplitude $\bar{Q}$ as

$$\bar{Q} = Q_a^{\mathrm{n}}\bar{v}_{\mathrm{n}}^a + Q_a^{\mathrm{p}}\bar{v}_{\mathrm{p}}^a. \tag{44}$$

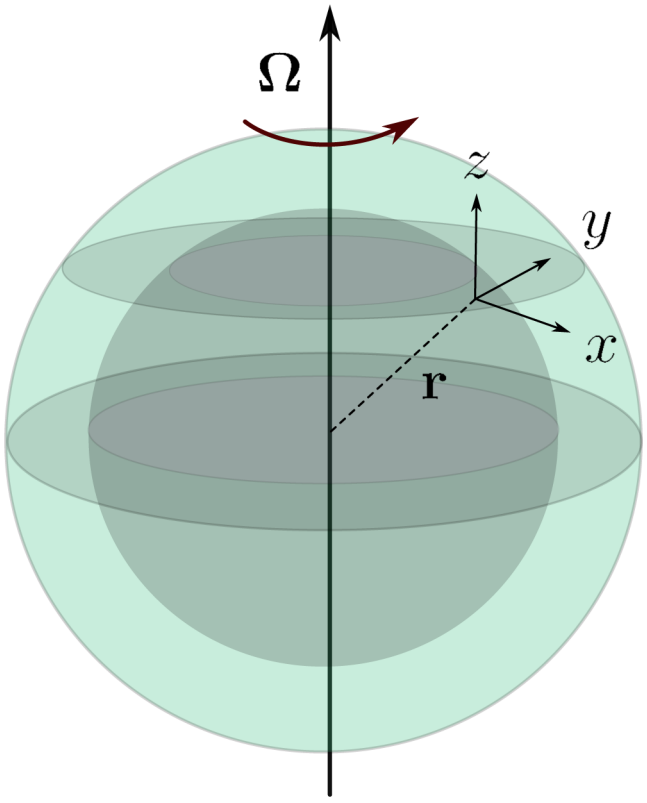

FIG. 2. Sketch of the geometrical definitions used: the vector $\mathbf{r}$ indicates the central position of a small sample of matter inside the star, whereas $\mathbf{r}+\mathbf{x}$ identifies the points in a neighborhood of $\mathbf{r}$. The local Cartesian system of coordinates is chosen to be right-handed in such a way that the z-axis is parallel to the direction identified by $\boldsymbol{\Omega}$, the x-axis defines the direction of the cylindrical radius, and the y-axis is locally parallel to the azimuthal direction. In this way, the coordinates x, y and z identify the position $\mathbf{x}$ introduced in Eq. (41).

Following this procedure, the perturbed version of the Euler-like equations (1) can be used to define a linear system of six equations for the six independent amplitudes $\bar{v}_{\mathrm{x}}^i$ which has the form

$$\sum_{\mathrm{y}'=\mathrm{n,p}} M_{ij}^{\mathrm{xy}'}\bar{v}_{\mathrm{y}'}^j. \tag{45}$$

The only way to have nontrivial solutions of the above equation is to impose that $\det(M) = 0$. The determinant of (45) is in general a high degree polynomial in the components of the wave vector $\mathbf{k}$ and of the frequency ω and requires a numerical analysis. Particular cases that can be studied analytically will, however, be presented in the following sections.

To calculate the components of the matrix in (45), first of all we insert the plane wave ansatz in the continuity equation (12) to obtain

$$\bar{\rho}_{\rm x} = \rho_i^{\rm xx}\bar{v}_{\rm x}^i, \quad \text{where } \rho_i^{\rm xx} = \frac{\rho_{\rm x}k_i}{\omega - k_i v_{\rm x}^i}. \tag{46}$$

We also need the plane wave perturbations of the chemical potential and entrainment, which from (25) and (27) are

$$\bar{\mu}_{\rm x} = \left[c_{\rm x}^2\frac{\rho_i^{\rm xx}}{\rho_{\rm x}} + \alpha_{\rm x}v_{\rm xy}^i\right]\bar{v}_{\rm x}^i + \left[C_{\rm x}\frac{\rho_i^{\rm yy}}{\rho_{\rm y}} - \alpha_{\rm x}v_{\rm xy}^i\right]\bar{v}_i^{\rm y} \tag{47}$$

and

$$\bar{\varepsilon}_{\rm x} = \left[(\alpha_{\rm x}-\varepsilon_{\rm x})\frac{\rho_i^{\rm xx}}{\rho_{\rm x}} + A_{\rm x}v_{\rm xy}^i\right]\bar{v}_i^{\rm x} + \left[\alpha_{\rm y}\frac{\rho_i^{\rm yy}}{\rho_{\rm x}} - A_{\rm x}v_{\rm xy}^i\right]\bar{v}_i^{\rm y}. \tag{48}$$

With the above expressions at hand, we can now compute the plane wave perturbations of the Euler equations in (14). The full result is complex, but a procedure to obtain all the variations in the presence of a background lag and with no approximations is given in Appendix. It is, however, instructive to study the case in which we neglect perturbations of the entrainment and set $\delta\varepsilon_{\rm x} = 0$ and also neglect terms involving $\partial\varepsilon_{\rm x}/\partial\rho_{\rm x}$, so that one has $\alpha_{\rm x} \approx \varepsilon_{\rm x}$ in (47). In this case, the Euler equations can be written as

$$i(k_j v_{\rm x}^j - \omega)[\bar{v}_i^{\rm x}(1-\varepsilon_{\rm x}) + \varepsilon_{\rm x}\bar{v}_i^{\rm y}] + 2\epsilon_{ijk}\Omega^j\bar{v}_x^k - ik_i\left(c_{\rm x}^2\frac{k_j\bar{v}_x^j}{k_j v_{\rm x}^j - i\omega} + C_{\rm y}\frac{k_j\bar{v}_y^j}{k_j v_{\rm y}^j - i\omega} - \varepsilon_{\rm x}\bar{v}_y^j w_j^{\rm yx}\right) = \delta f_i, \tag{49}$$

where defining $\bar{p}_{\rm n}^k = \bar{v}_{\rm n}^k + \varepsilon_{\rm n}\bar{w}_{\rm pn}^k$, we have

$$\begin{aligned}\delta f_i = {} & \left(\frac{\bar{\rho}_{\rm n}}{\rho_{\rm x}} - \frac{\rho_{\rm n}}{\rho_{\rm x}^2}\bar{\rho}_{\rm x}\right)n_{\rm v}\kappa^j\mathcal{B}'\epsilon_{ijk}w_{\rm xy}^k + \left(\frac{\bar{\rho}_{\rm n}}{\rho_{\rm x}} - \frac{\rho_{\rm n}}{\rho_{\rm x}^2}\bar{\rho}_{\rm x}\right)n_{\rm v}\kappa_l\mathcal{B}\epsilon_{ijk}\hat{\kappa}^j\epsilon^{klm}w_m^{\rm xy} \\ & + \frac{\rho_{\rm n}}{\rho_{\rm x}}n_{\rm v}\kappa^j\mathcal{B}'\epsilon_{ijk}\bar{w}_{\rm xy}^k + \frac{\rho_{\rm n}}{\rho_{\rm x}}n_{\rm v}\kappa_l\mathcal{B}\epsilon_{ijk}\hat{\kappa}^j\epsilon^{klm}\bar{w}_m^{\rm xy} - \frac{\rho_{\rm n}}{\rho_{\rm x}}\mathcal{B}'(iw_{\rm xy}^k k_k\bar{p}_i^{\rm n} - iw_{\rm xy}^k k_i\bar{p}_k^{\rm n}) \\ & + \frac{\rho_{\rm n}}{\rho_{\rm x}}\mathcal{B}(i\hat{\kappa}^m w_m^{\rm xy}\epsilon_{ith}k^t\bar{p}_n^h - iw_i^{\rm xy}\hat{\kappa}^l\epsilon_{lth}k^t\bar{p}_{\rm n}^h) + \frac{\rho_{\rm n}}{\rho_{\rm x}}\mathcal{B}\delta_i^z(iw_{\rm xy}^s\epsilon_{slm}k^l\bar{p}_{\rm n}^m - iw_z^{\rm xy}\epsilon_{zlm}k^l\bar{p}_{\rm n}^m).\end{aligned} \tag{50}$$

V. WAVES IN THE ABSENCE OF MUTUAL FRICTION

In this section, we consider some simple examples where progress can be made analytically, before moving on to the numerical results for the full set of equations. In particular we will first consider sound waves and inertial waves in the limit of vanishing mutual friction, and show how mutual friction can damp or drive some of the modes instable. The approximations will be outlined for each case as we proceed.

A. Sound waves

Let us begin by considering pure sound waves. If we set $\Omega = \varepsilon_{\rm x} = w_{\rm np} = v_{\rm n} = 0$ in (49) and (50), the dispersion relation follows from

$$\omega^2(c_{\rm p}^2k^2 - \omega^2)(c_{\rm n}^2k^2 - \omega^2) = 0. \tag{51}$$

Here and in the following calculations we will not consider the stable and trivial solutions. Using the dispersion relation, we recover two branches of sound waves, one for each fluid

$$\omega = \pm kc_{\rm n} \tag{52}$$

$$\omega = \pm kc_{\rm p}. \tag{53}$$

Including a background flow, still with $\Omega = \varepsilon_{\rm x} = 0$ does not couple the fluids, and simply introduces a correction, so that the nontrivial branches of the dispersion relation are

$$\omega = \pm kc_{\rm n} + (v_i^{\rm n}k^i) \tag{54}$$

$$\omega = \pm kc_{\rm p}. \tag{55}$$

1. Chemical coupling and entrainment

We now move on to considering the chemical coupling between the two fluids in the regime in which $w_{\rm np} = v_{\rm n} = 0$ and $\Omega = 0$. In this case, the dispersion relation follows from

$$\omega^4\xi - \omega^2k^2(C_\varepsilon + c_\varepsilon^2) + k^4(c_{\rm n}^2c_{\rm p}^2 - C_nC_p) = 0, \tag{56}$$

where we have defined

$$C_\varepsilon = C_{\rm n}\varepsilon_{\rm p} + C_{\rm p}\varepsilon_{\rm p} = 4\alpha\frac{\partial^2E}{\partial\rho_n\partial\rho_{\rm p}} \tag{57}$$

and

$$c_\varepsilon^2 = (1-\varepsilon_{\rm n})c_{\rm p}^2 + (1-\varepsilon_{\rm p})c_{\rm n}^2, \tag{58}$$

as well as the dimensionless parameter

$$\xi = 1 - \varepsilon_{\rm n} - \varepsilon_{\rm p}. \tag{59}$$

The roots of (56) are organized in four branches that have the form

$$\omega = \pm k c_1 \qquad \omega = \pm k c_2, \tag{60}$$

where the constants c_1 and c_2 are two velocities for entrainment-coupled sound waves

$$c_1^2 = \frac{c_\varepsilon^2 + C_\varepsilon + \Delta}{2\xi}$$
$$c_2^2 = \frac{c_\varepsilon^2 + C_\varepsilon - \Delta}{2\xi}, \tag{61}$$

with

$$\Delta = \sqrt{(c_\varepsilon^2 + C_\varepsilon)^2 - 4\xi(c_{\rm n}^2 c_{\rm p}^2 - C_{\rm n} C_{\rm p})}. \tag{62}$$

It is immediate to see that, in the limit of no entrainment and no chemical coupling, c_1 and c_2 are exactly equal to c_n and c_p of pure one-component sound waves. To grasp the physical effect of chemical coupling, we furthermore require that $c_{\rm x}^2 \gg C_{\rm x}, C_{\rm y}$. In this limit, it is useful to define Δ_0 as the limit of Δ when $C_{\rm x} = 0$,

$$\Delta_0 = \sqrt{c_\varepsilon^2 - 4\xi c_{\rm n}^2 c_{\rm p}^2}, \tag{63}$$

so that the limit of weak chemical coupling can be equally seen as $C_x/\Delta_0 \ll 1$. In this case, the velocities in (61) can be expanded up to the second order in the chemical couplings as

$$c_{1,2}^2 = \frac{c_\varepsilon^2 + C_\varepsilon \pm \Delta_0}{2\xi}\left(1 \pm \frac{C_\varepsilon}{\Delta_0}\right) + \tag{64}$$

$$\pm \frac{C_{\rm n} C_{\rm p}}{\Delta_0^2}\frac{c_\varepsilon^4 - 4\xi c_{\rm n}^2 c_{\rm p}^2}{\Delta_0} \mp \frac{C_\varepsilon^2}{\Delta_0^2}\frac{c_{\rm n}^2 c_{\rm p}^2}{\Delta_0} + O(C_{\rm x}^4). \tag{65}$$

In the limit of $\varepsilon_{\rm n} = \varepsilon_{\rm p}$, and using the relation $C_{\rm p} = \frac{\rho_{\rm p}}{\rho_{\rm n}} C_{\rm n}$, we recover the result [28]

$$\omega = \pm k c_{\rm n}\left[1 + \frac{\rho_{\rm p}}{2\rho_{\rm n}}\frac{C_{\rm n}^2}{c_{\rm n}^2(c_{\rm n}^2 - c_{\rm p}^2)}\right] \tag{66}$$

$$\omega = \pm k c_{\rm p}\left[1 + \frac{\rho_{\rm p}}{2\rho_{\rm n}}\frac{C_{\rm n}^2}{c_{\rm p}^2(c_{\rm p}^2 - c_{\rm n}^2)}\right]. \tag{67}$$

However, retaining the entrainment terms, the lowest order correction to the dispersion relation comes the term that is linear in C_ε: when entrainment is considered, the effect of the chemical coupling on sound waves is enhanced. Note that this result is independent of the assumption $\delta\varepsilon_{\rm x} = 0$ and remains the same also in the more general case in which perturbations of the entrainment are considered.

2. Including rotation

We now consider the effect of rotation on the sound waves, in the limit of no chemical coupling, i.e., we take $C_{\rm p} = C_{\rm n} = w_{\rm np} = v_{\rm n} = 0$ in the background. In this case, the dispersion relation is still too complex to solve for a general case. However, if we consider sound waves with a dispersion relation of the form $\omega \sim c_{\rm x} k$, we expect that $\omega \gg \Omega$ even for the smallest possible k, which is of the order of the inverse of the stellar radius R^{-1} (i.e., the sound velocity in nuclear matter is such that $c_{\rm x} \gg \Omega R$). Therefore, it is a very good approximation to expand the two branches of $\omega^2(k)$ to the lowest order in Ω,

$$\omega^2(k) = k^2 c_{1,2}^2 + f_{1,2}\Omega^2 + O(\Omega^4), \tag{68}$$

where

$$c_{1,2}^2 = \frac{c_\varepsilon^2 \pm \Delta_0}{2\xi} \qquad \Delta_0 = \sqrt{c_\varepsilon^4 - 4\xi c_{\rm n}^2 c_{\rm p}^2}, \tag{69}$$

where c_1 corresponds to the upper sign choice. The quantities f_1 and f_2 are

$$f_{1,2} = \frac{2}{\xi^2 \Delta_0}[(\xi^2 + 1)\Delta_0 \mp 2(c_n^2 + c_p^2)(\xi^2 + \xi)\sin^2(\theta) + \tag{70}$$

$$\mp c_\varepsilon^2(\xi^2 + \xi + 1)\cos(2\theta) \pm c_\varepsilon^2 \xi], \tag{71}$$

where f_1 corresponds to the upper sign choice and θ is the angle between $\mathbf{\Omega}$ and $\mathbf{k}$. Finally, combining the above expressions, we find that the correction to the four branches of the dispersion relation for sound waves produced by the Coriolis force is

$$\omega(k) = \pm\left(c_{1,2} k + \frac{f_{1,2}\Omega^2}{2c_{1,2}k}\right), \tag{72}$$

which, neglecting entrainment ($\varepsilon_{\rm n} = \varepsilon_{\rm p} = 0$) reduces to [28]

$$\omega \approx c_{\rm n} k\left[1 + \frac{2\Omega^2}{c_{\rm n}^2 k^2}(\sin\theta)^2\right] \tag{73}$$

$$\omega \approx c_{\rm p} k\left[1 + \frac{2\Omega^2}{c_{\rm p}^2 k^2}(\sin\theta)^2\right]. \tag{74}$$

B. Inertial waves

We now continue to focus on the effect of rotation, but search for solutions that are inertial waves, for which the dispersion relation is not linear in k. If we set

$c_n = c_p = C_n = C_p$, we find, as expected, families of inertial modes such that

$$\omega = \pm 2\Omega\cos\theta \tag{75}$$

$$\omega = \pm\frac{2\Omega\cos\theta}{(1-\varepsilon_n-\varepsilon_p)}. \tag{76}$$

In this case, we still have two families of modes, but these do not correspond to oscillations in the single fluids as in the sound wave case, but rather represent an inertial mode where the two fluids flow together, which represents the standard inertial mode of the system, and a mode in which the two fluid oscillate relative to each other, the frequency of which is affected by entrainment [69].

VI. INCLUDING MUTUAL FRICTION

So far it has been assumed that the two fluids can oscillate without any dissipation mechanism. The mutual friction will couple the two fluids and generally tend to damp any relative motion. To study this problem, we consider a selection of analytically tractable cases and defer the reader to Sec. VII for the full analysis. We begin with a discussion of inertial waves, as it is known that inertial modes may be dynamically unstable in the presence of a background flow [28,30,52].

Let us start our analysis of inertial waves by considering the weak drag regime, such that $\mathcal{R} \ll 1$, which results in $\mathcal{B}' \ll \mathcal{B}$. We thus take $\mathcal{B}' = 0$, and also set $c_n = c_p = C_n = C_p = 0$ as we are interested in inertial waves. In the case in which there is no background flow, i.e., $w^i_{np} = v^i_n = 0$, the dispersion relation follows from

$$[(4(\Omega\cos\theta)^2-\omega^2)(4(\Omega\cos\theta)^2-(2\mathcal{B}k_i\Omega^i(1+\tilde{\rho}) - i(1-\varepsilon_n-\varepsilon_p)\omega)^2] = 0,$$

where $\tilde{\rho} = \rho_n/\rho_p$. The solutions are still an undamped inertial mode, which we identify with the comoving mode, as in this case there is no relative motion and no mutual friction (note that in a full spherical analysis rotation couples the two motions at higher order and results in mutual friction damping even for the standard comoving mode, see Haskell *et al.* [69]), and the damped counter-moving mode, modified by entrainment.

$$\omega = \pm 2\Omega\cos\theta \tag{77}$$

$$\omega = \frac{2\Omega\cos\theta}{1-\varepsilon_n-\varepsilon_p}(\pm 1 - i\mathcal{B}(1+\tilde{\rho})). \tag{78}$$

Note that the denominator is always positive, $1-\varepsilon_n-\varepsilon_p>0$, as required by stability on a microscopic scale [65]. The mode is therefore always stable, but we see here that our study of large scale hydrodynamical instabilities, such as the one that would arise if $1-\varepsilon_n-\varepsilon_p<0$, successfully captures a more general physical instability of the system.

A. Background flow

We now consider the physically realistic case in which the fluids are not corotating in the background, for example due to vortex pinning in the crust. The analysis is now more involved, so we will consider two cases separately: counterflow along the axis of the vortex array (the DG instability) and counterflow perpendicular to the axis.

1. The Donnelly-Glaberson instability

To study the instabilities that arise due to counterflow along the vortex axis, we specialize our setup, and consider only modes propagating along the vortex axis, which is taken to be aligned with the rotation axis along z. We thus have $k_x = k_y = 0$. To begin our analysis, we consider the simplified case with no entrainment, i.e., $\varepsilon_x = \varepsilon_y = 0$ and also start from the assumption $\tilde{\rho} = \rho_n/\rho_p = 0$, which corresponds to assuming that the mutual friction only acts on the neutrons. This not only simplifies the calculations, but it corresponds to assuming that the protons and electrons are "clamped" to the normal fluid (e.g., their motion is entirely dictated by the magnetic field). In this case, the dispersion relation is

$$\omega(k_z v_n^z+\omega)(4\Omega^2-\omega^2)((2\Omega-i\mathcal{B}k_z v_n^z)^2 - (2\mathcal{B}\Omega+i(k_z v_n^z-\omega))^2) = 0, \tag{79}$$

which, apart from the trivial solutions corresponding to the choice of coordinate system, has solutions

$$\omega = \pm 2\Omega \tag{80}$$

$$\omega = \mp 2\Omega - 2i\mathcal{B}\Omega \pm i\mathcal{B}k_z v_n^z + k_z v_z^n. \tag{81}$$

The first solution corresponds to standard inertial waves (the factor $\cos\theta = 1$ due to our choice of direction of $\mathbf{k}$), the second corresponds to the DG instability and is generally unstable as long as $|v_n| > 2\Omega/|k_z|$. If we consider a standard pulsar such that $2\Omega \approx 100$ rad/ sec and hydrodynamical scales such that $|k_z| < 1$ cm^{-1}, then we have an instability if $|v_n| > 10^2$ cm/s, which corresponds to a lag of $\Delta\Omega \approx 10^{-4}$, in the outer layers of the star, which is easily sustainable by pinning forces in the crust [70]. Such an instability is thus always likely to be present, as vortex bending and large scale flows in the normal fluid, coupled to the superfluid, will always induce counterflow along the vortex array. The fact that the instability exists even if $\tilde{\rho} = 0$ and mutual friction is not acting on the protons, suggests the instability will exist even in the presence of strong magnetic fields, as suggested by the analysis of van Eysden and Link [30].

If we relax our approximations, and take $\tilde{\rho} \neq 0$ and include entrainment in our analysis, the full solution is intractable. We thus consider the weak drag case, for which $\mathcal{R} \ll 1$, and we can take $\mathcal{B}' \approx 0$. Furthermore, we consider two limiting cases, the small entrainment limit, which is relevant for the core of the star, and the large entrainment limit, relevant for the crust. For small entrainment $\varepsilon_{\rm n} < \varepsilon_{\rm p} \ll 1$, we have

$$\mathrm{Re}(\omega) = \pm 2(1+\varepsilon_{\rm p})\Omega + \frac{\mathcal{B}^2(k_z v_{\rm n}^z \pm 2\Omega)}{(k_z v_{\rm n}^z)^2 + \mathcal{B}^2[(k_z v_{\rm n}^z)^2 \pm \Omega k_z v_{\rm n}^z + 4\Omega^2]} \tag{82}$$

$$\mathrm{Im}(\omega) = \mp \frac{4\mathcal{B}\varepsilon_{\rm p}\Omega^2 k_z v_{\rm n}^z}{(k_z v_{\rm n}^z)^2 + \mathcal{B}^2[(k_z v_{\rm n}^z)^2 \pm \Omega k_z v_{\rm n}^z + 4\Omega^2]} \tag{83}$$

and

$$\mathrm{Re}(\omega) = \pm 2(1+\varepsilon_{\rm n})\Omega + k_z v_{\rm n}^z - \frac{4\mathcal{B}^2\varepsilon_{\rm p}\Omega^2(k_z v_{\rm n}^z \pm 2\Omega)}{(k_z v_{\rm n}^z)^2 + \mathcal{B}^2[(k_z v_{\rm n}^z)^2 \pm \Omega k_z v_{\rm n}^z + 4\Omega^2]} \tag{84}$$

$$\mathrm{Im}(\omega) = -\mathcal{B}[k_z v_{\rm n}^z + 2\Omega(1+\varepsilon_{\rm n} \pm \varepsilon_{\rm p})] \mp \frac{4\mathcal{B}\varepsilon_p\Omega^2 k_z v_{\rm n}^z}{(k_z v_{\rm n}^z)^2 + \mathcal{B}^2[(k_z v_{\rm n}^z)^2 \pm \Omega k_z v_{\rm n}^z + 4\Omega^2]}. \tag{85}$$

We see that in the presence of a background flow entrainment modifies also the comoving mode, which is now potentially unstable. For weak drag, if we expand to first order in $\mathcal{B}$, we see that the mode is always unstable for

$$\frac{1}{|k_z|} > \frac{|v_{\rm n}|}{4\mathcal{B}\varepsilon_{\rm p}\Omega^2}, \tag{86}$$

which means that in the presence of a lag, due to core pinning (e.g., of neutron vortices to proton fluxtubes), the vortex array is generally unstable on all hydrodynamical length scales for standard parameters ($\mathcal{B} \approx 10^{-4}$, $\Omega \approx 100$, $\varepsilon_{\rm p} = 0.6$, $|v_{\rm n}| = 10^4$ cm/s).

2. Two stream instability

Let us now consider the case of a two stream instability, in which there is a counterflow perpendicular to the vortex axis, which we take to be aligned with the rotation axis such that $\hat{\kappa}^i = \hat{\Omega}^i = \hat{z}^i$. We thus have $v_x^{\rm n} \neq 0$, with $v_y^{\rm n} = 0$, $v_z^{\rm n} = 0$, and to keep the calculation tractable we consider the case in which $\varepsilon_{\rm x} = 0$ and take the protons to be clamped to the normal fluid ($\tilde{\rho} = 0$). The dispersion relation is

$$\begin{aligned}&\omega(k_x v_{\rm n}^x - \mathcal{B}k_y v_{\rm n}^x - \omega)(4\Omega^2 - \omega^2) \\ &\quad\times (4(1+\mathcal{B}^2)\Omega^2 - 2i\mathcal{B}\Omega(-k_x v_{\rm n}^x + \mathcal{B}k_y v_{\rm n}^x + 2\omega) \\ &\quad - (k_x v_{\rm n}^x - \omega)(k_x v_{\rm n}^x - \mathcal{B}k_y v_{\rm n}^x - \omega)) = 0.\end{aligned} \tag{87}$$

Apart from the trivial solution, we now have solutions of the form

$$\omega = 2\Omega - 2i\mathcal{B}\Omega + k_x v_{\rm n}^x \pm \frac{1}{2}\mathcal{B}k_y v_{\rm n}^x \pm \frac{1}{2}\sqrt{1 - i\frac{\mathcal{B}k_x v_{\rm n}^x}{2\Omega} + \frac{\mathcal{B}^2 k_y^2 (v_x^{\rm n})^2}{16\Omega^2}}. \tag{88}$$

This mode can be unstable due to the induced flow in the y direction caused by the background flow in the x direction. An expansion for $\mathcal{B} \ll 1$ reveals that the criterion for instability is

$$-\mathrm{Im}(\omega) = 2\mathcal{B}\Omega + \frac{1}{2}\mathcal{B}k_x v_{\rm n}^x < 0. \tag{89}$$

This gives the condition for the instability to develop

$$v_x^{\rm n} > \frac{4\Omega}{|k_x|}, \qquad k_x > 0 \tag{90}$$

$$v_x^{\rm n} < -\frac{4\Omega}{|k_x|}, \qquad k_x < 0. \tag{91}$$

Note, this condition does not contain dependence on k_y. To obtain this, we need to expand the second order in small parameter $|v_{\rm n}|/\Omega$, which leads to

$$-\mathrm{Im}(\omega) = 2\mathcal{B}\Omega + \frac{\mathcal{B}}{2}k_x v_{\rm n}^x - \frac{\mathcal{B}^3 k_x^3 (v_{\rm n}^x)^3}{64\Omega^2} - \frac{\mathcal{B}^3 k_x k_y^2 (v_{\rm n}^x)^3}{64\Omega^2}. \tag{92}$$

As we can see mutual friction does not affect the critical velocity for the instability to set in, but affects its growth rate, with higher mutual friction causing a faster rise of the instability with increasing velocity.

B. The strong drag regime

We now move on to consider the case of a strong drag, that corresponds to $\mathcal{R} \gg 1$, in which case the parameter $\mathcal{B}'$ can no longer be neglected. This case may be applicable in regions with strong pinning [71–73] and may have important consequences for the development of the r-mode instability [41,69]. Let us begin our analysis by the equivalent of the DG instability, in which the relative flow is along the vortex axis, taken to coincide with rotational axis, or $v_x^{\rm n} = v_y^{\rm n} = 0$ and $v_z^{\rm n} \neq 0$, and we also take $\varepsilon_{\rm x} = 0$. We consider the limit $\mathcal{R} \ll 1$ for which $\mathcal{B} \approx 0$ and $\mathcal{B}' \approx 1$. In this case, the spectrum is given by

$$\omega = 2\Omega - \mathcal{B}'\Omega(1+\tilde{\rho}) - \frac{1}{2}k_z v_n^z + \frac{1}{2}\mathcal{B}' k_z v_n^z \pm \frac{1}{2}\sqrt{T_1}$$
$$\omega = -2\Omega + \mathcal{B}'\Omega(1+\tilde{\rho}) + \frac{1}{2}k_z v_n^z + \frac{1}{2}\mathcal{B}' k_z v_n^z \pm \frac{1}{2}\sqrt{T_2}, \quad (93)$$

with

$$T_1 = \mathcal{B}'^2(-2\Omega(1+\tilde{\rho}) + k_z v_{\rm n}^z)^2 + 2\mathcal{B}' k_z v_{\rm n}^z[2\Omega(-1+\tilde{\rho}) + k_z v_{\rm n}^z)] + (k_z v_{\rm n}^z)^2$$
$$T_2 = \mathcal{B}'^2(2\Omega(1+\tilde{\rho}) + k_z v_{\rm n}^z)^2 + 2\mathcal{B}' k_z v_{\rm n}^z[2\Omega(1-\tilde{\rho}) + k_z v_{\rm n}^z] + (k_z v_{\rm n}^z)^2. \quad (94)$$

For standard neutron star parameters, these modes are not unstable, and in fact if we expand for $\mathcal{B}' \ll 1$, we obtain

$$\omega = 2\Omega + 2\mathcal{B}'\Omega + k_z v_{\rm n}^z \pm \mathcal{B}' k_z v_{\rm n}^z$$
$$\omega = -2\Omega + 2\mathcal{B}'\Omega + k_z v_{\rm n}^z \pm \mathcal{B}' k_z v_{\rm n}^z, \quad (95)$$

which are stable, modified inertial modes.

C. Sound waves and mutual friction

To study the effect of mutual friction on sound waves, we can consider an expansion in Ω around the $\Omega = 0$ solution $\omega = \pm c_{\rm n} k$. Let us consider the modes of the superfluid, in the clamped proton approximation. Defining θ to be the angle between the wave vector and the rotation axis, we find that for $\varepsilon_{\rm x} = C_{\rm x} = w_{\rm xy} = v_{\rm n} = 0$, we have

$$\omega(k) = \pm c_{\rm n} k - i\mathcal{B}\Omega^2 \sin^2\theta \pm \frac{\Omega^2 \sin^2\theta}{2c_{\rm n}k}(4 - 8\mathcal{B}' + 4\mathcal{B}'^2 - 5\mathcal{B} + \mathcal{B}^2\cos 2\theta). \quad (96)$$

The effect of the mutual friction disappears when the wave vector is aligned with the vorticity, i.e., $\theta = 0$; in this case, the velocity perturbation is parallel to the vortex array and there cannot be any mutual friction effect (all the cross products in 28 are zero). Things are very different if a background velocity lag is present (even if this lag is parallel to the vortex array) because vorticity perturbations enter the game: this will be investigated numerically in the next sections.

In the weak drag limit, we may set $\mathcal{B}' \approx \mathcal{R}^2$ and $\mathcal{B} \approx \mathcal{R}$ and the relevant terms become

$$\omega = \pm c_{\rm n} k - i\mathcal{R}\Omega^2 \sin^2\theta \pm \frac{\Omega^2 \sin^2\theta}{2c_{\rm n}k}(4 - 5\mathcal{R}). \quad (97)$$

D. Isotropic (Gorter-Mellink) mutual friction

We now consider the Gorter-Mellink form for the mutual friction in (10) to investigate if and how the presence of an isotropic vortex tangle modifies the previous results. In the limit $kc_{\rm n} \gg A_{GM}|\mathbf{v}_n|^2$, it is possible to write the exact implicit form of the dispersion relation, which is

$$\omega(k) = \pm 2\Omega|\cos\theta| - i\alpha_I^{\pm} A_{GM}|v_{\rm n}|^2\left(1 - \frac{f_I^{\pm}\Omega^2}{c_{\rm n}k^2}\right)$$
$$\omega(k) = \pm\left(c_{\rm n}k + \frac{2\Omega^2}{c_{\rm n}k^2}\right) - i\alpha_S^{\pm} A_{GM}|v_{\rm n}|^2\left(1 - \frac{f_S^{\pm}\Omega^2}{c_{\rm n}k^2}\right) \quad (98)$$

for inertial and sound waves, respectively. Here, $f_I^{\pm} \sim 1$ and $f_S^{\pm} \sim 1$ are four involved functions of the angles between the vectors $\mathbf{v}_n$, $\mathbf{k}$, and $\mathbf{\Omega}$, as well as the two positive functions $\alpha_I^{\pm} > 0$ and $\alpha_S^{\pm} > 0$. Irrespectively of the mutual orientation and magnitude of the three vectors (provided that kc_n is always much bigger than Ω and $A_{GM}|\mathbf{v}_n|^2$), we are always in a damped regime in which the damping timescale is of the order of $A_{GM}^{-1}|\mathbf{v}_n|^{-2}$ for both inertial and sound waves.

It would thus appear that a rectilinear vortex array is rapidly destabilized as unstable inertial modes develop due to counterflow. If an (approximately) isotropic vortex tangle develops this remains stable, at least until the turbulent tangle decays. Once a rectilinear array is restored, the system is again unstable, leading to a recurrent mechanism that may be linked to the trigger of pulsar glitches. A more detailed analysis in the case of a polarized turbulent tangle should be the focus of future work.

Note that as the modes in (98) are stable, we will not consider isotropic mutual friction in the numerical analysis in the following section.

VII. NUMERICAL RESULTS

All the machinery needed to derive the general dispersion relations for the various modes of oscillation of the two-fluid system is presented in Appendix. The final result is the matrix M in (A25), which depends on some basic local quantities that define how the system responds to a perturbation in the velocity fields: the full matrix (or its determinant) can be seen as a function of ω and $\mathbf{k}$ and depends on several parameters, namely

$$M = M(\omega, \mathbf{k}; \mathbf{v}_n, \boldsymbol{\omega}, \mathbf{\Omega}; \varepsilon_{\rm x}, \rho_{\rm x}, \alpha_{\rm x}, A_{\rm x}, C_{\rm x}, c_{\rm x}; \mathcal{B}, \mathcal{B}'). \quad (99)$$

Leaving aside the obvious dependence on the pulsation ω and on $\mathbf{k}$, the other parameters (that describe completely the hydrodynamic state of the background configuration when there is no turbulence and magnetic field) have been formally divided into three sets, which helps us to discuss their role.

The first set comprises the variables $\mathbf{v}_n$, $\boldsymbol{\omega}$, and $\mathbf{\Omega}$: they define the state of motion of the background configuration in which the normal component rotates rigidly. We allow for a stationary nonzero local velocity lag $\mathbf{v}_n = \mathbf{w}_{\rm np}$, which is expected to be nonconstant on the stellar radius length scale. Therefore, in a purely local analysis, the background vorticity field $\boldsymbol{\omega}$ is not expressible in terms of the local (constant) value of $\mathbf{w}_{\rm np}$: only a true solution of the unperturbed equations of motion would lead to locally

TABLE I. The two prototype cases, for the crust and core of the star, that have been tested in the numerical analysis of the determinant. For each of these five cases, we consider nine different relative orientations of the local lag $\mathbf{v}_n$ and $\mathbf{k}$ and the three mutual friction scenarios listed in Table II. Each of these cases has been investigated by considering two relative velocity speeds between neutrons and the normal component $|\mathbf{v}_n| = 1$ cm/s and $|\mathbf{v}_n| = 10^4$ cm/s.

Case	ρ_n	c_n	c_p	ε_n	ε_p	Ω	$\lvert\boldsymbol{\omega}\rvert$	$\hat{\boldsymbol{\omega}}$	$A_{n,p}$	$C_{n,p}$
Crust	$4\rho_p$	10^9 cm/s	$0.51c_n$	-10	-40	100 rad/s	200 rad/s	$\hat{\mathbf{z}}$	0	0
Core	$4\rho_p$	10^9 cm/s	$0.51c_n$	0.15	0.6	100 rad/s	200 rad/s	$\hat{\mathbf{z}}$	0	0

consistent values for $\mathbf{w}_{\rm np}$, $\boldsymbol{\omega}$, and $\boldsymbol{\Omega}$, but would prevent us to test the more general case in which the local direction and magnitude of these vectors are chosen at will.

The second set of parameters describes the local state of matter in the stationary configuration. It can be further divided into two subsets. The four parameters $\varepsilon_{\rm x}$ and $\rho_{\rm x}$ are defined by considering the first law of thermodynamics (16) and their unperturbed value can oscillate: indeed, we introduced the linear combinations (46) and (48) to express their amplitudes in terms of the perturbed velocities (the same is valid for the chemical potentials $\tilde{\mu}_{\rm x}$, with the only caveat that the unperturbed value of the chemical potentials does not enter into the explicit expression of M). The second subset comprises $\alpha_{\rm x}$, $A_{\rm x}$, $C_{\rm x}$, and $c_{\rm x}$, that are related to second order derivatives of the internal energy E; in a first-order analysis, these quantities are fixed to their unperturbed value and allow, together with the unperturbed values $\rho_{\rm x}$ and $\varepsilon_{\rm x}$, to express the fundamental thermodynamic perturbations $\delta\rho_{\rm x}$, $\delta\varepsilon_{\rm x}$, and $\delta\tilde{\mu}_{\rm x}$, as described in Sec. III A.

Finally, the two parameters $\mathcal{B}$ and $\mathcal{B}'$ define the "state" of the vortex array (note again, that we only consider the standard, anisotropic form of the mutual friction, and not the Gorter-Mellink form, as we have found modes to be stable for this form of the mutual friction). We do not consider variations of these parameters and their value has to be fixed according to the mutual friction scenario that we are interested to test. In the subsequent numerical analysis, we consider different possibilities, listed in Tables I and II.

From the analytic point of view, writing down the full matrix M is of little interest, but its complete and explicit form in components can be easily obtained with the aid of any software for symbolic computation, as outlined in Appendix. Although extremely complex, also the full and exact determinant of M can be obtained as well. At this point, we substitute a particular choice for the background parameters into the complete expression of the determinant; the roots of $\det M(\omega, \mathbf{k}) = 0$, which is a high degree polynomial equation in the pulsation ω, can be computed numerically for different values of $\mathbf{k}$. By varying $\mathbf{k}$ and the parameters, some branches of the dispersion relation $\omega(\mathbf{k})$ may result in a positive imaginary part. The associated instability timescale is then defined as

$$T(\mathbf{k}) = \frac{2\pi}{\mathrm{Im}(\omega(\mathbf{k}))}. \tag{100}$$

Since we worked within a purely hydrodynamic framework, it is important to stress that not all the values of $|\mathbf{k}|$ are physically meaningful. As also discussed in [30], the wave vector should be much smaller than the inverse of the stellar radius, otherwise the effect of stratification is expected to modify the dispersion relation (namely, the background quantities have spatial dependence on such length scales and cannot be considered uniform, as in the present local analysis). Since the stellar radius is about $R \sim 10$ km, we should consider $|\mathbf{k}| \gg 10^{-6}$ cm^{-1}: therefore, we expect the present analysis to be valid for $|\mathbf{k}| \sim 10^{-3}$ cm^{-1} since significant density changes are expected to occur on the length scale of about 10 m, especially at the core-crust interface.

On the other hand, the definition of the superfluid momentum and vorticity needs a suitable average on a macroscopic sample of matter containing many vortex lines, in which average separation is expected to be of the order of $\sim 10^{-3}$ cm. Therefore, we expect the present analysis to break down when the wave vector reaches the critical value $|\mathbf{k}| \sim 10^3$ cm^{-1}. For this reason, the region outside the physically interesting range $10^{-3} < |\mathbf{k}|$ cm $< 10^3$ is shaded in the plots of the instability timescales.

Considering the relative orientation of four different vectors ($\mathbf{v}_n$, $\boldsymbol{\Omega}$, $\boldsymbol{\omega}$, and $\mathbf{k}$) leads to a huge parameter space; therefore, in the numerical analysis we stick to the case in which $\boldsymbol{\Omega} = \Omega\hat{\mathbf{z}}$ and $\boldsymbol{\omega} = 2\boldsymbol{\Omega}$, while $\mathbf{v}_n$ and $\mathbf{k}$ are chosen to be aligned with one of the three directions $\hat{\mathbf{x}}$, $\hat{\mathbf{y}}$, or $\hat{\mathbf{z}}$, for a total of nine combinations [74]. However, for simplicity, only the interesting cases that allow for unstable modes are shown in figures and discussed.

First of all we consider the DG instability, for strong and weak drag and in the "pinned" scenario, which we mimic

TABLE II. The mutual friction scenarios considered in the numerical analysis: for each case listed in Table I, we consider these four mutual friction regimes.

Description	$\mathcal{B}'$	$\mathcal{B}$	$\mathcal{R}$
Pinned vortices	1	0	∞
Free vortices	0	0	0
Strong drag	0.5	0.5	1
Weak drag	10^{-4}	10^{-2}	$\approx 10^{-2}$

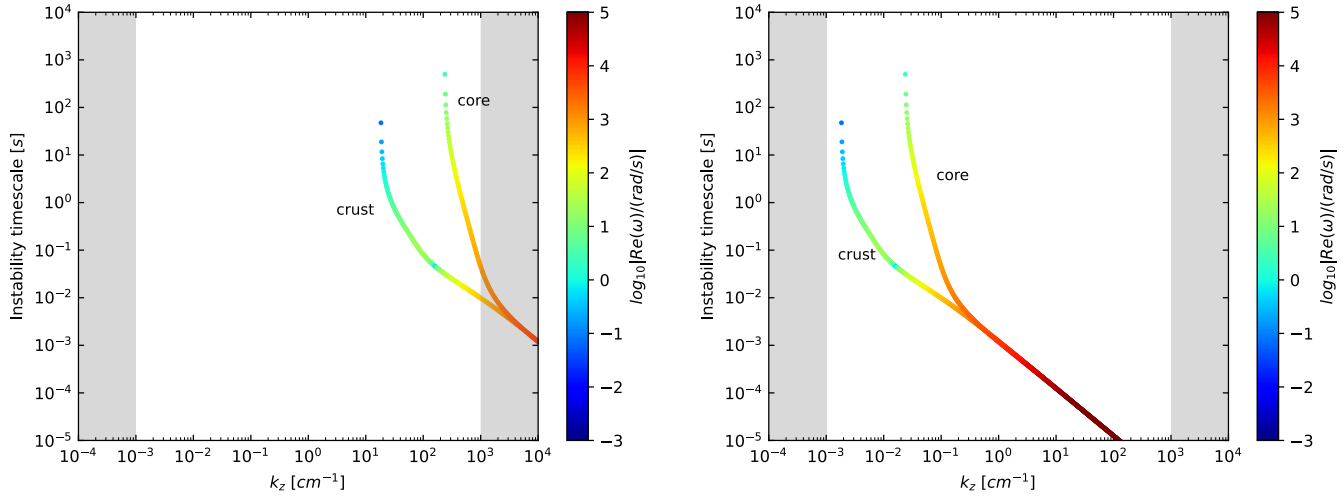

FIG. 3. Instability timescale $T(\mathbf{k})$ versus wave-vector $\mathbf{k}$ for the DG instability, in which the counterflow and k are along the vortex axis in the z direction. The color coding expresses the real part of the oscillation frequency (note that the rotation rate of the star, i.e., of the "normal" component, is taken to be $\Omega = 100$ rad/s). We consider the strong drag case with $\mathcal{B} = \mathcal{B}' = 0.5$ and two values for the background lag, a low value of $v_n^z = 1$ cm/s (left), and a high value (corresponding approximately to the maximum that pinning forces can sustain), of $v_n^z = 10^4$ cm/s (right). In general, we see that there are always mixed inertial-sound waves, that are unstable on dynamical timescales, and are increasingly unstable on small length scales, and that for large enough background velocity lags, the whole dynamical range is unstable.

by taking $\mathcal{B}' = 1$, but $\mathcal{B} = 0$. In Figs. 3 and 5, we plot the instability timescale for strong drag (weak drag is qualitatively similar) and for pinned vortices, for varying values of the background lag. In general, we confirm the results of the analysis in Sec. VI A 1, there exists a family of mixed inertial and sound waves, that are unstable on dynamical timescales, both in the core and crust. Mutual friction has little effect on damping the instability (in fact it is at the heart of driving it), and rather it is the lag that plays a role in determining the onset of the instability. For small values of the lag of $v_n^z = 1$ cm/s, corresponding to $\Delta\Omega \approx 10^{-5}$ in the outer core or inner crust, assuming a radius of $R \approx 10$ km, only the shortest length scales are unstable. For higher lags ($v_n^z = 10^4$ cm/s, $\Delta\Omega \approx 10^{-2}$), all the dynamical range is unstable, and we can thus assume that once pinning allows for a significant enough lag to develop, the array will go unstable, possibly playing a role in triggering pulsar glitches or contributing to timing noise.

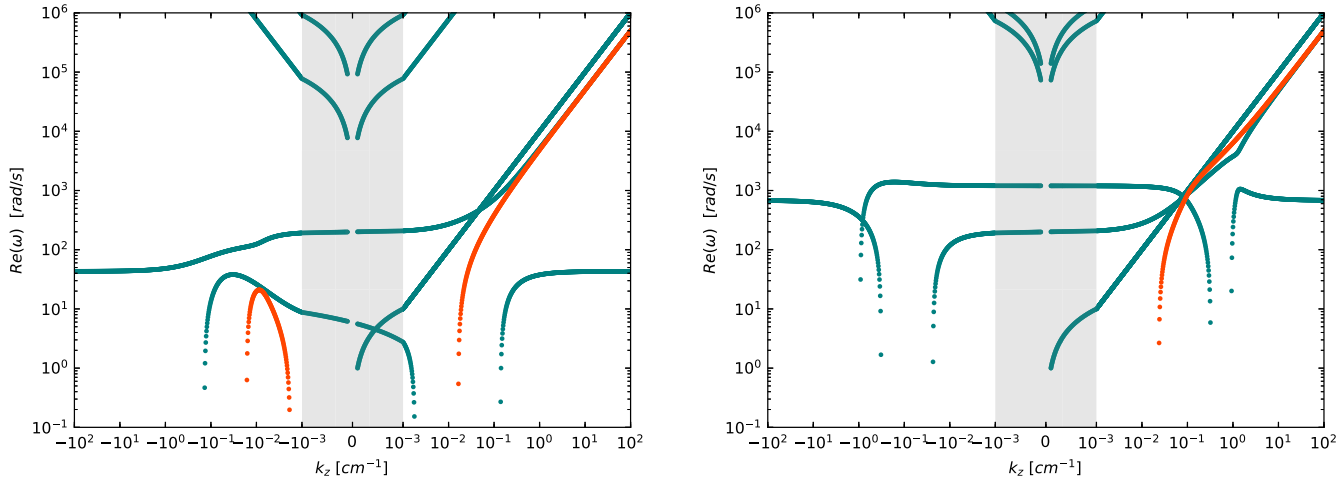

FIG. 4. Dispersion relations (real part of ω vs k_z) for the crust (left) and core (right) of the neutron star, for a lag of $v_n^z = 10^4$ cm/s in the case of strong drag ($\mathcal{B} = \mathcal{B}' = 0.5$), for the DG instability in which we consider the background lag along the vortex axis, i.e., the z axis. We can see that there are mode crossings between families of inertial and sound waves, and in red we have the unstable modes, which are modified sound-inertial waves. In the crust, in the presence of large entrainment, an additional unstable inertial mode is present for negative values of k_z. The shading identifies the region in which the scale of the horizontal axis is linear.

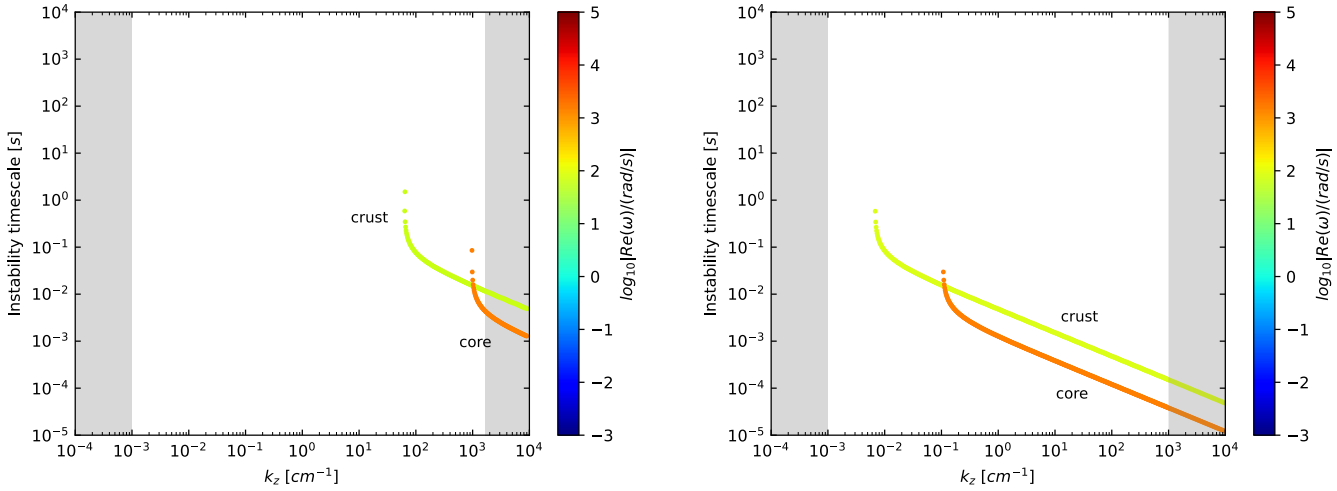

FIG. 5. Instability timescale versus wave-vector **k** for the DG instability, in which the counterflow and k are along the vortex axis in the z direction. The color coding expresses the real part of the oscillation frequency (note that the rotation rate of the star, i.e., of the "normal" component, is taken to be $\Omega = 100$ rad/s). The setup us the same as in Fig. 3, but here we consider the "pinned" case with $\mathcal{B} = 0$ and $\mathcal{B}' = 1$, again two values for the background lag, a low value of $v_n^z = 1$ cm/s (left), and a high value of $v_n^z = 10^4$ cm/s (right). We see that we still have unstable modes, although if one observes the dispersion relation in Fig. 6, it is clear that these are now inertial waves and not mixed sound-inertial waves as in the strong drag case (the weak drag case is qualitatively similar to the strong drag one).

In Figs. 4 and 6, we plot the dispersion relation for both the strong drag and pinned case. We see that the nature of the unstable modes changes: in the pinned case, inertial modes are unstable, while in the strong drag case (and we have verified that the same is true for weak drag), the unstable mode is a modified sound wave.

In Fig. 7, we consider the two-stream instability, in which the background counterflow is taken perpendicular to the vortex (and rotation) axis. Here again we confirm our analytical results from Sec. VI A 2. There are mixed sound-inertial waves (as can be verified from the dispersion relation in Fig. 8) that are unstable on dynamical timescales, and the unstable range depends strongly on the magnitude of the background counterflow velocity. For high values, as may be expected from strong pinning, $v_n^x = 10^4$ cm/s, the whole dynamical range is unstable, with the instability developing on similar timescales at all scales. For $v_n^x = 1$ cm/s, on the other hand, only the smallest length scales are unstable, and the instability develops on longer timescales, that may be affected by other viscous mechanisms, such as shear viscosity.

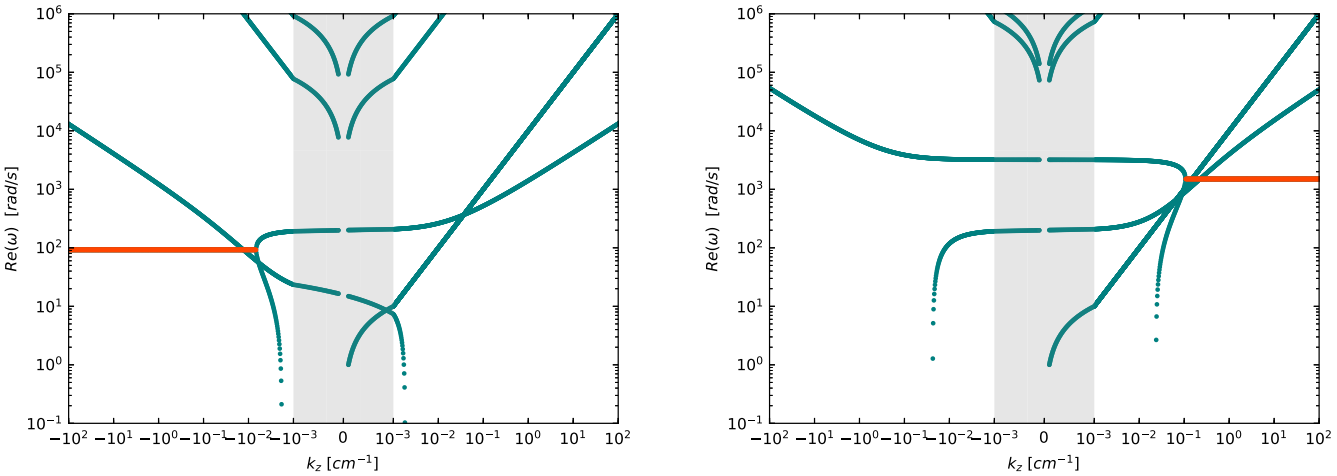

FIG. 6. Dispersion relations (real part of ω vs k_z) for the crust (left) and core (right) of the neutron star, for a lag of $v_n^z = 10^4$ cm/s for the pinned case ($\mathcal{B} = 0, \mathcal{B}' = 1$), in the case of the DG instability in which we consider the background lag along the vortex axis, i.e., the z axis. Unlike in the strong drag case in Fig. 4, the unstable modes (in red) are now clearly inertial waves. The shading identifies the region in which the scale of the horizontal axis is linear.

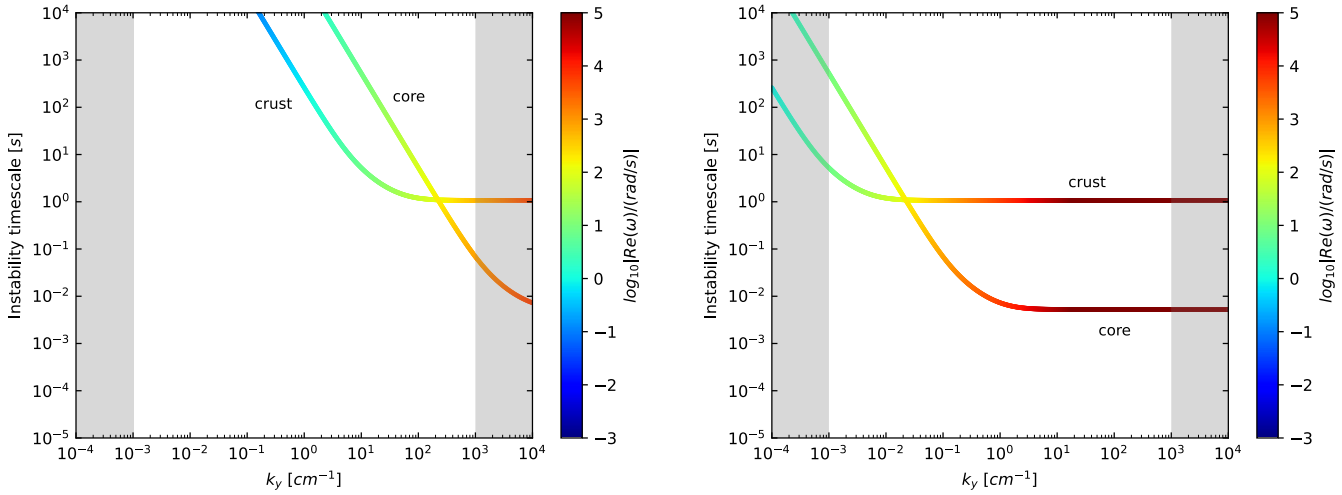

FIG. 7. Instability timescale versus wave-vector **k** for the two-stream instability, in which the counterflow and k are taken perpendicular to the vortex axis, in this case in the y direction. The color coding expresses the real part of the oscillation frequency (note that the rotation rate of the star, i.e., of the 'normal' component, is taken to be $\Omega = 100$ rad/s). As in previous cases, we consider the strong drag case with $\mathcal{B} = \mathcal{B}' = 0.5$ and two values for the background lag, a low value of $v_n^y = 1$ cm/s (left), and a high value (corresponding approximately to the maximum that pinning forces can sustain), of $v_n^y = 10^4$ cm/s (right). In general, we see that there are always mixed inertial-sound waves, that are unstable on dynamical timescales, and that for large enough background velocity lags, the whole dynamical range is unstable.

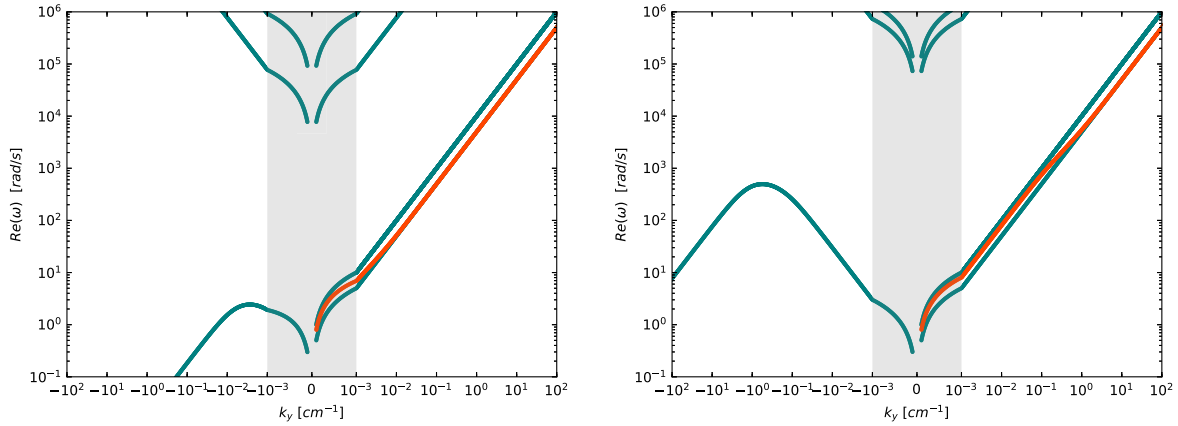

FIG. 8. Dispersion relations (Real part of ω vs k_y) for the crust (left) and core (right) of the neutron star, for a lag of $v_n^y = 10^4$ cm/s for the strong drag case ($\mathcal{B} = \mathcal{B}' = 0.5$), for the two-stream instability in which we consider the background lag perpendicular to the vortex axis, i.e., the y axis (the vortex is taken to be aligned with the z axis). The unstable modes (in red) appear to be sound-inertial waves. Note that for the pinned or weak drag case, no instabilities are present. The shading identifies the region in which the scale of the horizontal axis is linear.

VIII. CONCLUSIONS

We have studied the modes of oscillation of a superfluid neutron star, accounting for background counterflows and including entrainment. We have considered the effect for both standard HVBK mutual friction that arises if the vortex array is straight, and the Gorter-Mellink isotropic form, relevant for fully developed turbulence.

We find that for standard mutual friction there is always a fast instability in the case of counterflow along the vortex axis (which may arise, for example, if the star is precessing, or if vortices bend on a large scale), which is the neutron star analog of the Donnelly-Glaberson instability that is observed in laboratory studies of superfluid helium. We also confirm the existence of a rapid two-stream instability when the background counterflow is perpendicular to the vortex axis (as is expected if a difference in angular velocity between the superfluid and the normal fluid arises due to pinning).

We find that entrainment plays an important role in the instability, and its effect is twofold. On the one side, it

extends the dynamical range over which inertial modes are unstable in the crust, but on the other it significantly shortens the growth time in the core of the star.

When we consider isotropic Gorter-Mellink mutual friction, we find that the previous instabilities are stabilized. This suggests that once a large enough lag sets in, the instabilities we have presented will disrupt the straight vortex array and a turbulent tangle will develop. At this point, the system is stable until the turbulence decays and the process will start again. It is thus very likely that transitions to turbulence play a role in triggering pulsar glitches and in timing noise [48,75].

An important effect that we have not considered is that of the magnetic field. The problem is complicated, as the interior field configuration of a neutron star is generally unknown, but van Eysden and Link [30] found that for simple field geometries the two-stream instability can be stabilized, while the Donnelly-Glaberson instability is always present. We have mimicked the effect of the magnetic field by studying a setup in which the proton fluid is "clamped" and not affected by the mutual friction (to imitate the situation in which it is held in place by magnetic stresses) and find that the two-stream instability is still present in the weak drag regime when entrainment is present. Future work should focus on the full problem, accounting also for superconductivity in the core and the interaction between neutron vortices and superconducting flux tubes [76].

ACKNOWLEDGMENTS

We acknowledge support from the Polish National Science Centre grant SONATA BIS 2015/18/E/ST9/00577. Partial support comes from PHAROS, COST Action CA16214. We thank the Institute for Nuclear Theory at the University of Washington for its kind hospitality and stimulating research environment. This research was supported in part by the INT's U.S. Department of Energy Grant No. DE-FG02- 00ER41132.

APPENDIX: DERIVATION OF THE DISPERSION MATRIX

In this appendix, we provide a more self-contained description of how to perform the local variations by using directly the plane wave ansatz and find the dispersion matrix of the two-fluid system. In the following, the indexes x and y are always meant to be different (x ≠ y), while x and y′ can assume the same value.

For clarity, let us list all the quantities that appear into the Euler equations (1) as the entries of a vector Q, namely

$$Q = (v_{\mathrm{x}}^i, \rho_{\mathrm{x}}, \tilde{\mu}_{\mathrm{x}}, \varepsilon_{\mathrm{x}}, p_{\mathrm{x}}^i, \omega^i, \hat{\omega}^i). \tag{A1}$$

Note that the gravitational potential Φ is not included into the set of variables that we perturb, as well as the mutual friction parameters $\mathcal{B}$, $\mathcal{B}'$, and A_{GM}. The angular velocity Ω is also kept constant and defines the rotating frame in which $\mathbf{k}$ and the pulsation ω of the plane wave ansatz (42) are measured. Since the quantities in Q are not all independent, it is convenient to calculate their variation following the order in the list. Once the quantities in Q have been expressed in terms of the velocity fields only, the vector is expanded at the first order as

$$Q[\mathbf{v}_{\mathrm{x}} + \bar{\mathbf{v}}_{\mathrm{x}} e^{i(\mathbf{k}\cdot\mathbf{x}-\omega t)}] \approx Q_B + \sum_{\mathrm{y}} \frac{\partial Q}{\partial \bar{v}_{\mathrm{y}}^j} \bar{v}_{\mathrm{y}}^j. \tag{A2}$$

Hence, the generic amplitudes $\bar{Q}$ introduced in Eq. (44) are obtained by means of the coefficients

$$Q_j^{\mathrm{y}} = e^{-i(\mathbf{k}\cdot\mathbf{x}-\omega t)} \left.\frac{\partial Q}{\partial \bar{v}_{\mathrm{y}}^j}\right|_B = \left.\frac{\partial \bar{Q}}{\partial \bar{v}_{\mathrm{y}}^j}\right|_B. \tag{A3}$$

For ρ_x, $\tilde{\mu}_{\mathrm{x}}$, and ε_{x}, the result has already been given in Sec. IV. From the continuity equation, we find the diagonal elements ρ_j^{xx} of the three 2×2 matrices $\rho_j^{\mathrm{xy}'} = \delta_{\mathrm{xy}'}\rho_j^{\mathrm{xx}}$; see Eq. (46). Now, the thermodynamic relations of Sec. III A allow us to calculate the explicit form of

$$\bar{\mu}_{\mathrm{x}} = \mu_a^{\mathrm{x}n}\bar{v}_n^a + \mu_a^{\mathrm{x}p}\bar{v}_p^a \tag{A4}$$

and

$$\bar{\varepsilon}_{\mathrm{x}} = \varepsilon_a^{\mathrm{x}n}\bar{v}_n^a + \varepsilon_a^{\mathrm{x}p}\bar{v}_p^a, \tag{A5}$$

where the matrices $\mu_j^{\mathrm{xy}'}$ and $\varepsilon_j^{\mathrm{xy}'}$ have been given in Eqs. (47) and (48), respectively. Using the result for $\rho_j^{\mathrm{xy}'}$, the final expressions read

$$\begin{aligned} \mu_i^{\mathrm{xx}} &= \frac{c_{\mathrm{x}}^2 k^i}{\omega - \mathbf{k}\cdot\mathbf{v}_{\mathrm{x}}} + \alpha_{\mathrm{x}} w_{\mathrm{xy}}^i \\ \mu_i^{\mathrm{xy}} &= \frac{C_{\mathrm{x}} k^i}{\omega - \mathbf{k}\cdot\mathbf{v}_{\mathrm{y}}} - \alpha_{\mathrm{x}} w_{\mathrm{xy}}^i \end{aligned} \tag{A6}$$

for the specific momentum and

$$\begin{aligned} \varepsilon_i^{\mathrm{xx}} &= (\alpha_{\mathrm{x}} - \varepsilon_{\mathrm{x}}) \frac{k^i}{\omega - \mathbf{k}\cdot\mathbf{v}_{\mathrm{x}}} + A_{\mathrm{x}} w_{\mathrm{xy}}^i \\ \varepsilon_i^{\mathrm{xy}} &= \frac{\alpha_{\mathrm{y}}\rho_{\mathrm{y}}}{\rho_x} \frac{k^i}{\omega - \mathbf{k}\cdot\mathbf{v}_{\mathrm{y}}} - A_{\mathrm{x}} w_{\mathrm{xy}}^i \end{aligned} \tag{A7}$$

for the entrainment parameters.

At this point it is immediate to address also the variations of the momenta and of the vorticity. To give a concrete example of how the linear combination (44) looks like when applied to vectorial quantities, we start by formally writing the momentum amplitude as

$$\bar{p}^i_{\rm x} = p^{{\rm x}n}_{ia}\bar{v}^a_n + p^{{\rm x}p}_{ia}\bar{v}^a_p. \tag{A8}$$

Performing the expansion (A2) on the momenta defined in (4) immediately gives

$$\bar{p}^i_{\rm x} = (1-\varepsilon_{\rm x})\bar{v}^i_{\rm x} + \varepsilon_{\rm x}\bar{w}^i_{\rm y} + v^i_{\rm yx}\bar{\varepsilon}_{\rm x}. \tag{A9}$$

The last term can be expanded thanks to (A5), and (A2) tells us that

$$\begin{aligned} p^{\rm xx}_{ia} &= (1-\varepsilon_{\rm x})\delta_{ia} + w^{\rm yx}_i\varepsilon^{\rm xx}_a \\ p^{\rm xy}_i &= \varepsilon_{\rm x}\delta_{ia} + w^{\rm yx}_i\varepsilon^{\rm xy}_a. \end{aligned} \tag{A10}$$

When the entrainment coefficients (A7) are inserted into the above formulas, we see that the momentum perturbations have a correction which depends on the coefficient $A_{\rm x}$. Not surprisingly, these terms are of the second order in the background velocity lag; it is not particularly convenient to neglect them here, but from the numerical point of view these terms are expected to have little effect on the calculated dispersion relation.

The last ingredient that we need is to write the vorticity perturbation in the same fashion of (44), namely

$$\bar{\omega}_i = \omega^n_{ia}\bar{v}^a_n + \omega^p_{ia}\bar{v}^a_p. \tag{A11}$$

Starting from Eq. (34), or applying directly (A2) on the definition of vorticity together with (A5), it is straightforward to check that

$$\begin{aligned} -i\omega^n_{ia} &= (1-\varepsilon_n)\epsilon_{ija}k^j + \epsilon_{ijl}k^j v^l_{\rm pn}\varepsilon^{nn}_a \\ -i\omega^p_{ia} &= \varepsilon_n\epsilon_{ija}k^j + \epsilon_{ijl}k^j w^l_{\rm pn}\varepsilon^{\rm np}_a. \end{aligned} \tag{A12}$$

Alternatively, the above result can be found directly from (A9) by observing that $\bar{\omega}_i = i\epsilon_{iab}k^a\bar{p}^b_n$. Similarly, the variation of the vorticity versor can be easily obtained by means of the projector in Eq. (35).

1. Left-hand side of the Euler equations

Let us define the right-hand side of Eq. (1) as

$$\mathcal{E}^{\rm x}_i = (\partial_t + v^j_{\rm x}\nabla_j)p^{\rm x}_i + \varepsilon_{\rm x}w^{\rm xy}_j\nabla_i v^j_{\rm x} + \nabla_i\tilde{\mu}_x + 2\epsilon_{ijk}\Omega^j v^k_{\rm x}, \tag{A13}$$

where the gravitational potential Φ and the centrifugal term have been ignored: we are interested in the variation $\delta\mathcal{E}^i_{\rm x}$ and these two terms only contribute to define the background configuration. We extend the notation (42) to $\mathcal{E}^{\rm x}_i$, namely

$$\delta\mathcal{E}^{\rm x}_i = \bar{\mathcal{E}}^{\rm x}_i e^{i(\mathbf{k}\cdot\mathbf{x}-\omega t)}, \tag{A14}$$

where

$$\bar{\mathcal{E}}^{\rm x}_i = \mathcal{E}^{{\rm xx}}_{ia}\bar{v}^a_{\rm x} + \mathcal{E}^{\rm xy}_{ia}\bar{v}^a_{\rm y}. \tag{A15}$$

Using systematically the results obtained so far, a small amount of algebra gives

$$\begin{aligned} i\mathcal{E}^{\rm xx}_{ia} &= (\omega - \mathbf{k}\cdot\mathbf{v}_{\rm x})[(1-\varepsilon_{\rm x})\delta_{ia} + w^{\rm yx}_i\varepsilon^{\rm xx}_a] - k_i(\varepsilon_{\rm x}w^{\rm yx}_a + \mu^{\rm xx}_a) \\ &\quad + 2i\epsilon_{ija}\Omega^j \end{aligned} \tag{A16}$$

and

$$i\mathcal{E}^{\rm xy}_{ia} = (\omega - \mathbf{k}\cdot\mathbf{v}_{\rm x})[\varepsilon_{\rm x}\delta_{ia} + w^{\rm yx}_i\varepsilon^{\rm xy}_a] - k_i\mu^{\rm xy}_a. \tag{A17}$$

In a dynamical regime in which the mutual friction is zero (i.e., in the rather ideal situation in which the vortex lines can be considered free and no drag nor pinning interactions act upon them), this result is sufficient to build the matrix M of Eq. (45). More explicitly, the six equations of the full linear system (45) can be also be written as

$$\begin{aligned} M^{nn}_{ia}\bar{v}^a_n + M^{\rm np}_{ia}\bar{v}^a_p &= 0 \\ M^{\rm pn}_{ia}\bar{v}^a_n + M^{pp}_{ia}\bar{v}^a_p &= 0, \end{aligned} \tag{A18}$$

where the indexes i and a run over the three spatial indexes (the summation over a is understood). Therefore, it should be clear that each block of the full matrix M can be obtained as

$$M^{{\rm x}{\rm y}'}_{ia} = \mathcal{E}^{{\rm x}{\rm y}'}_{ia} \tag{A19}$$

in the free vortex limit.

2. Perturbing the mutual friction

In order to treat consistently the mutual friction term, it is convenient to start from the case ${\rm x} = n$ in (6), namely

$$\mathbf{f}^n = B'\boldsymbol{\omega}\times\mathbf{v}_{\rm np} + B\hat{\boldsymbol{\omega}}\times(\boldsymbol{\omega}\times\mathbf{v}_{\rm np}). \tag{A20}$$

Once the variation $\delta\mathbf{f}^n$ has been obtained, the reaction on the normal component will just be given by

$$\delta\mathbf{f}^p = -\left(\frac{\delta\rho_n}{\rho_p} - \frac{\rho_n}{\rho_p^2}\delta\rho_p\right)\mathbf{f}^n - \frac{\rho_n}{\rho_p}\delta\mathbf{f}^n. \tag{A21}$$

Note that this last equation is valid also for the Gorter-Mellink mutual friction (10). In complete analogy with what has already been discussed for Eq. (A15), we may write

$$\bar{f}^{\rm x}_i = f^{{\rm x}n}_{ia}\bar{v}^a_n + f^{{\rm x}p}_{ia}\bar{v}^a_p. \tag{A22}$$

The calculation leading to an explicit form of the coefficients $f^{{\rm x}{\rm y}'}_{ia}$ is laborious, and the final expression is

complex enough to be useless in an analytic approach. However, it is possible to implement an exact procedure that can be solved by any software for symbolic calculus. First, the amplitude in (A23) can be formally obtained as

$$\bar{f}_i^{\mathrm{x}} = e^{-i(\mathbf{k}\cdot\mathbf{x}-\omega t)} \sum_{\mathcal{Q}} \bar{\mathcal{Q}} \frac{\partial}{\partial \bar{\mathcal{Q}}} \bar{f}_i^{\mathrm{x}} [\mathcal{Q}_B + e^{i(\mathbf{k}\cdot\mathbf{x}-\omega t)} \bar{\mathcal{Q}}], \quad \text{(A23)}$$

where the derivative is evaluated on the background configuration. Therefore, the matrices in (A23) are computed as

$$f_{ij}^{\mathrm{xy}'} = \sum_{\mathcal{Q}} \frac{\partial \bar{f}_i^{\mathrm{x}}}{\partial \bar{\mathcal{Q}}} \frac{\partial \bar{\mathcal{Q}}}{\partial \bar{v}_{\mathrm{y}'}^j}\bigg|_B = \sum_{\mathcal{Q}} \mathcal{Q}_j^{\mathrm{y}'} \frac{\partial \bar{f}_i^{\mathrm{x}}}{\partial \bar{\mathcal{Q}}}\bigg|_B . \quad \text{(A24)}$$

In this way, it is possible to find the complete matrix M of Eq. (99): not surprisingly, its form is defined in terms of the four 3×3 blocks

$$M_{ij}^{\mathrm{xy}'} = \mathcal{E}_{ij}^{\mathrm{xy}'} - f_{ij}^{\mathrm{xy}'} . \quad \text{(A25)}$$

The determinant of this 6×6 matrix is a huge rational function of complex coefficients, which numerator defines a high degree polynomial in ω and in the components of $\mathbf{k}$. The roots of this polynomial define the dispersion relation $\omega(\mathbf{k})$ of the oscillation modes of the two-fluid system. In Sec. VII, the dispersion relations relative to some physically interesting cases are studied numerically within the simplifying assumptions that $C_{\mathrm{x}} = \alpha_x = A_{\mathrm{x}} = 0$. Notice that, according to (A7), this does not imply that entrainment variations are null [as it has been assumed in particular in (49) and (50)].

[1] B. P. Abbott *et al.* (LIGO Scientific and Virgo Collaborations), Phys. Rev. Lett. **119**, 161101 (2017).
[2] B. P. Abbott *et al.* (LIGO Scientific and Virgo Collaborations), Phys. Rev. Lett. **121**, 161101 (2018).
[3] D. Page, *Fifty Years of Nuclear BCS* (World Scientific, Singapore, 2013), p. 324–337.
[4] B. Haskell and A. Sedrakian, Astrophysics and Space Science Library **457**, 401 (2018).
[5] C. M. Espinoza, A. G. Lyne, B. W. Stappers, and M. Kramer, Mon. Not. R. Astron. Soc. **414**, 1679 (2011).
[6] P. W. Anderson and N. Itoh, Nature (London) **256**, 25 (1975).
[7] B. Haskell and A. Melatos, Int. J. Mod. Phys. D **24**, 1530008 (2015).
[8] M. A. Alpar, P. W. Anderson, D. Pines, and J. Shaham, Astrophys. J. **278**, 791 (1984).
[9] W. C. G. Ho, C. M. Espinoza, D. Antonopoulou, and N. Andersson, Sci. Adv. **1**, e1500578 (2015).
[10] P. M. Pizzochero, M. Antonelli, B. Haskell, and S. Seveso, Nat. Astron. **1**, 0134 (2017).
[11] O. Akbal, M. A. Alpar, S. Buchner, and D. Pines, Mon. Not. R. Astron. Soc. **469**, 4183 (2017).
[12] B. Haskell, V. Khomenko, M. Antonelli, and D. Antonopoulou, Mon. Not. R. Astron. Soc. **481**, L146 (2018).
[13] E. M. Kantor and M. E. Gusakov, Phys. Rev. D **83** (2011).
[14] A. I. Chugunov and M. E. Gusakov, Mon. Not. R. Astron. Soc. Lett. **418**, L54 (2011).
[15] J. Noronha and A. Sedrakian, Phys. Rev. D **77** (2008).
[16] B. Haskell, Phys. Rev. D **83** (2011).
[17] N. Andersson and K. D. Kokkotas, Mon. Not. R. Astron. Soc. **299**, 1059 (1998).
[18] L. Gualtieri, E. Kantor, M. Gusakov, and A. Chugunov, Phys. Rev. D **90** (2014).
[19] A. L. Watts and T. E. Strohmayer, Adv. Space Res. **40**, 1446 (2007).
[20] A. Passamonti and S. K. Lander, Mon. Not. R. Astron. Soc. **438**, 156 (2014).
[21] M. Gabler, P. Cerdá-Durán, N. Stergioulas, J. A. Font, and E. Müller, Mon. Not. R. Astron. Soc. **460**, 4242 (2016).
[22] W. I. Glaberson, W. W. Johnson, and R. M. Ostermeier, Phys. Rev. Lett. **33**, 1197 (1974).
[23] W. Guo, S. B. Cahn, J. A. Nikkel, W. F. Vinen, and D. N. McKinsey, Phys. Rev. Lett. **105**, 045301 (2010).
[24] D. Kivotides, J. Fluid Mech. **668**, 58 (2011).
[25] J. Gao, E. Varga, W. Guo, and W. F. Vinen, Phys. Rev. B **96**, 094511 (2017).
[26] D. Kivotides, Phys. Rev. Fluids **3**, 104701 (2018).
[27] M. Tsubota, T. Araki, and C. F. Barenghi, Phys. Rev. Lett. **90**, 205301 (2003).
[28] T. Sidery, N. Andersson, and G. L. Comer, Mon. Not. R. Astron. Soc. **385**, 335 (2008).
[29] C. Peralta, A. Melatos, M. Giacobello, and A. Ooi, Astrophys. J. **635**, 1224 (2005).
[30] C. A. van Eysden and B. Link, Astrophys. J. **865**, 60 (2018).
[31] C. E. Swanson, C. F. Barenghi, and R. J. Donnelly, Phys. Rev. Lett. **50**, 190 (1983).
[32] A. P. Finne, T. Araki, R. Blaauwgeers, V. B. Eltsov, N. B. Kopnin, M. Krusius, L. Skrbek, M. Tsubota, and G. E. Volovik, Nature (London) **424**, 1022 (2003).
[33] J. S. Tsakadze and S. J. Tsakadze, J. Low Temp. Phys. **39**, 649 (1980).
[34] C. A. van Eysden and A. Melatos, J. Low Temp. Phys. **165**, 1 (2011).
[35] H. E. Hall and W. F. Vinen, Proc. R. Soc. A **238**, 215 (1956).
[36] I. L. Bekarevich and I. M. Khalatnikov, Sov. Phys. JETP **13**, 643 (1961).
[37] N. Andersson and G. L. Comer, Classical Quantum Gravity **23**, 5505 (2006).
[38] A. Mastrano and A. Melatos, Mon. Not. R. Astron. Soc. **361**, 927 (2005).

[39] R. Prix, G. L. Comer, and N. Andersson, Astron. Astrophys. **381**, 178 (2002).
[40] N. Andersson, G. L. Comer, and R. Prix, Phys. Rev. Lett. **90**, 091101 (2003).
[41] K. Glampedakis and N. Andersson, Phys. Rev. Lett. **102**, 141101 (2009).
[42] N. Andersson, K. Glampedakis, and M. Hogg, Phys. Rev. D **87**, 063007 (2013).
[43] B. Link, Mon. Not. R. Astron. Soc. **422**, 1640 (2012).
[44] B. Link, Mon. Not. R. Astron. Soc. **421**, 2682 (2012).
[45] C. Peralta and A. Melatos, Astrophys. J. **701**, L75 (2009).
[46] C. Peralta, A. Melatos, M. Giacobello, and A. Ooi, Astrophys. J. **644**, L53 (2006).
[47] C. Peralta, A. Melatos, M. Giacobello, and A. Ooi, J. Fluid Mech. **609**, 221 (2008).
[48] A. Melatos and B. Link, Mon. Not. R. Astron. Soc. **437**, 21 (2014).
[49] K. Glampedakis, N. Andersson, and D. I. Jones, Phys. Rev. Lett. **100**, 081101 (2008).
[50] K. Glampedakis, N. Andersson, and D. I. Jones, Mon. Not. R. Astron. Soc. **394**, 1908 (2009).
[51] G. Mendell, Astrophys. J. **380**, 530 (1991).
[52] R. Prix, Phys. Rev. D **69**, 043001 (2004).
[53] N. Chamel, J. Low Temp. Phys. **189**, 328 (2017).
[54] N. Andersson, T. Sidery, and G. L. Comer, Mon. Not. R. Astron. Soc. **368**, 162 (2006).
[55] M. A. Alpar, S. A. Langer, and J. A. Sauls, Astrophys. J. **282**, 533 (1984).
[56] P. B. Jones, Mon. Not. R. Astron. Soc. **243**, 257 (1990).
[57] A. Sedrakian, Phys. Rev. D **71** (2005).
[58] P. B. Jones, Mon. Not. R. Astron. Soc. **257**, 501 (1992).
[59] R. I. Epstein and G. Baym, Astrophys. J. **387**, 276 (1992).
[60] V. Khomenko and B. Haskell, Pub. Astron. Soc. Aust. **35**, e020 (2018).
[61] V. Graber, A. Cumming, and N. Andersson, Astrophys. J. **865**, 23 (2018).
[62] N. Andersson, T. Sidery, and G. L. Comer, Mon. Not. R. Astron. Soc. **381**, 747 (2007).
[63] C. J. Gorter and J. H. Mellink, Physica (Utrecht) **15**, 285 (1949).
[64] N. Andersson and G. L. Comer, Classical Quantum Gravity **18**, 969 (2001).
[65] B. Carter, N. Chamel, and P. Haensel, Int. J. Mod. Phys. D **15**, 777 (2006).
[66] N. Andersson and G. L. Comer, Mon. Not. R. Astron. Soc. **328**, 1129 (2001).
[67] Neglecting A_x implies that we are implicitly assuming the internal energy to have the form $E = E_0 + \alpha_0 w_{\rm np}^2$, where E_0 and α_0 are the equilibrium values of E and α when there is no lag between the components. Physically, this means that we are working in the limit of small velocity lags.
[68] N. Chamel, Phys. Rev. C **85**, 035801 (2012).
[69] B. Haskell, N. Andersson, and A. Passamonti, Mon. Not. R. Astron. Soc. **397**, 1464 (2009).
[70] S. Seveso, P. M. Pizzochero, F. Grill, and B. Haskell, Mon. Not. R. Astron. Soc. **455**, 3952 (2016).
[71] M. Ruderman, T. Zhu, and K. Chen, Astrophys. J. **492**, 267 (1998).
[72] B. Link, Astron. Astrophys. **458**, 881 (2006).
[73] B. Link, Phys. Rev. Lett. **91**, 101101 (2003).
[74] The presence of a nonzero background lag may locally modify the vorticity direction. However, in our local analysis, the background lag is treated as locally uniform, while the local direction of the vorticity depends on the large scale, global arrangement of the background lag in the stationary configuration: we are therefore forced, due to the fact that the analysis is local, to assume three independent directions for the wave vector, the velocity lag, and the vorticity. However, in the following analysis, we keep the vorticity fixed along the z-axis (i.e., aligned with $\mathbf{\Omega}$). This assumption, as well as the fact that we will use $|\boldsymbol{\omega}| = 2\Omega$ in the background configuration, is not severe when the lag in angular velocity is small compared to the rotation rate of the star. Note that only the background vorticity is fixed, we account for variations in $|\boldsymbol{\omega}|$ in the mutual friction.
[75] C. Peralta, A. Melatos, M. Giacobello, and A. Ooi, Astrophys. J. **651**, 1079 (2006).
[76] K. Glampedakis, N. Andersson, and L. Samuelsson, Mon. Not. R. Astron. Soc. **410**, 805 (2011).

Monthly Notices of the ROYAL ASTRONOMICAL SOCIETY

MNRAS **496,** 5564–5574 (2020) doi:10.1093/mnras/staa1930
Advance Access publication 2020 July 06

The effect of non-linear mutual friction on pulsar glitch sizes and rise times

T. Celora [1]★ V. Khomenko,[2] M. Antonelli [2]★ and B. Haskell[2]★

[1]*Mathematical Sciences and STAG Research Centre, University of Southampton, Southampton SO17 1BJ, UK*
[2]*Nicolaus Copernicus Astronomical Center of the Polish Academy of Sciences, ul. Bartycka 18, PL-00-716 Warsaw, Poland*

Accepted 2020 June 30. Received 2020 June 17; in original form 2020 February 12

ABSTRACT

Observations of pulsar glitches have the potential to provide constraints on the dynamics of the high density interior of neutron stars. However, to do so, realistic glitch models must be constructed and compared to the data. We take a step towards this goal by testing non-linear models for the mutual friction force, which is responsible for the exchange of angular momentum between the neutron superfluid and the observable normal component in a glitch. In particular, we consider a non-linear dependence of the drag force on the relative velocity between superfluid vortices and the normal component, in which the contributions of both kelvin and phonon excitations are included. This non-linear model produces qualitatively new features, and is able to reproduce the observed bimodal distribution of glitch sizes in the pulsar population. The model also suggests that the differences in size distributions in individual pulsars may be due to the glitches being triggered in regions with different pinning strengths, as stronger pinning leads to higher vortex velocities and a qualitatively different mutual friction coupling with respect to the weak pinning case. Glitches in pulsars that appear to glitch quasi-periodically with similar sizes may thus be due to the same mechanisms as smaller events in pulsars that have no preferred glitch size, but simply originate in stronger pinning regions, possibly in the core of the star.

Key words: stars: neutron – pulsars: general – stars: rotation.

1 INTRODUCTION

Neutron stars (NSs) are promising environments in which to study physics in extreme conditions, and a significant amount of work has been devoted to using electromagnetic (see e.g. Bogdanov et al. 2019) and gravitational observations (Abbott et al. 2018) to constrain the equation of state (EOS) of dense matter in the interior of these objects. These studies are complementary to those that can be carried out with terrestrial experiments, as particle accelerators and heavy ion colliders cannot probe the high density and low temperature behaviour of the fundamental interactions, nor study the behaviour of matter with the large isospin asymmetries that characterize NS interiors (Haensel, Potekhin & Yakovlev 2007). In particular the neutrons are expected to be superfluid at such densities and temperatures (Chamel 2017; Haskell & Sedrakian 2018).

Pulsar glitches (sudden spin-ups observed in otherwise spinning down pulsars) are thought to represent a probe into the behaviour of the superfluid interior. Most models, in fact, assume that vortices in the superfluid are pinned (Anderson & Itoh 1975), either in the crust or core of the star, and that their sudden unpinning leads to rapid transfer of angular momentum and observed glitch (see e.g. Haskell & Melatos 2015). In these models the dissipative interaction between the superfluid and normal (observable) fluid is given by the so-called 'mutual friction' (Hall & Vinen 1956; Bekarevich & Khalatnikov 1961; Langlois, Sedrakian & Carter 1998; Andersson, Sidery & Comer 2006), which is mediated by the interaction between vortices and the normal component of the star and sets the observed coupling time-scale (Alpar & Sauls 1988).

Recent observations of glitches in Crab (Lyne et al. 2015; Shaw et al. 2018) and Vela (Palfreyman et al. 2018) pulsars have been used to obtain constraints on the mutual friction coefficients (Haskell et al. 2018; Ashton et al. 2019), which can shed light on the microscopic interaction occurring in the star and, ultimately, on the physical region the glitch is triggered. This is an interesting point, as calculations of entrainment parameters in the crust show that these may be very large (Carter, Chamel & Haensel 2006; Chamel 2012), i.e. there may be very few conduction neutrons in the crust, reducing the amount of angular momentum that can be exchanged and challenging a crustal interpretation of glitches (Andersson et al. 2012; Chamel 2013; Delsate et al. 2016). In this case, part of the core superfluid, in which neutron vortices can pin to proton flux tubes (Muslimov & Tsygan 1985; Srinivasan et al. 1990; Ruderman, Zhu & Chen 1998; Alpar 2017) may be involved, and glitch observations could be used to constrain superfluid gap models, pinning forces and the EOS (Ho et al. 2015; Pizzochero et al. 2017; Montoli, Antonelli & Pizzochero 2020b).

Furthermore, the distribution of glitch sizes appears to be bimodal (Fuentes et al. 2017), and some pulsars, such as Vela and the X-ray pulsar J0537-6910 appear to have mostly large glitches that occur quasi periodically (Antonopoulou et al. 2018), as opposed to most other pulsars for which the size distribution is consistent with a power law and the waiting time distribution with an exponential (Melatos & Peralta 2007; Howitt, Melatos & Delaigle 2018). This difference is also likely to be the hallmark of different physical regimes of the process (Fulgenzi, Melatos & Hughes 2017) and possibly due to

★ E-mail: T.Celora@soton.ac.uk (TC); antonelli@camk.edu.pl (MA); antonelli@camk.edu.pl (BH)

glitches originating in different physical regions of the star (Haskell & Antonopoulou 2014).

A careful determination of mutual friction parameters in the core and crust of the star, and a study of the system's hydrodynamical response is crucial in order to make theoretical predictions. In the core of the star mutual friction is thought to be mainly due to electron scattering off magnetized vortex cores (Alpar, Langer & Sauls 1984), while in the crust energy is dissipated mainly by phonon excitations of the lattice (Jones 1990a) and kelvin excitations of the vortices themselves (Epstein & Baym 1992; Jones 1992), which can also occur when vortices cross flux tubes in the core (Ruderman et al. 1998; Link 2003; Glampedakis, Andersson & Samuelsson 2011). Significant uncertainties still remain in the determination of crustal mutual friction parameters, which in turn impact on predictions of the glitch rise time and observed size (Haskell, Pizzochero & Sidery 2012; Antonelli & Pizzochero 2017; Sourie et al. 2017). A recent step forward was taken by Graber, Cumming & Andersson (2018) who, following the approaches of Epstein & Baym (1992) and Jones (1992), calculated the kelvin friction parameters at different densities in the crust and compared the results to Vela glitches.

In this paper we include an additional ingredient in the calculation which, we show, has a strong impact, both qualitative and quantitative, on the glitch features, namely the dependence of the mutual friction parameters on the relative velocity between superfluid vortices and the normal component. This issue is of fundamental importance in the crust, as kelvin mutual friction depends strongly on the relative velocity (Epstein & Baym 1992; Jones 1992) and is suppressed for low velocities, at which phonon contributions dominate (Jones 1990a; Jones 1990b). If vortices unpin and initially move at large velocities, they will thus experience a varying drag as the system relaxes towards equilibrium. The problem is, however, of more general relevance, as relative motions between the superfluid and normal components may lead to turbulence (Peralta et al. 2006; Andersson, Sidery & Comer 2007) and also to a different velocity dependence of the mutual friction parameters, as is, for example, well known for objects falling through the atmosphere on Earth, for which the terminal velocity can be obtained by considering a drag that scales with the square of the velocity, rather than linearly as would be expected if the air flow were laminar.

In the following we first examine the problem of mutual friction in the case of velocity-dependent parameters, and discuss the different possible physical regimes. We then move on to discuss the mutual friction in the crust of a neutron star, and present a model which includes both kelvin and phonon contributions. We show that this model predicts a qualitatively different rise than standard mutual friction models, which is consistent with recent observations of a glitch in the Vela pulsar (Palfreyman et al. 2018; Ashton et al. 2019). We also apply the model to a population of glitching pulsars and show that it produces a bimodal glitch size population that has an excess of large glitches.

2 MUTUAL FRICTION: LINEAR DRAG IN ABSENCE OF TURBULENCE

Let us begin our analysis by reviewing the standard derivation of the mutual friction force in neutron stars (Mendell 1991; Carter & Chamel 2005; Andersson et al. 2006). Following Prix, Comer & Andersson (2002), we deal with a system composed of a charge neutral mixture of protons and electrons and everything coupled to it on short time-scales (so that we can treat them as a single component, the 'normal' one hereafter dubbed 'p') plus a superfluid neutron component (hereafter dubbed 'n') which, due to the stellar rotation, is threaded by an array of quantized vortices.

In the absence of interactions between the superfluid and the normal component, the vortex line velocity $\boldsymbol{v_L}$ is equal to the bulk velocity $\boldsymbol{v_n}$ of the neutrons (where both $\boldsymbol{v_L}$ and $\boldsymbol{v_n}$ are orthogonal to the vortex line, see e.g. Donnelly 1991). This result can be understood by analysing the forces acting on a vortex, which to a very good degree of approximation can be treated as a massless object (Baym & Chandler 1983; Sonin 1987; Donnelly 1991), although see Simula (2018) for a recent discussion on the effective mass of a quantum vortex. In this case the only force acting on a free vortex line is the Magnus force $\mathbf{f}_M$ per unit length of vortex,

$$f_M^i = \rho_{\rm n}\varepsilon^{ijk}\kappa_j\left(v_k^{\rm L} - v_k^{\rm n}\right), \tag{1}$$

where $\boldsymbol{\rho}_{\rm n}$ is the density of neutrons and $\boldsymbol{\kappa}$ is a vector aligned locally with the vorticity, such that $\boldsymbol{\kappa} = \kappa\,\hat{\boldsymbol{\kappa}}$ and $\boldsymbol{\kappa}= h/2m_{\rm n}$ is the quantum of circulation. The requirement of force balance leads to $\mathbf{f}_M = 0$ and thus $\boldsymbol{v_L} = \boldsymbol{v_n}$. In the more general case in which the vortices interact also with the normal component flowing with velocity $\boldsymbol{v_p}$, the vortex velocity $\boldsymbol{v_L}$ will in general differ from both $\boldsymbol{v_n}$ and $\boldsymbol{v_p}$.

If we describe the dissipative interaction between the vortices and the normal component in terms of a linear drag force, the equation of motion of a single vortex line is

$$f_M^i + f_D^i = 0, \tag{2}$$

with the drag force per unit length defined as:

$$f_D^i = -\eta\left(v_{\rm L}^i - v_{\rm p}^i\right). \tag{3}$$

The drag coefficient η is related to the dimensionless quantity $\mathcal{R}$ often used in the literature via $\mathcal{R} = \eta/\kappa\rho_{\rm n}$. It is useful to work in the normal component rest frame where the equation (2) reads

$$\hat{\boldsymbol{\kappa}} \times (\mathbf{v}_{\rm Lp} - \mathbf{v}_{\rm np}) - \mathcal{R}\mathbf{v}_{\rm Lp} = 0. \tag{4}$$

We can solve this equation to write the vortex velocity $\mathbf{v}_{\rm Lp} = \mathbf{v}_{\rm L} - \mathbf{v}_{\rm p}$ in terms of the lag $\mathbf{v}_{\rm np} = \mathbf{v}_{\rm n} - \mathbf{v}_{\rm p}$, namely

$$\mathbf{v}_{\rm Lp} = -\frac{\mathcal{R}}{1+\mathcal{R}^2}\,\hat{\boldsymbol{\kappa}} \times \mathbf{v}_{\rm np} - \frac{1}{1+\mathcal{R}^2}\,\hat{\boldsymbol{\kappa}} \times (\hat{\boldsymbol{\kappa}} \times \mathbf{v}_{\rm np}). \tag{5}$$

In the limit of 'weak drag', $\mathcal{R} \ll 1$, one can neglect the first term to get $\mathbf{v}_{\rm Lp} \approx -\hat{\boldsymbol{\kappa}} \times (\hat{\boldsymbol{\kappa}} \times \mathbf{v}_{\rm np})$, as expected for the no-drag case. On the other hand, if we consider the 'super strong drag' regime, that is $\mathcal{R} \gg 1$, the previous equation gives $\mathbf{v}_{\rm Lp} \approx 0$, implying that the vortex is effectively pinned.

Now, the force per unit volume acting between the normal component and the superfluid is found by averaging over all the vortices in the fluid element, or rather over the total length of vortex lines L in the element. In general this depends on the nature of the flow, as a turbulent flow can tangle the vortices and increase the length of vortex in an element (Vinen 1957; Schwarz 1988). We will discuss this possibility in the following sections. In the case of an array of straight and aligned vortices, it is possible to introduce the vortex density n_v on a unit surface orthogonal to $\hat{\boldsymbol{\kappa}}$ and use it to get the averaged force per volume element. Then, using Newton's third law, the force per unit volume between the vortices and the fluids can be included in the hydrodynamical equations (the full form will be given in equation 34) as

$$\begin{aligned}\rho_n\partial_t\mathbf{v}_n + \ldots &= -n_v\,\mathbf{f}_M\\ \rho_p\partial_t\mathbf{v}_p + \ldots &= -n_v\,\mathbf{f}_D.\end{aligned} \tag{6}$$

From equation (6) we can read the mutual friction force $\mathbf{F}_{\rm MF}$, defined as the force exerted by the normal component on the superfluid,

namely

$$F^i_{\rm MF} = -n_v\, f^i_M = n_v\, f^i_D, \tag{7}$$

where the vortex density n_v can be seen as a measure of the macroscopic vorticity $\omega^i_{\rm n}$ vector via

$$\omega^i_{\rm n} = m_{\rm n}^{-1}\, \varepsilon^{ijk}\, \partial_j\, p^{\rm n}_k = \kappa\, n_v\, \hat{\kappa}^i. \tag{8}$$

Therefore, the mutual friction force can be written in such a way that only macroscopic hydrodynamical quantities appear (Andersson et al. 2006)

$$\mathbf{F}_{\rm MF} = \rho_{\rm n}(\mathcal{B}_c\, \boldsymbol{\omega}_n \times \mathbf{v}_{\rm np} + \mathcal{B}_d\, \hat{\boldsymbol{\omega}}_n \times (\boldsymbol{\omega}_n \times \mathbf{v}_{\rm np})), \tag{9}$$

where $\hat{\boldsymbol{\omega}}_n = \hat{\boldsymbol{\kappa}}$ and

$$\mathcal{B}_c = \frac{\mathcal{R}^2}{1+\mathcal{R}^2} \qquad \mathcal{B}_d = \frac{\mathcal{R}}{1+\mathcal{R}^2}. \tag{10}$$

Therefore, the mutual friction force is composed of a Coriolis-like part which is proportional to $\mathcal{B}_c$, and a dissipative part proportional to $\mathcal{B}_d$.

3 VORTEX MOTION WITH NON-LINEAR DRAG

In this section we consider the more general case of a non-linear drag force. In the standard picture, presented in the previous section, the drag parameter $\mathcal{R}$ is taken to be a constant, which can be estimated via microphysical calculations of energy dissipation rates in specific channels. For instance, in the NS crust, for some relatively high values of the vortex velocity $v_{\rm Lp} \gtrapprox 10^4$ cm s^{-1}, energy is dissipated mainly by Kelvin waves propagating along the vortex line (Epstein & Baym 1992). On the other hand, for lower vortex velocities the Kelvin waves are suppressed and energy is dissipated via excitation of phonons in the crustal lattice (Jones 1990a). Hence, the drag parameter $\mathcal{R}$ itself depends on $|v_{\rm Lp}|$ (see Jones 1992). As a result, we are interested in dealing with the more general case in which the additional dependence of the drag force on the relative speed $|\mathbf{v}_{\rm Lp}|$ is encoded in $\tilde{\mathcal{R}}$,

$$f^i_D = -\rho_{\rm n}\, \kappa\, \tilde{\mathcal{R}}\, v^i_{\rm Lp}, \qquad \tilde{\mathcal{R}} = \tilde{\mathcal{R}}(|\mathbf{v}_{\rm Lp}|). \tag{11}$$

Of course, the linear drag case is recovered once $\tilde{\mathcal{R}}$ is assumed to be a constant.

While the case we are explicitly considering is that of a straight vortex array and a velocity-dependent drag parameter $\tilde{\mathcal{R}}$, so that the mutual friction force can be written

$$F^i_{\rm MF} = -n_v \rho_{\rm n}\, \kappa\, \tilde{\mathcal{R}}\, v^i_{\rm Lp} \tag{12}$$

this is mathematically equivalent to considering a turbulent tangle of vortices, with vortex length per unit volume $\tilde{L} = \tilde{L}(|\mathbf{v}_{\rm Lp}|)$. In this latter case, the mutual friction force takes the form

$$F^i_T = -\tilde{L} \rho_{\rm n}\, \kappa\, \mathcal{R}\, v^i_{\rm Lp}\,, \tag{13}$$

which is formally the same as equation (12). The conclusions we will obtain in the following for different functional dependence of $\tilde{\mathcal{R}}$ on the vortex line velocity can thus be directly applied to the case in which $\tilde{L}$ has the same dependence, so that e.g. the qualitative behaviour of the coupling for $\tilde{\mathcal{R}} \propto |\mathbf{v}_{\rm Lp}|^2$ can be applied to the standard case of fully developed isotropic quantum turbulence as well, in which $\tilde{L} \propto |\mathbf{v}_{\rm Lp}|^2$ (Vinen 1957; Andersson et al. 2007).

To proceed it is useful to introduce the usual cylindrical coordinates system $(\hat{e}_x, \hat{e}_\varphi, \hat{e}_z)$ where the z-axis is aligned with the vortices, i.e. $\hat{\boldsymbol{\kappa}} = \hat{e}_z$. We also consider the velocities of the two components to be azimuthal, so that $\mathbf{v}_{\rm np} = x\, \Omega_{\rm np} \hat{e}_\varphi$. On the time-scales of the observable glitch dynamics this is true for a fluid element (at least on average), and allows us to simplify the analysis. However, on shorter time-scales vortex accumulation (Khomenko & Haskell 2018) and counterflow along the axis of a vortex due to bending (Khomenko, Antonelli & Haskell 2019) may give rise to instabilities leading to turbulence or vortex avalanches.

In components, the force balance equation (2) gives

$$\begin{aligned} v^\varphi_{\rm Lp} - v^\varphi_{\rm np} + \tilde{\mathcal{R}}\, v^x_{\rm Lp} &= 0 \\ v^x_{\rm Lp} - \tilde{\mathcal{R}}\, v^\varphi_{\rm Lp} &= 0, \end{aligned} \tag{14}$$

that can be rearranged as

$$v^x_{\rm Lp} = \frac{\tilde{\mathcal{R}}}{1+\tilde{\mathcal{R}}^2} v^\varphi_{\rm np} = \mathcal{B}_{MF}\, v^\varphi_{\rm np}. \tag{15}$$

This expression is only formal since we have that the drag parameter $\tilde{\mathcal{R}}$ still has an implicit dependence on $|\mathbf{v}_{\rm Lp}|$. The solution in equation (15) also defines the mutual friction coefficient $\mathcal{B}_{MF}$, which is introduced in such a way that it reduces to $\mathcal{B}_d$ in the linear drag case (when $\tilde{\mathcal{R}}$ is a constant).

The last equation we need is the azimuthal component of the vortex line velocity,

$$v^\varphi_{\rm Lp} = \frac{v^\varphi_{\rm np}}{1+\tilde{\mathcal{R}}^2}. \tag{16}$$

Combining equations (15) and (16) we obtain

$$|\mathbf{v}_{\rm Lp}| = \frac{|\mathbf{v}_{\rm np}|}{\sqrt{1+\tilde{\mathcal{R}}^2}} \tag{17}$$

which, given a functional dependence of $\tilde{\mathcal{R}}^2$ on $|\mathbf{v}_{\rm Lp}|$, can be solved to eliminate the vortex line velocity from the hydrodynamical equations in equation (6). We will analyse specific forms of the mutual friction in the following, but let us note here that equation (17) shows that the difference between $|\mathbf{v}_{\rm Lp}|$ and $|\mathbf{v}_{\rm np}|$ is of $\mathcal{O}(\tilde{\mathcal{R}}^2)$, so that to very good approximation one can take $|\mathbf{v}_{\rm Lp}| \approx |\mathbf{v}_{\rm np}|$ for $\tilde{\mathcal{R}} \ll 1$, and simply solve the hydrodynamical equations in equation (6) directly for $\tilde{\mathcal{R}}(|\mathbf{v}_{\rm Lp}|) \approx \tilde{\mathcal{R}}(|\mathbf{v}_{\rm np}|)$ (or equivalently, if dealing with turbulence, for $\tilde{L}(|\mathbf{v}_{\rm Lp}|) \approx \tilde{L}(|\mathbf{v}_{\rm np}|)$).

3.1 Power-law drag

Let us start with a simple prescription, and consider a power-law behaviour for the drag force,

$$f^i_D = -\eta_\beta\, |\mathbf{v}_{Lp}|^\beta\, v^i_{Lp}\,, \tag{18}$$

where the physical dimension of the viscous parameter η_β depends on the explicit value of β. Despite its simplicity, this prescription is applicable to several physical setups. For example, in the presence of classical turbulence one has $\beta = 1$ (the standard case of objects moving in a fluid at high Reynolds number, according to Newton's drag law), and for isotropic quantum turbulence $\beta = 2$, although polarized turbulence is likely to require the use of multiple power laws to describe the drag (Andersson et al. 2007; Mongiovì & Jou 2007). Negative values of β do not have an hydrodynamical interpretation, but microphysical calculations of Kelvin drag in the crust (Epstein & Baym 1992; Jones 1992; Graber et al. 2018) and also core of the star if the protons are in a type-II superconducting state (Link 2003; Haskell, Glampedakis & Andersson 2014), suggest that $\beta = -3/2$: this case is of particular interest for NSs and will be considered in detail in the following.

To work with a dimensionless drag parameter $\mathcal{R}$ we introduce a microscopic parameter v_0 (with the dimension of a velocity) and

rewrite the drag force in equation (18) as

$$f_D^i = -\kappa\,\rho_n\,\mathcal{R}\left(\frac{|\mathbf{v}_{Lp}|}{v_0}\right)^{\beta} v_{Lp}^i, \tag{19}$$

where the constant and dimensionless drag parameter is $\mathcal{R} = \eta_\beta\, v_0^\beta/\kappa\,\rho_n$. In terms of the drag coefficient $\tilde{\mathcal{R}}$ previously introduced we have that

$$\tilde{\mathcal{R}} = \left(\frac{|\mathbf{v}_{\rm Lp}|}{v_0}\right)^{\beta} \mathcal{R}. \tag{20}$$

Now, to solve the equations of motion for the vortex line it is helpful to introduce the dimensionless variables

$$s = \frac{v_{Lp}^\varphi}{|\mathbf{v}_{\rm Lp}|}, \quad \sqrt{1-s^2} = \frac{v_{\rm Lp}^x}{|\mathbf{v}_{\rm Lp}|} \tag{21}$$

and

$$\chi_L = \frac{|\mathbf{v}_{Lp}|}{v_0}, \quad \chi_{np} = \frac{|\mathbf{v}_{np}|}{v_0} \tag{22}$$

so to rewrite equation (14) as

$$\begin{aligned} s\,\chi_L - \chi_{np} + \mathcal{R}\sqrt{1-s^2}\,\chi_L^{\beta+1} &= 0 \\ \sqrt{1-s^2} - \mathcal{R}\,\chi_L^{\beta}\,s &= 0. \end{aligned} \tag{23}$$

Note that $s = \cos(\theta_D)$, where θ_D is the 'dissipation angle' introduced by Epstein & Baym (1992), see also Link (2014). Starting from equation (14) one can show that

$$\begin{aligned} \chi_L &= s\,\chi_{np} \\ \mathcal{R}^2\,\chi_{np}^{2\beta}\,s^{2\beta+2} + s^2 - 1 &= 0. \end{aligned} \tag{24}$$

Since $0 \le s \le 1$, namely $0 \le \theta_D \le \pi/2$, we see that the lag between the vortices and the normal component must always be smaller than the lag between the neutron (n) and normal (p) component. It is also interesting to observe that, since $\tilde{\mathcal{R}} = \mathcal{R}\,\chi_{\rm np}^{\beta}\,s^{\beta}$, the mutual friction coefficient $\mathcal{B}_{MF}$ introduced in equation (15) reads

$$\mathcal{B}_{MF} = s\sqrt{1-s^2} = \frac{1}{2}\sin(2\theta_D). \tag{25}$$

Different values of β correspond to different phenomenological models for the dynamics of vortex lines and the evolution of the system will depend on the choice for the index β.

To better discuss this point, let us first remark that it is always possible to choose v_0 such that $\mathcal{R} = 1$, implying $\tilde{\mathcal{R}} \approx 1$ when $|\mathbf{v}_{Lp}| \approx v_0$ (this regime corresponds to the largest possible value for the mutual friction parameter, $\mathcal{B}_{MF} = 1/2$). This value of v_0 defines three velocity ranges $|\mathbf{v}_{Lp}| \ll v_0$, $|\mathbf{v}_{Lp}| \approx v_0$ and $|\mathbf{v}_{Lp}| \gg v_0$, that are related to three mutual friction regimes. This is sketched, for different prescriptions of β, in Fig. 1, where we show the dependence of the effective drag parameter $\tilde{\mathcal{R}}$ on $|\mathbf{v}_{Lp}|$, having chosen a fixed value of $\tilde{\mathcal{R}} = 1$ for $|\mathbf{v}_{Lp}| = v_0$.

According to equation (24), the vortex velocity $|\mathbf{v}_{Lp}|$ decreases as the two components recouple during the spin-up phase of a glitch, simply because the initial lag is decreasing as well.

For $\beta < 0$ and an initial velocity $|\mathbf{v}_{Lp}| > v_0$, the drag increases as the two components recouple and rapidly enters the strong $\tilde{\mathcal{R}} \approx 1$ regime, as we can see for the $\beta = -3/2$ case which is relevant for kelvin mutual friction. If during the recoupling process the lag becomes so small that $|\mathbf{v}_{Lp}| < v_0$, we enter the 'super-strong' drag regime, where $\tilde{\mathcal{R}}$ diverges. In this regime the friction coefficient goes to zero as $\mathcal{B}_{MF} \sim \tilde{\mathcal{R}}^{-1}$, so that a negative β could be used to mimic the repinning process, namely a suppression of the mutual friction.

For $\beta > 0$ the opposite is true, and the coupling strength decays (more or less rapidly depending on the actual value of β) as the lag decreases. Such a model, for initial conditions such that $|\mathbf{v}_{Lp}| > v_0$, could be used to describe phenomenologically a situation in which a pinned vortex configuration undergoes unpinning, passes through a phase of strong drag (in which the recoupling of the components is very fast) and possibly a final part in which $|\mathbf{v}_{Lp}| \ll v_0$ and the recoupling proceeds with a much slower time-scale.

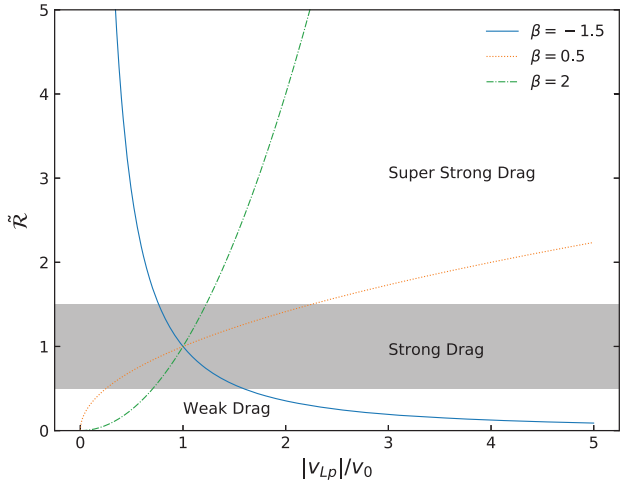

Figure 1. Qualitative plot of the drag parameter $\tilde{\mathcal{R}}$ as a function of $|\mathbf{v}_{Lp}|/v_0$, for different values of β and having chosen a fixed value of $\tilde{\mathcal{R}} = 1$ for $|\mathbf{v}_{Lp}| = v_0$. Three regions are highlighted, the 'weak drag' region in which $\mathcal{B}_{MF} \sim \tilde{\mathcal{R}}$, the 'strong drag' region in which $\mathcal{B}_{MF} \lesssim 1/2$ and a 'super strong drag' one where the mutual friction goes to zero as $\mathcal{B}_{MF} \sim \tilde{\mathcal{R}}^{-1}$. Therefore, a drag force described by a power law with a negative β can be used to model the effect of initially free vortices repinning. For positive values of β the opposite is true, and the coupling becomes weak as $|\mathbf{v}_{Lp}|$ decreases. For the case $\beta = 2$, which describes mutual friction in an isotropic turbulent tangle, the drag is initially strong, but rapidly decreases as the recoupling proceeds.

In fact the power-law prescription in equation (18) can be used to model transitions between different dynamical regimes at different relative vortex velocities. If, for example, one has two microscopic estimates $\mathcal{R}_1$ and $\mathcal{R}_2$ for the drag parameter in two different regimes such that

$$\begin{aligned} \tilde{\mathcal{R}}(\mathbf{v}_{Lp} \approx v_1) \approx \mathcal{R}_1 &= \mathcal{R}\left(\frac{v_1}{v_0}\right)^{\beta} \\ \tilde{\mathcal{R}}(\mathbf{v}_{Lp} \approx v_2) \approx \mathcal{R}_2 &= \mathcal{R}\left(\frac{v_2}{v_0}\right)^{\beta}, \end{aligned} \tag{26}$$

we may interpolate between the two values using a power-law approximation for the drag with exponent

$$\beta_{12} = \frac{\log(\mathcal{R}_2/\mathcal{R}_1)}{\log(v_2/v_1)}. \tag{27}$$

The final interpolated drag function reads

$$\tilde{\mathcal{R}} = \mathcal{R}_1\left(\frac{|\mathbf{v}_{Lp}|}{v_1}\right)^{\beta_{12}} = \mathcal{R}_2\left(\frac{|\mathbf{v}_{Lp}|}{v_2}\right)^{\beta_{12}}. \tag{28}$$

As a result, the choice of a non-linear drag being a simple power law may be used for modelling the transition between different effective drag regimes related to the activation of different dissipation channels. It can also be used as a simple model for the repinning process: we can in fact set one of the two values of $\mathcal{R}$ very large at small lags so to mimic an effective repinning.

3.2 Realistic drag in the crust

We now use the methods developed in the previous sections to construct a non-linear model for superfluid drag in the NS crust. Graber et al. (2018) have computed the drag coefficient resulting from Kelvin wave excitations: their estimate of the drag coefficient depends on the typical relative velocity as $\tilde{\mathcal{R}} \propto |v_{\rm Lp}|^{-3/2}$. On the other hand, Jones (1990a) has shown that Kelvin processes are suppressed below $|v_{\rm Lp}| \lesssim 500\,{\rm cm\,s^{-1}}$, and that at even lower vortex velocities $|v_{Lp}| \approx 1\,{\rm cm\,s^{-1}}$ the main contribution to the drag comes from phonon excitations, leading to a constant coefficient $\mathcal{R} = 10^{-5}$.

Since phonon excitations give rise to a drag coefficient which is lower than the Kelvin one, a realistic model that interpolates between the two behaviours should reduce to

$$\begin{aligned}
\tilde{\mathcal{R}} &\approx \mathcal{R}_1 \left(\frac{|\mathbf{v}_{\rm Lp}|}{v_1}\right) && \text{for } v_{\rm Lp} \approx v_1 \ll 500\,{\rm cm\,s^{-1}} \\
\tilde{\mathcal{R}} &\approx \mathcal{R}_2 \left(\frac{|\mathbf{v}_{\rm Lp}|}{v_2}\right)^{-3/2} && \text{for } v_{\rm Lp} \approx v_2 \gg 500\,{\rm cm\,s^{-1}},
\end{aligned} \tag{29}$$

where v_1 and v_2 are respectively the typical velocities for which the phonon and kelvin excitations are dominant. We choose the simplest linear dependence to get a smooth interpolation between the two channels and the values $\mathcal{R}_1$ and $\mathcal{R}_2$ are determined from microphysical calculations of phonon and kelvin drag parameters for $v_{\rm Lp} \approx v_1$ and $v_{\rm Lp} \approx v_2$ respectively. We note that Gügercinoğlu & Alpar (2020) interpret the result of Graber et al. (2018) differently and that results in an exponent for the Kelvin-drag regime of $-1/2$. Since our model is purely phenomenological, this can be easily adjusted in our prescription.

For our estimate of crustal drag forces we take the constant[1] values $v_1 = 1\,{\rm cm\,s^{-1}}$, with $\mathcal{R}_1 = 10^{-5}$ and $v_2 = 10^4\,{\rm cm\,s^{-1}}$, for which we set $\mathcal{R}_2 = 10^{-3}$. Since there are two power-law regimes, we model the transition between them[2] by writing the total drag coefficient as

$$\tilde{\mathcal{R}} = \left(\mathcal{R}_1^{-1}\left(\frac{|\mathbf{v}_{\rm Lp}|}{v_1}\right)^{-1} + \mathcal{R}_2^{-1}\left(\frac{|\mathbf{v}_{\rm Lp}|}{v_2}\right)^{3/2}\right)^{-1}, \tag{30}$$

which is shown as a function of $|\mathbf{v}_{\rm Lp}|$ in Fig. 2. Let us stress that the choice of the crossover velocities v_1 and v_2 agrees with microphysical estimates (Jones 1990a; Graber et al. 2018), but remains, nevertheless, rather uncertain. However, simulations of interactions between vortices and ions in the crust (Wlazlowski et al. 2016) and flux tubes in the core (Drummond & Melatos 2017, 2018) are becoming feasible and more stringent constraints on these parameters may become available in the future.

Introducing dimensionless quantities as in the previous subsection, via equation (21) and taking

$$\chi_L^{(i)} = \frac{|\mathbf{v}_{\rm Lp}|}{v_i}, \quad \chi_{np}^{(i)} = \frac{|\mathbf{v}_{\rm np}|}{v_i} \quad \text{for } i = 1, 2 \tag{31}$$

[1]Clearly, the parameters $\mathcal{R}_2$ and v_2 vary with density, while here we are not doing so because the glitch model will be rigid (the angular velocity will not depend on the x and z coordinates). Hence, we choose the value of $\mathcal{R}_2$ and v_2 according to model-A presented in Graber et al. (2018): model-A is the only one for which the estimated value of v_2 lies in the validity regime of kelvonic drag throughout all the crust, namely $v_2 > 10^2\,{\rm cm\,s^{-1}}$. According to this model, the value of v_2 varies, while $\mathcal{R}_2$ is almost constant throughout the whole crust.

[2]To avoid unnecessary confusion, let us note that this interpolation is not related to the one introduced at the end of Section 3.1.

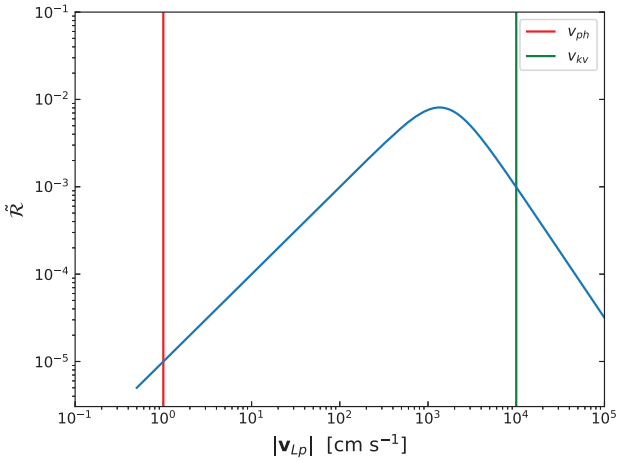

Figure 2. Form of the $\tilde{\mathcal{R}}$ as a function of $|\mathbf{v}_{\rm Lp}|$ where $\mathcal{R}_1 = 10^{-5}$, $\mathcal{R}_2 = 10^{-3}$, $v_1 = 1\,{\rm cm\,s^{-1}}$ and $v_2 = 10^4\,{\rm cm\,s^{-1}}$. Since here $\tilde{\mathcal{R}} \ll 1$ we have $\mathcal{B}_{MF} \approx \tilde{\mathcal{R}}$, so that the figure shows with a good accuracy also the behaviour of the mutual friction parameter.

where i labels the two crossover velocities, we can write equation (14) as

$$\begin{aligned}
&\sqrt{1-s^2} - \left(\mathcal{R}_1^{-1}\chi_L^{(1)\,-1} + \mathcal{R}_2^{-1}\chi_L^{(2)\,3/2}\right)^{-1} s = 0, \\
&s\,\chi_L^{(i)} - \chi_{np}^{(i)} + \left(\mathcal{R}_1^{-1}\chi_L^{(1)\,-1} + \mathcal{R}_2^{-1}\chi_L^{(2)\,3/2}\right)^{-1} \sqrt{1-s^2}\,\chi_L^{(i)} = 0.
\end{aligned} \tag{32}$$

It is then shown that $|v_{\rm Lp}| \leq |v_{\rm np}|$ is still valid, namely $\chi_L^{(i)} = s\,\chi_{\rm np}^{(i)}$. Hence, it is easy to recast equation (32) as

$$\left(\frac{1}{\mathcal{R}_1}\left(s\,\chi_{np}^{(1)}\right)^{-1} + \frac{1}{\mathcal{R}_2}\left(s\,\chi_{np}^{(1)}\frac{v_1}{v_2}\right)^{3/2}\right)^{-2} s^2 + s^2 - 1 = 0\,. \tag{33}$$

This equation can now be integrated together with the fluid equations for the system, which we will present in the next section.

4 GLITCH MODEL

Having determined the model for the mutual friction, we investigate its effect on pulsar glitch dynamics. To do this we start from the full equations of motion for the neutron superfluid (n) and normal component (p), which can be written as

$$\begin{aligned}
&\left(\partial_t + v_{\rm x}^j\nabla_j\right)\left(v_i^{\rm x} + \varepsilon_{\rm x}\,w_i^{\rm yx}\right) + \nabla_i\left(\mu_{\rm x} + \phi\right) \\
&\qquad + \varepsilon_{\rm x}\,w_{\rm yx}^i\nabla_i v_j^{\rm x} = f_i^{\rm x}/\rho_{\rm x},
\end{aligned} \tag{34}$$

where x and y label the chemical component (i.e. x, y = n, p), $\varepsilon_{\rm x}$ is the entrainment parameter, $\mu_{\rm x}$ is the chemical potential per unit mass of the substance x, ϕ is the gravitational potential and $w_i^{\rm yx} = v_i^{\rm y} - v_i^{\rm x}$ is the relative velocity (see e.g. Prix (2004) and Andersson & Comer (2006)). To build a rigid glitch model we assume axial symmetry (i.e. no dependence on the azimuthal angle φ) and we take the ansatz, with x the cylindrical radius,

$$\mathbf{v}_{\rm n} = x\,\Omega_n(t)\,\hat{e}_\varphi, \quad \mathbf{v}_{\rm p} = x\,\Omega_p(t)\,\hat{e}_\varphi. \tag{35}$$

With this assumption the two fluids equations reduce to

$$\begin{aligned}
&\partial_t\,v_i^{\rm n} + \varepsilon_{\rm n}\partial_t\left(v_i^{\rm p} - v_i^{\rm n}\right) + \nabla_i\left(\mu_{\rm n} + \phi\right) = f_i^{\rm n}/\rho_{\rm n} \\
&\partial_t\,v_i^{\rm p} + \varepsilon_{\rm p}\partial_t\left(v_i^{\rm n} - v_i^{\rm p}\right) + \nabla_i\left(\mu_{\rm p} + \phi\right) = f_i^{\rm p}/\rho_{\rm p}.
\end{aligned} \tag{36}$$

The ansatz equation (35) implies that the non-azimuthal components of the two fluid equations in equation (34) are not dynamical (they

represent the hydrostatic equilibrium that sets the structure of the star) and that the continuity equations for the two species are automatically satisfied (Antonelli & Pizzochero 2017).

The force density that enters the two fluid equations is the mutual friction force,

$$f_i^{\rm n}/\rho_{\rm n} = F_i^{\rm MF}/\rho_{\rm n} = -\varepsilon_{ijk}\,\omega_{\rm n}^j\,\left(v_{\rm L}^k - v_{\rm n}^k\right). \tag{37}$$

Because of the presence of the vorticity $\omega_{\rm n}^i$ in the mutual friction, it is sometimes useful to perform a change of variables and define a new angular velocity given by

$$\Omega_v = (1-\varepsilon_{\rm n})\,\Omega_{\rm n} + \varepsilon_{\rm n}\,\Omega_{\rm p}. \tag{38}$$

This quantity is just a variable related to the superfluid momentum that can be used in place of $\Omega_{\rm n}$ and merely represents the total amount of vortices present within the cylindrical radius x via the Feynman-Onsager relation. As a result, the equations of motion in equation (36) read

$$\begin{aligned}\dot{\Omega}_v &= -2\,\Omega_v\,\frac{v_L^x}{x},\\ \left(\rho_{\rm p} - \frac{\varepsilon_{\rm n}\,\rho_{\rm n}}{1-\varepsilon_{\rm n}}\right)\dot{\Omega}_{\rm p} + \frac{\rho_{\rm n}}{1-\varepsilon_{\rm n}}\,\dot{\Omega}_v &= 0,\end{aligned} \tag{39}$$

where we exploited equation (8), namely the fact that

$$\boldsymbol{\omega}_n = \frac{1}{m_{\rm n}}\nabla\times\mathbf{p}_{\rm n} = 2\Omega_v\,\hat{e}_z. \tag{40}$$

These are the equations for a two component rigid glitch model, where the first is a continuity equation for the vortex number (cfr equation (13) of Antonelli & Pizzochero 2017) while the second is just the angular momentum conservation (i.e. it is equivalent to $\rho_{\rm n}\dot{\Omega}_{\rm n} + \rho_{\rm p}\dot{\Omega}_{\rm p} = 0$). More precisely, to obtain a well-defined averaged rigid model we should average the equations over the whole star, so that the second equation in equation (39) expresses the conservation of the total angular momentum of the NS,

$$\dot{L}_n + \dot{L}_p = I_n\,\dot{\Omega}_n + I_p\,\dot{\Omega}_p = 0\,. \tag{41}$$

If we now add an external spin-down torque (divided by the total moment of inertia) α due to electromagnetic emission and use equation (15), the glitch model equations become

$$\begin{aligned}\dot{\Omega}_v &= -2\,\Omega_v\,\mathcal{B}_{MF}\,\frac{\Omega_v - \Omega_{\rm p}}{1-\varepsilon_{\rm n}}\\ \dot{\Omega}_{\rm p} &= -\frac{\alpha}{1-x_v} - \frac{x_v}{1-x_v}\dot{\Omega}_v,\end{aligned} \tag{42}$$

where we have introduced the fractional moment of inertia $x_{\rm x} = I_{\rm x}/I_T$ (x = p,n) and $x_v = x_n/(1-\varepsilon_n)$, while I_T is the total moment of inertia of the star. We also exploited the fact that $\Omega_{vp} = (1-\varepsilon_{\rm n})\Omega_{\rm np}$.

Hence, the form of the equations (42) does not change because of the additional entrainment coupling; moreover, it is possible to include ε_n into the phenomenological parameters. Since our aim is to study the effect of non-linear mutual friction (and as we have shown that the presence of ε_n does not change its form), we will set $\varepsilon_n = 0$ so that equation (38) reduces to $\Omega_v = \Omega_n$ and $x_v = x_n$.

The p-component here represents the 'normal' component, i.e. the proton–electron fluid in the star, the crust, and all components that are coupled to it on a dynamical time-scale that is shorter than that of the glitch. In many models it is assumed that, due to electron scattering off magnetized vortex cores (Alpar & Sauls 1988), the superfluid in the core is coupled to the crust fast enough that it can be included in the p component. However, in the outer core the coupling time-scale due to mutual friction may be comparable with the rise time (Newton, Berger & Haskell 2015a). This effect has been studied both by integrating the full density-dependent equations with also density-dependent mutual friction in the core and constant drag in the crust (Haskell et al. 2012; Haskell & Antonopoulou 2014) or by treating the superfluid in the core as an additional component in a three-component model with density-dependent drag in the crust (Graber et al. 2018; Pizzochero, Montoli & Antonelli 2020; Sourie & Chamel 2020a). What is observed is that the outer core recouples after the glitch, giving rise to a short-term relaxation and possibly an 'overshoot', in which the observed frequency rises above the observed long-term post-glitch frequency, a behaviour that has indeed been observed in a recent glitch of the Vela pulsar (Ashton et al. 2019; Pizzochero et al. 2020).

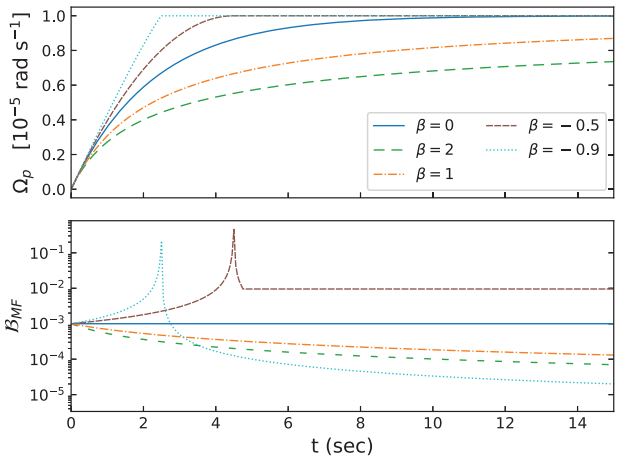

Figure 3. Study of the rise time for a power-law drag $\tilde{\mathcal{R}}$ with initial lag $\Omega_{\rm np} = 10^{-3}$ rad s^{-1} , $x_{\rm p} = 0.99$, and torque $\alpha = 10^{-9}$ rad s^{-2}.

In the following we adopt an approximate prescription to model this behaviour by modifying equations (42) to account for a third component – with fractional moment of inertia $rx_{\rm p}$ – that recouples to the remaining part of the p-component (having fractional moment of inertia $(1-r)x_{\rm p}$) with a typical time-scale $\tau_{\rm co}$. We thus consider the following system of equations

$$\begin{aligned}\dot{\Omega}_{\rm n} &= -2\mathcal{B}_{MF}\Omega_{\rm n}\,(\Omega_{\rm n} - \Omega_{\rm p}),\\ x_{\rm p}(1 - r\,e^{-t/\tau_{co}})\,\dot{\Omega}_{\rm p} + x_{\rm n}\,\dot{\Omega}_{\rm n} &= -\alpha,\end{aligned} \tag{43}$$

which imply that the third component is completely decoupled at $t = 0$: at the beginning of our simulation the effective moment of inertia fraction of the normal component is $x_{\rm p}(1-r)$, lower than the asymptotic value $x_{\rm p}$ that is reached at the end of the recoupling. Clearly, the general relation $x_{\rm p} + x_{\rm n} = 1$ is still valid.

Following Haskell & Antonopoulou (2014) and Newton, Berger & Haskell (2015b) we will set $r = 0.75$ and choose for $\tau_{\rm co}$ the fiducial value of 71 s so that the latter is compatible with the standard value of the mutual friction coefficient in the core. Later on we will test how a different choice of $\tau_{\rm co}$ affects the glitch sizes predicted with this model.

5 NUMERICAL RESULTS: STUDY OF THE GLITCH RISE

To begin our analysis we perform a numerical integration of the two-component model defined by the equations in equation (42) for the power-law ansatz equation (24). First, we study how the glitch rise time changes with the value of β: the results are shown in Fig. 3. Following Seveso et al. (2016), we assume that initially there is a lag between the two fluids of $\Omega_{\rm np} = 10^{-3}$ rad s^{-1}, which, for a stellar

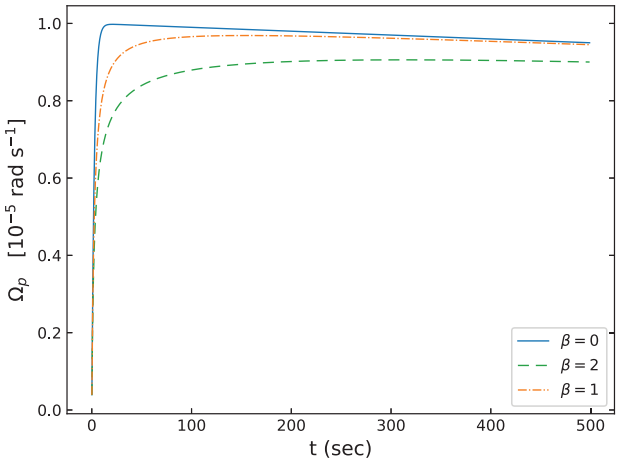

Figure 4. Long time evolution for positive β, in which we verify that the value of the glitch amplitude after the first minutes is not necessarily the same for all cases. The initial lag used is $\Omega_{\rm np} = 10^{-3}$ rad s^{-1}, $I_p/I_T = 0.99$, and torque $\alpha = 10^{-9}$ rad s^{-2}.

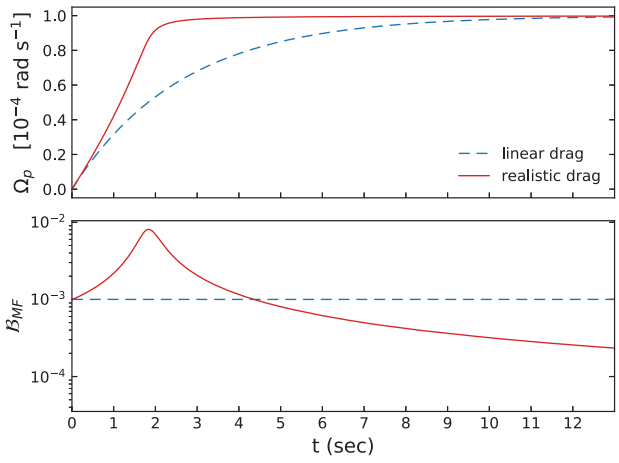

Figure 5. Glitch rise (red, solid) for the microscopic drag prescription in equation (30) compared to the exponential rise given by linear mutual friction (blue, dashed) for $x_p = 0.99$. The initial lag is $\Delta\Omega_{np} = 10^{-2}$ rad s^{-1}, larger than the value for which the maximum of $\mathcal{B}_{\rm MF}$ occurs.

radius of 10 km, corresponds to a lag of $v_{\rm np} = 10^3$ cm s^{-1} in the crust near the equator.

To compare cases corresponding to different values of β, we impose that all models have the same value of $\tilde{\mathcal{R}} = 10^{-3}$ at $t = 0$, so that the initial slope of the rise is equal for each value of β because, initially, the angular momentum is transferred with the same $\mathcal{B}_{MF}$. We then simulate each model by solving the implicit equation (24) at each integration step so that the evolution of $\tilde{\mathcal{R}}$ and $\mathcal{B}_{\rm MF}$ is peculiar to each model. With the simple power-law model we cannot test values of $\beta \leq -1$ (and thus the value $\beta = -3/2$ associated with kelvin waves), because the drag force equation (19) would diverge when the lag goes to zero, and consequently equation (24) may not have solutions. This issue is addressed in the more realistic model we will discuss later in this section.

We observe that for negative values of β the rise is faster than for the usual linear model with $\beta = 0$, which is used here as a reference since it allows to define the exponential timescale for the process. Furthermore, $\Omega_{\rm p}$ grows to the asymptotic value in a finite time because of the rise in the mutual friction coefficient $\mathcal{B}_{MF}$. Afterwards the value of the $\mathcal{B}_{MF}$ drops sharply (as can be seen in the lower panel of Fig. 3) and the frequency evolution essentially stops. Conversely, for positive values of β the rise is much gentler because the angular momentum transfer rate decreases with the lag; we also observe that, for values of β high enough, this may result in smaller glitches when the time taken for the rise becomes longer than the spin-down typical time-scale. This effect can be seen in Fig. 4 for the $\beta = 2$ case, where the integration is performed long enough that the spin-down torque effects become apparent.

The behaviour for negative values of β, for which we observe a very rapid rise, is consistent with observations of recent glitches in the Crab pulsar, and also with a recent large glitch in the Vela pulsar, for which an upper limit on the rise time of 12 s was set at the 90 per cent confidence level, with the data favouring, in general, very short rise times (Ashton et al. 2019). It is therefore clear that to obtain quantitative constraints on interior NS physics it is not sufficient to calculate drag coefficients for a fixed $|\mathbf{v}_{\rm Lp}|$ and then treat them as constants to obtain an exponential rise, as the behaviour inferred from timing observations is qualitatively different. At the same time, we have to point out that the current data do not allow us to resolve the glitch behaviour below 10 s where the differences with the exponential rise are most visible. This situation might improve in the future, as the observational time-span keeps growing – thus allowing for more refined statistical models of the intrinsic noise and improving the sensitivity.

We now turn our attention to the more microphysical prescription for the drag given in equation (30) and plotted in Fig. 2, which allows for both kelvin and phonon contributions in the NS crust.

From our previous analysis of the power-law case, we expect to have different behaviours for the glitch rise if the initial lag is larger or smaller than the value for which the maximum of $\mathcal{B}_{\rm MF}$ occurs, i.e. if the drag is in the negative β regime for high values of $|\mathbf{v}_{\rm Lp}|$, or in the positive β regime for low values of $|\mathbf{v}_{\rm Lp}|$.

To investigate this we integrate the two-component model for different initial conditions, for initial values of $v_{\rm np} = R\Omega_{\rm np}$ both before and after the peak of $\mathcal{B}_{\rm MF}$. Examples of the results are shown in Figs 5 to 7. In the case with a large lag at $t = 0$ that falls in the $\beta < 0$ part of the drag, we can observe a change in the convexity of the rise in correspondence of the activation of the phonon dissipation channel, see Fig. 5. In these cases the initial rise is very rapid, and likely to decouple part of the core, causing an 'overshoot' and rapid post-glitch recoupling, as expected in some glitch models (see e.g. Haskell et al. 2012; Antonelli & Pizzochero 2017; Graber et al. 2018; Pizzochero et al. 2020). For small values of the initial lag, on the other hand, only values of $\beta > 0$ are sampled, and the mutual friction strength drops off as the glitch proceeds. Like in the previous simpler case, this behaviour can possibly lead to smaller amplitude glitches, as the coupling time-scale becomes long enough to be comparable with the spin-down time-scale and the rise is effectively halted.

Throughout this entire section (and in the following one as well) we used $x_{\rm n} = 0.01$. This value of the fractional moment of inertia is consistent with that of a crustal superfluid, even though the S-wave superfluid might well extend into the inner core (Zuo et al. 2004) – in which case a value of $x_{\rm n} \approx 0.1$ would be more appropriate. Still, we decided to use $x_{\rm n} = 0.01$ to be consistent with the realistic model developed for the crust. A larger value of the superfluid fractional moment of inertia would result in a larger angular momentum reservoir, and therefore bigger glitches.

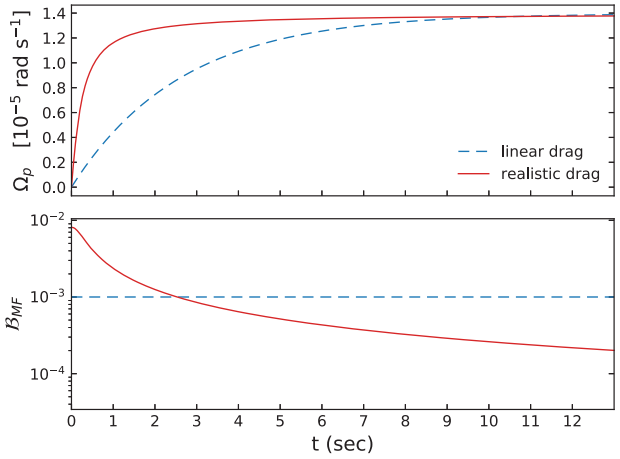

Figure 6. Glitch rise (red, solid) for the microscopic drag prescription in equation (30) compared to the exponential rise given by linear mutual friction (blue, dashed) for $x_p = 0.99$. The initial lag is $\Omega_{\rm np} = 1.4 \times 10^{-3}$ rad s^{-1} that corresponds to the value for which the maximum of $\mathcal{B}_{\rm MF}$ occurs.

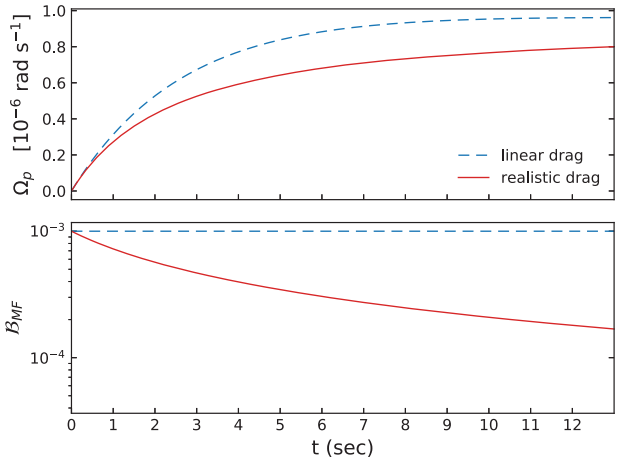

Figure 7. Glitch rise (red, solid) for the microscopic drag prescription in equation (30) compared to the exponential rise given by linear mutual friction (blue, dashed) for $x_p = 0.99$. The initial lag is $\Omega_{\rm np} = 10^{-4}$ rad s^{-1} and thus smaller than the value for which the maximum of $\mathcal{B}_{\rm MF}$ occurs.

6 NUMERICAL RESULTS: GLITCH SIZE DISTRIBUTIONS

In the previous section we mostly focused on the effects of the microscopic drag in equation (30) on the glitch rise, namely on the first few seconds after the glitch is started. The same friction model can also be used to study the long time frequency evolution of the star after a glitch, and also glitch sizes. The frequency evolution is ultimately determined once the initial lag, and consequently the initial coupling time-scale between the two components, is chosen. This quantity is not constrained, and may vary from glitch to glitch even in the same star. Therefore, we now study the glitch size distributions that we get out of the model for an initial lag in the interval [10: 10^5] cm s^{-1} (see Fig. 8).

First, we observe that for large initial lags the drag is mainly due to Kelvin excitations and increases as the system recouples, leading to a very rapid rise. This in turn may decouple part of the core and lead to a larger initial jump in frequency. To investigate this effect we consider the approximate 3-component model in Section 3.2, in

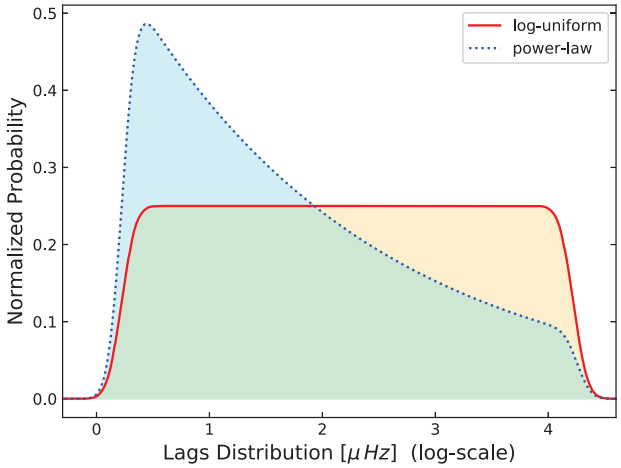

Figure 8. Input distributions of the initial lags for the two cases of interest: log-uniform (red, solid) in the interval [10: 10^5] cm s^{-1} and power law (blue, dashed) in the same interval with exponent -1.2.

which the core recouples with a time-scale $\tau_{\rm co}$. This means that the angular momentum is transferred to an observable p-component with smaller inertia and results in larger glitches (although note that it will not reproduce an overshoot as a full 3-component model such as that of Graber et al. (2018), Pizzochero et al. (2020), Sourie & Chamel (2020b). The effect is more evident for large initial lags for which angular momentum is transferred more rapidly ($\mathcal{B}_{MF}$ higher) and the fraction of core that has already recoupled is smaller.

The initial condition have been chosen to be consistent with parameters of the Vela pulsar, so that $\Omega_p(0) \approx \Omega_n(0) = 70.34$ rad s^{-1} and $\alpha = 9.8 \times 10^{-11}$ rad s^{-2}. Also, in order to test the effects of the of $\tau_{\rm co}$ we consider the fiducial value for Vela (see Haskell & Antonopoulou 2014; Newton et al. 2015b), namely $\tau_{\rm co} = 71$ s, but also $\tau_{\rm co} = 7.1$ s which is compatible with the linear model time-scale and $\tau_{\rm co} = 710$ s. Throughout this entire section the glitch is computed from the residuals, namely as $\Omega_p(t) - \Omega_p(0) + \alpha\, t$, where α is the absolute value of the spin-down rate, because this is compatible with the observational procedure.

As a first step we consider initially a log-uniform distribution of the initial lags $v_{\rm np}$ in the range [10; 10^5] cm s^{-1} (see Fig. 8). The output glitch distributions in the linear case are presented in Fig. 9: as expected they are flat as well and roughly scaled by a factor $x_n = 0.01$, while the only effect of the approximate three component model is to slightly shift the glitch sizes to bigger values. Furthermore, since in the linear model the angular momentum is transferred at a constant rate, the effects of the approximate 3-component model are the same for each initial lag, namely the output glitch-size distribution is 'rigidly' shifted to the right by a greater amount for larger values of $\tau_{\rm co}$.

In Fig. 10 we compare the output glitch distribution for the standard linear drag 2-component model with the ones obtained using the realistic non-linear drag from Section 3.2 and assuming to 'measure' the glitch after 200 s.

We see that now in all cases with non-zero $\tau_{\rm co}$ the output distributions present a peak for high glitches, and while there is a quantitative difference between the different cases, the qualitative feature is present in all the three models. To point out that this effect is due to the modified mutual friction – and not to the approximate 3-component model, so that it must be visible even for $\tau_{\rm co} = 0$ – in Fig. 11 we plot the output distribution that we get if we 'measure' the glitch after 50 s. Note that the latter is compatible with the current

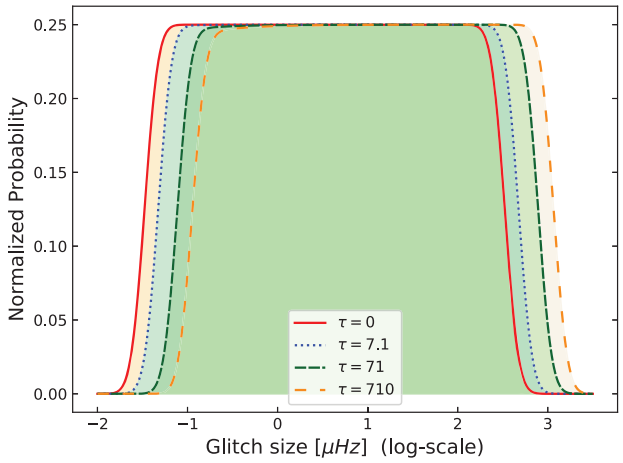

Figure 9. Output glitch size distribution in the linear case for an initial (log-scale) uniform lags distribution. The linear $\tau = 0$ case (red, solid) is given for comparison with the approximate 3-component ones: $\tau = 7.1$ (blue, dotted), $\tau = 71$ (green, dashed) and $\tau = 710$ (yellow, dashed).

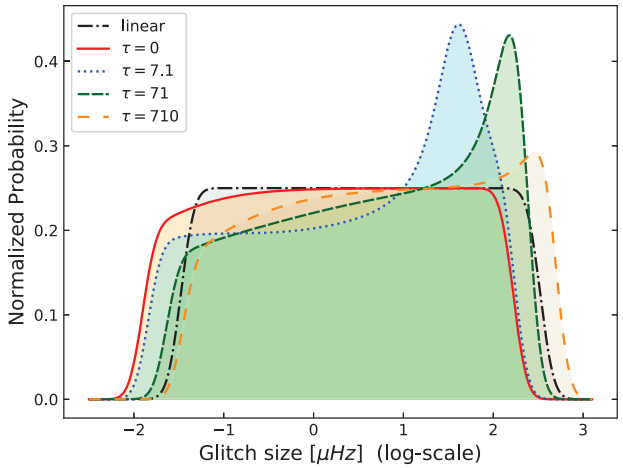

Figure 10. Comparison of glitch size distributions in the linear and realistic non-linear case for an initial log-uniform lags distribution. The linear case (black, dash-dotted) is given for comparison with the non-linear 2-component model (red, solid) and approximate 3-component ones: $\tau = 7.1$ s (blue, dotted), $\tau = 71$ s (green, dashed) and $\tau_{\rm co} = 710$ s (yellow, dashed). The glitch is measured at 200 s.

observational limits on the full glitch rise time (Dodson, McCulloch & Lewis 2002), although the initial rise may be of the order of 12 s (Ashton et al. 2019). In Fig. 11 the peak is in fact present also for the non-linear $\tau_{\rm co} = 0$ s model. This feature is interpreted as follows: for very high initial lags, namely $v_{np} \approx 10^5$ cm s^{-1}, the system is sampling the area well right to the peak of the $\mathcal{B}_{MF}$ plot (see Fig. 2), so that we have a considerably low value for the initial angular momentum transfer rate. This implies that the angular momentum reservoir is not completely emptied out within 50 s and we measure a smaller glitch size. The system is sampling the kelvonic branch, so that the rate increases as the system recouples and the residual is transferred within the next 150 s in the $\tau_{\rm co} = 0$ case – and can possibly be considered as a delayed rise.[3] If we consider

[3]The delayed rise in the largest glitch observed in Crab pulsar (see Shaw et al. 2018) could be the effect of a non-linear mutual friction – with model parameters different from those considered in this work.

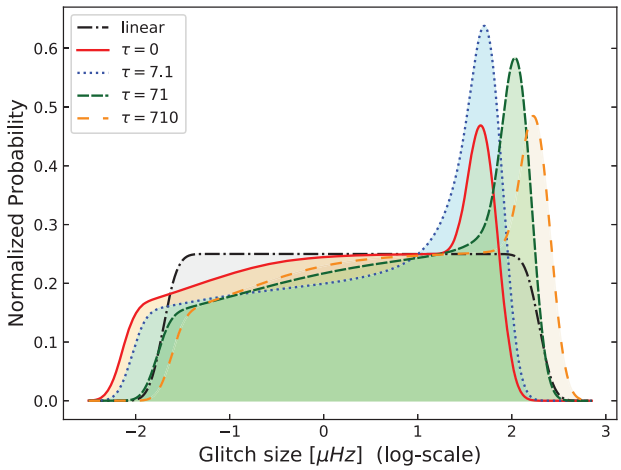

Figure 11. Comparison of glitch size distributions in the linear and realistic non-linear case for an initial log-uniform lags distribution. The linear case (black, dash-dotted) is given for comparison with the non-linear 2-component model (red, solid) and approximate 3-component ones: $\tau = 7.1$ s (blue, dotted), $\tau = 71$ s (green, dashed), and $\tau_{\rm co} = 710$ s (yellow, dashed). The glitch is measured at 50 s.

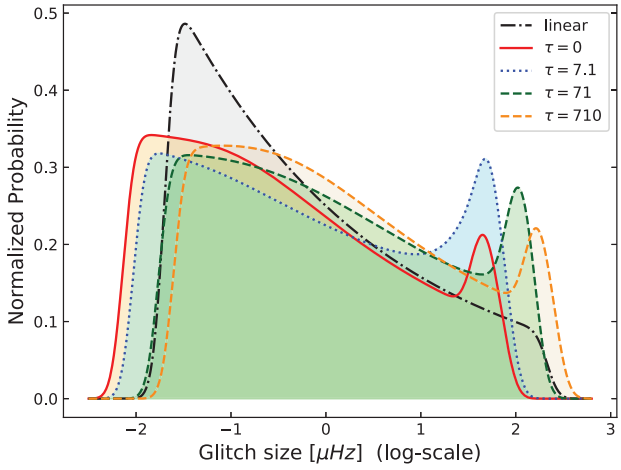

Figure 12. Comparison of glitch size distributions in the linear and realistic non-linear case for an initial power-law lags distribution. The linear case (black, dash-dotted) is given for comparison with the non-linear 2-component mode (red, solid) and two approximate 3-component ones: $\tau = 7.1$ s (blue, dotted), $\tau = 71$ s (green, dashed), and $\tau_{\rm co} = 710$ s (yellow, dashed). The power-law exponent is -1.2 and the glitch is measured at 50 s.

the approximate 3-component model, the dynamics depends on the interplay between two 'time-scales', the angular momentum transfer rate (which changes during the evolution) and $\tau_{\rm co}$. As a result, we still observe the peak after 200 s. As expected, the microscopic drag of equation (30) gives also smaller glitches (with respect to the linear case) when the system samples the phonon-branch only, namely for low initial lags.[4] This effect is counteracted in the approximate three-component model and in the fiducial model (the one with $\tau_{\rm co} = 71$ s) we observe a reduction in the number of small glitches (see Fig. 10).

In Fig. 12 we test a somewhat more realistic scenario in which the initial lag distribution is not log-uniform but follows a power

[4]Recall that $v_{\rm Lp} \leq v_{\rm np}$, so that for small initial lag the system is sampling the region left to the $\mathcal{B}_{\rm MF}$ peak, see Fig. 2.

law with exponent −1.2 as suggested by both simulations of vortex avalanches (Warszawski & Melatos 2012) and observations of pulsar glitch size distributions (Melatos, Peralta & Wyithe 2008; Howitt et al. 2018; Fuentes, Espinoza & Reisenegger 2019), see Fig. 8. The features discussed in the previous log-uniform case are still present, but now we are sampling smaller values for the initial lags with higher probability. In this case the distribution turns out to be bimodal, with a narrower larger size component above approximately $10^2\ \mu Hz$ and a wider second component extending to lower sizes. This distribution is in qualitative agreement with the observed distribution presented by Fuentes et al. (2017) and Ashton, Prix & Jones (2017), which suggests that the same mechanism (the recoupling of a pinned superfluid) can explain both populations if a non-linear drag model is used.

It is thus possible that in NSs with predominantly large glitches (like the Vela pulsar) the events are triggered in stronger pinning regions, while in stars with a majority of smaller glitches, these are likely to be triggered in weaker pinning regions. This is in agreement with the analysis of Haskell et al. (2018), according to which larger glitches are likely to be triggered in the outer core of the star. To implement this feature in the model one could make use of a distribution for $x_{\rm n}$ (instead of a flat fixed value $x_{\rm n} = 0.01$). In this way one can account for the fact that, for large values of the lags, the superfluid reservoir involved in the process extends also to the outer core – where it is pinned – and therefore its fractional moment of inertia is bigger. Given the uncertainties in the values for $x_{\rm n}$ we have not included this feature in the model, but this constitutes an interesting refinement to be explored in future works.

Although we have also tested approximate 3-component models, none of them will reproduce an important feature of the full 3-component ones – the overshoot (see Graber et al. 2018; Pizzochero et al. 2020; Sourie & Chamel 2020b). The presence of an overshoot can lead to a glitch size (measured at $50\,s$) that is bigger than the asymptotic value. The overshoot is expected to affect more for large initial lags, and therefore it would shift the rightmost peak by some amount. However, according to up-to-date estimates (see Montoli et al. 2020a) the overshoot size will not be bigger then double the asymptotic value, that is it will shift the rightmost peak by no more than ≈0.3, so that the qualitative features are the same. To this respect, we also note that the asymptotic value of our approximate 3-component model is bigger than the 2-component one, and in some way already accounts for the overshoot effects in the size distributions by slightly overestimating them (see Fig. 12, especially the fiducial $\tau = 71$ case).

Also, to obtain more stringent constraints future work should include corrections due to general relativity (see e.g. Sourie et al. 2017; Antonelli, Montoli & Pizzochero 2018; Gavassino et al. 2020) and the full density dependence of the drag in the core (Alpar et al. 1984; Andersson & Comer 2006) and crust of the star (Graber et al. 2018).

7 CONCLUSIONS

We studied the effect of a non-linear form of the mutual friction on pulsar glitch sizes and rise times: we considered both a simple power-law dependence of the drag force on the relative velocity between superfluid vortices and the normal component, and a physically motivated model for the crust of an NS, in which for low vortex velocities the drag is mainly due to phonon excitations while for high velocities to kelvin excitations (Jones 1990a, 1992; Epstein & Baym 1992; Graber et al. 2018).

For the simple power-law case we find that for positive values of the index β the rise is slower than in the standard linear case, for which the rise is exponential. This case is relevant for both classical turbulence, for which one expects a power-law index $\beta = 1$ and isotropic quantum turbulence for which $\beta = 2$ and confirms the previous results of Peralta et al. (2006) for the rise time. Additionally we find that for $\beta > 0$ the size of the glitch can also be affected, as the coupling time-scale rapidly grows to the point where it is comparable with the spindown time-scale, thus effectively halting the rise and leading to smaller glitches.

For negative values of the power-law index β the situation is reversed, and the drag parameter $\tilde{\mathcal{R}}$ grows as the vortices slowdown. This is particularly relevant for glitches, as the rapid rise is thought to be due to mutual friction coupling given by the excitation of Kelvin waves either in the crust, as vortices move past the ions in the lattice, or core, as they cut through superconducting fluxtubes (Ruderman et al. 1998; Link 2003). In both the cases where the dissipation is due to excitation of Kelvin waves the index is expected to be $\beta = -3/2$.

In the more realistic model defined in equation (30) we have that at high velocities (above $v_0 \approx 10^3\,{\rm cm\,s^{-1}}$) vortices experience a kelvonic drag that scales as $v_{\rm Lp}^{-3/2}$, while at lower velocities the kelvonic contributions are suppressed and phonons dominate the drag, scaling as $v_{\rm Lp}$ (Jones 1990a). This means that for high initial lags (corresponding to strong pinning regions) vortices experience an initially increasing drag after the depinning, as in the $\beta < 0$ power-law case. On the contrary, for low initial lags only $\beta > 0$ regions are sampled (see Fig. 2). We explore the effect of this drag model on the observed glitch size distribution with both our standard 2-component model, and also with an approximate 3-component model. In both cases the observed glitch distribution presents an excess of large glitches. This automatically implies that, given an input distribution that favours small initial lags (Howitt et al. 2018), the observed glitch distribution is bimodal, with a narrower peak above $\Delta\nu_{\rm glitch} \approx 10^2\ \mu$Hz and a wider component for lower sizes. This is qualitatively consistent with what is observed in the pulsar population (Fuentes et al. 2017). It is thus possible that both populations of glitches (i.e. the 'large' and 'small' glitches) originate from the same mechanism, namely the recoupling of a pinned superfluid component, once the realistic kelvin-phonon mutual friction is considered.

Furthermore, we speculate that the different size distributions observed in individual pulsars may be due to the glitch originating in different regions of pinned vorticity. For pulsars where power-law distributions are observed, it is likely that the glitch originates in regions where the pinning is not strong enough to allow for large initial lags (i.e. regions in which the typical lags before unpinning are not large enough to allow the vortex to experience the kelvonic, $\beta = -3/2$, branch of the mutual friction). On the other hand, in pulsars that glitch quasi-periodically with a preferred size, such as the Vela or J0537-6910, it is likely that glitches occur in strong pinning regions where only kelvonic mutual friction is present. This would be the case in the outer core, where vortex-flux tube interactions allow for strong pinning (Sourie & Chamel 2020a), but will also excite Kelvin waves on the vortices once they are free to cut through the flux tubes (Ruderman et al. 1998; Link 2003).

In conclusion we have shown that non-linear mutual friction in NS interiors leads to appreciable differences in pulsar glitch rises compared to the standard linear model. In particular, a non-linear drag that interpolates between the phononic and kelvonic regimes allows to explain the differences observed in the size distributions in terms of a single process and is also consistent with recently observed glitches in the Crab and Vela pulsar (Haskell et al. 2018). To obtain constraints on the EOS, on transport parameters in the NS interior and on the glitch trigger region, however, future work should aim to include the effect of general relativity (Sourie et al. 2017;

Antonelli et al. 2018; Gavassino et al. 2020), and to make contact with microphysical calculations of interactions between vortices and ions in the NS crust (Seveso et al. 2016; Wlazlowski et al. 2016). This will allow to study how structural differences between glitching pulsars affect their glitch size distribution, and to constrain microphysical parameters in the high density interior of the star (Ho et al. 2015; Pizzochero et al. 2017; Montoli et al. 2020b).

ACKNOWLEDGEMENTS

TC acknowledges support from PHAROS COST Action (CA16214). VK, MA, and BH acknowledge support from the Polish National Science Centre grant SONATA BIS 2015/18/E/ST9/00577, P.I.: B. Haskell. This research was supported in part by the INT's U.S. Department of Energy grant No. DE-FG02- 00ER41132. The authors thank N. Andersson for reading the manuscript and useful critical comments. We also thank the anonymous referees for the constructive comments.

DATA AVAILABILITY

The data underlying this article are available in the article and in its online supplementary material.

REFERENCES

Abbott B. P., Abbott R., Abbott T. D., Acernese F., 2018, Phys. Rev. Lett., 121, 161101
Alpar M. A., 2017, J. Astrophys. Astron., 38, 44
Alpar M. A., Sauls J. A., 1988, ApJ, 327, 723
Alpar M. A., Langer S. A., Sauls J. A., 1984, ApJ, 282, 533
Anderson P. W., Itoh N., 1975, Nature, 256, 25
Andersson N., Comer G. L., 2006, Class. Quantum Gravity, 23, 5505
Andersson N., Sidery T., Comer G. L., 2006, MNRAS, 368, 162
Andersson N., Sidery T., Comer G. L., 2007, MNRAS, 381, 747
Andersson N., Glampedakis K., Ho W. C. G., Espinoza C. M., 2012, Phys. Rev. Lett., 109, 241103
Antonelli M., Pizzochero P. M., 2017, MNRAS, 464, 721
Antonelli M., Montoli A., Pizzochero P. M., 2018, MNRAS, 475, 5403
Antonopoulou D., Espinoza C. M., Kuiper L., Andersson N., 2018, MNRAS, 473, 1644
Ashton G., Prix R., Jones D. I., 2017, Phys. Rev. D, 96, 063004
Ashton G., Lasky P. D., Graber V., Palfreyman J., 2019, Nat. Astron., 3, 1143
Baym G., Chandler E., 1983, J. Low Temp. Phys., 50, 57
Bekarevich I. L., Khalatnikov I. M., 1961, Sov. Phys. JETP, 13, 643
Bogdanov S. et al., 2019, BAAS, 51, 506
Carter B., Chamel N., 2005, Int. J. Mod. Phys. D, 14, 749
Carter B., Chamel N., Haensel P., 2006, Int. J. Mod. Phys. D, 15, 777
Chamel N., 2012, Phys. Rev. C, 85, 035801
Chamel N., 2013, Phys. Rev. Lett., 110, 011101
Chamel N., 2017, J. Astrophys. Astron., 38, 43
Delsate T., Chamel N., Gürlebeck N., Fantina A. F., Pearson J. M., Ducoin C., 2016, Phys. Rev. D, 94, 023008
Dodson R. G., McCulloch P. M., Lewis D. R., 2002, ApJ, Lett., 564, L85
Donnelly R. J., 1991, Quantized Vortices in Helium II. Cambridge Univ. Press, Cambridge, UK
Drummond L. V., Melatos A., 2017, MNRAS, 472, 4851
Drummond L. V., Melatos A., 2018, MNRAS, 475, 910
Epstein R. I., Baym G., 1992, Astrophys. J., 387, 276
Fuentes J. R., Espinoza C. M., Reisenegger A., Stappers B. W., Shaw B., Lyne A. G., 2017, A&A, 608, 131
Fuentes J. R., Espinoza C. M., Reisenegger A., 2019, A&A, 630, A115
Fulgenzi W., Melatos A., Hughes B. D., 2017, MNRAS, 470, 4307
Gavassino L., Antonelli M., Pizzochero P., Haskell B., 2020, MNRAS, 494, 3562
Glampedakis K., Andersson N., Samuelsson L., 2011, MNRAS, 410, 805
Graber V., Cumming A., Andersson N., 2018, ApJ, 865, 23
Gügercinoğlu E., Alpar M. A., 2020, MNRAS, 496, 2506
Haensel P., Potekhin A. Y., Yakovlev D. G., 2007, in Haensel P., Potekhin A. Y., Yakovlev D. G., eds, Neutron stars 1: Equation of state and structure. Vol. 326. Springer, New York, USA
Hall H. E., Vinen W. F., 1956, Proc. R. Soc. London Ser. A, 238, 215
Haskell B., Antonopoulou D., 2014, MNRAS, 438, L16
Haskell B., Melatos A., 2015, Int. J. Mod. Phys. D, 24, 1530008
Haskell B., Sedrakian A., 2018, Superfluidity and Superconductiv- ity in Neutron Stars,p. 401
Haskell B., Pizzochero P. M., Sidery T., 2012, MNRAS, 420, 658
Haskell B., Glampedakis K., Andersson N., 2014, MNRAS, 441, 1662
Haskell B., Khomenko V., Antonelli M., Antonopoulou D., 2018, MNRAS Lett., 481, L146
Ho W. C. G., Espinoza C. M., Antonopoulou D., Andersson N., 2015, Sci. Adv., 1, e1500578
Howitt G., Melatos A., Delaigle A., 2018, ApJ, 867, 60
Jones P. B., 1990a, MNRAS, 243, 257
Jones P. B., 1990b, MNRAS, 244, 675
Jones P. B., 1992, MNRAS, 257, 501
Khomenko V., Haskell B., 2018, Publ. Astron. Soc. Austr., 35, e020
Khomenko V., Antonelli M., Haskell B., 2019, Phys. Rev. D, 100, 123002
Langlois D., Sedrakian D. M., Carter B., 1998, MNRAS, 297, 1189
Link B., 2003, Phys. Rev. Lett., 91, 101101
Link B., 2014, ApJ, 789, 141
Lyne A. G., Jordan C. A., Graham-Smith F., Espinoza C. M., Stappers B. W., Weltevrede P., 2015, MNRAS, 446, 857
Melatos A., Peralta C., 2007, ApJ, 662, L99
Melatos A., Peralta C., Wyithe J. S. B., 2008, ApJ, 672, 1103
Mendell G., 1991, ApJ, 380, 530
Mongiovì M. S., Jou D., 2007, Phys. Rev. B, 75, 024507
Montoli A., Antonelli M., Magistrelli F., Pizzochero P., 2020a, preprint (arXiv:2005.01594)
Montoli A., Antonelli M., Pizzochero P. M., 2020b, MNRAS, 492, 4837
Muslimov A. G., Tsygan A. I., 1985, Ap&SS, 115, 43
Newton W. G., Berger S., Haskell B., 2015a, MNRAS, 454, 4400
Newton W. G., Berger S., Haskell B., 2015b, MNRAS, 454, 4400
Palfreyman J., Dickey J. M., Hotan A., Ellingsen S., van Straten W., 2018, Nature, 556, 219
Peralta C., Melatos A., Giacobello M., Ooi A., 2006, ApJ, 651, 1079
Pizzochero P. M., Antonelli M., Haskell B., Seveso S., 2017, Nat. Astron., 1, 0134
Pizzochero P., Montoli A., Antonelli M., 2020, A&A, 636, A101
Prix R., 2004, Phys. Rev. D, 69, 043001
Prix R., Comer G. L., Andersson N., 2002, A&A, 381, 178
Ruderman M., Zhu T., Chen K., 1998, Astrophys. J., 492, 267
Schwarz K. W., 1988, Phys. Rev. B, 38, 2398
Seveso S., Pizzochero P. M., Grill F., Haskell B., 2016, MNRAS, 455, 3952
Shaw B. et al., 2018, MNRAS, 478, 3832
Simula T., 2018, Phys. Rev. A, 97, 023609
Sonin E. B., 1987, Rev. Mod. Phys., 59, 87
Sourie A., Chamel N., 2020a, MNRAS, 493, 382
Sourie A., Chamel N., 2020b, MNRAS, 493, L98
Sourie A., Chamel N., Novak J., Oertel M., 2017, MNRAS, 464, 4641
Srinivasan G., Bhattacharya D., Muslimov A. G., Tsygan A. J., 1990, Curr. Sci., 59, 31
Vinen W. F., 1957, Proc. R. Soc. London Ser. A, 242, 493
Warszawski L., Melatos A., 2012, MNRAS, 428, 1911
Wlazlowski G., Sekizawa K., Magierski P., Bulgac A., Forbes M. M. N., 2016, Phys. Rev. Lett., 117
Zuo W., Li Z. H., Lu G. C., Li J. Q., Scheid W., Lombardo U., Schulze H. J., Shen C. W., 2004, Phys. Lett. B, 595, 44

This paper has been typeset from a TEX/LATEX file prepared by the author.